UNIVERSITY OF CALIFORNIA

SANTA CRUZ

HIGHLY TUNABLE PLASMONIC NANOPARTICLES FOR USE AS SURFACE ENHANCED RAMAN SCATTERING SUBSTRATES FOR THE DETECTION OF PROTEIN AND LIPID BIOMARKERS IN SOLUTION

A dissertation submitted in partial satisfaction
of the requirements for the degree of

DOCTOR OF PHILOSOPHY

in

CHEMISTRY

By

A'Lester C. Wiggins-Allen

March 2022

The Dissertation of A'Lester C. Wiggins-Allen

is approved:

_____

Professor Jin Z. Zhang, Chair

_____

Professor David Kliger

_____

Professor Ilan Benjamin

_____

Peter Biehl
Vice Provost and Dean of Graduate Studies

Table of Contents

LIST OF FIGURES

LIST OF SCHEMES

LIST OF TABLES

protein, Anti-SARS-CoV-2 mAb without a his-tag, and His-tagged spike-mAb

Abstract

HIGHLY TUNABLE PLASMONINC NANOPARTICLES FOR USE AS SURFACE ENHANCED RAMAN SCATTERING SUBSTRATES FOR THE DETECTION OF PROTEIN AND LIPID BIOMARKERS IN SOLUTION

A'Lester C. Wiggins-Allen

Because of the high sensitivity, molecular specificity, and non-invasive sampling technique, surface enhanced Raman scattering (SERS) is one of the most powerful analytical techniques. Additionally, its low interference from water makes SERS uniquely effective for biological sensing. In the last decade, the emergence of life-threatening pathogens and debilitating diseases has outpaced the development of treatments. Detection and monitoring have become the first guard approach to containing the spread of deadly infections such as Ebola, H1N1, and SARS-CoV-2. As a result, recent SERS research has heavily focused on studying biological processes and point of care diagnostics.

The choice of the nanostructure of the SERS substrate determines its localized surface plasmon resonance which directly contributes to the overall SERS enhancement. Hollow nanostructures are advantages as SERS substrates due to their highly tunable optical properties, which arise from varying the outer diameter to shell thickness. However, hollow nanoparticles have been underexplored due to a more complex synthesis needed to control their physical dimensions. The work in this

dissertation explores using hollow gold nanospheres (HGNs) as a template to synthesize rugose hollow nanostructures. HGNs enabled fine control over the hollow (void space) core. However, isotropic geometry yields a single plasmon mode limiting the number of hot spots for SERS enhancement. Rugose nanostructures have improved electric field strength as compared to smooth nanoparticles. More specifically, spiny nanostructures have better electron confinement at their tips. A multibranched structure has an increased number of hot spots. Multibranched hollow gold nanostructures were synthesized using hollow gold nanospheres as a seed particle.

Chapter 1 introduces general concepts of plasmonics applied to Raman spectroscopy, specifically how the nanostructure of noble metals influences the localized surface plasmon resonance. The latter part of chapter 1 discusses the characterization of metal nanoparticles through absorption spectroscopy and electron microscopy.

Chapter 2 highlights the use of hollow gold nanostars and PEG-based conjugation to overcome the difficulty of detecting amyloid beta 1-14. As a result, we increased our understanding of the parameters needed to detect low Raman scatterers in aqueous media. The key findings were that hollow gold nanostars enable improved SERS enhancement compared to hollow gold nanospheres and solid gold nanostars. The analytical enhancement factor of the hollow gold nanostars was 1.29×10^9 for the 1367 cm^{-1} peak in R6G was shown to be 11.5 times increased compared to hollow gold nanospheres.

Chapter 3 focuses on developing a new method to detect the SARS-CoV-2 S1 spike protein and the anti-SARS-CoV-2 antibodies by anchoring the his-tagged spike protein to a multibranched gold nanoshell for detection via SERS. Multibranched gold nanoshells were prepared using $HAuCl_4$, $AgNO_3$, and ascorbic acid to improve the optical and morphological properties of smooth ~150 nm gold nanoshells for detecting proteins. The multibranched gold nanoshells were gently mixed with a his-tagged SARS-CoV-2 S1 spike protein, purified, and mixed with Anti-SARS-CoV-2 monoclonal antibodies. Raman and SERS measurements of the spike protein and monoclonal antibody with a histidine tag showed a significant increase in peak intensity compared to samples without histidine. Enhanced SERS peaks from the spike protein at 1079, 1178, and 1592 cm^{-1} are attributed to δ =N-H, νC-N, νC=C, respectively. Enhanced peaks from the Anti-SARS-CoV-2 monoclonal antibody at 861, 1205, 1454, and 1630 cm^{-1} can be assigned to νN-H, νC-C, C-H def, and νC=O associated with the phenylalanine and tyrosine rich region closest to the binding sites on mAb.

Chapter 4 discusses the work to apply fiber-enhanced SERS to monitor the repair process of a self-healing wastewater purification membrane. The use of a SERS substrate with hollow core photonic crystal fiber (HCPCF) as a waveguide increased the signal intensity for major distinguishing hydrocarbon tail peaks at 1436cm^{-1} (CH_2 bend) and 1296cm^{-1} (CH_2 twist) by 1.5 and 2x as compared to SERS alone. The increase in signal for lower intensity C-C peaks such as 1157cm^{-1} was 14x compared to SERS alone. The results show that SERS coupled with a waveguide can enable highly sensitive *in situ* measurements.

This dissertation is dedicated to my ancestors, whose stories continually inspire me to overcome every obstacle no matter the difficulty.

ACKNOWLEDGEMENTS

My Dissertation Committee: Jin, I have learned so much from you. Thank you so much for setting high expectations while extending autonomy and patience. Your mentorship has helped me become a better researcher and presenter. Thank you, Prof. Kliger, for extending the invite to attend your lab lunches. You and your lab's support were a motivation when I felt unsure that I could finish. Thank you, Prof. Benjamin, for being a calm and collected presence in all our meetings. You reminded me to relax. I hope to have the opportunity to continue working together throughout my career.

Prof. Bakthan Singaram, thank you for taking a physical chemist under your wing. I learned so much through being a TA in your class about how to reach students. Your Singaram two-thirds rule continues to help me push through my self-doubt. Dr. Bin Chen, I am very grateful to have gotten to know you. I cannot express how much your support meant to me. You instilled in me the confidence and resolved to persevere. I have taken your advice to heart and spent many nights with a bottle of wine and the Raman spectrometer, which resulted in the data I needed for many of my publications. Dr. Jing Li, thank you for taking me under your wing at NASA AMES when I was without a home. Your support made it possible for me to graduate.

Labmates: Melissa and Vivien, you both gave me the emotional and mental support that I needed to make it through a fire, pandemic, and depressive times. I cannot thank you both enough for always being there to talk. I will miss your energy and cherish the

memories that we made together. I especially will miss going on walks, having decompressions, and celebrations.

Evan, I am grateful to have met you. You reminded me to stay calm and collected and have good priorities.

Sara, Staci, and Sarah L., thank you for showing me the ropes and setting me up for success later in the lab. I couldn't have asked for a more supportive group of people to work with every day.

Cassandra, Sarah W., and Dylan, you were all fantastic lab mates. It was great seeing you go off and find your passions. I enjoyed carpooling, playing Pokémon Go, and receiving acupuncture.

Mekedi, thank you for growing with me. I learned how to be a better mentor through our time together in the lab. Thank you for your patience with me. I am so happy to see you thrive.

Addis, you are such an inspiration. I know you will thrive and succeed. I will always be there to support you, and I know that you will do the same. I cannot wait to come back to UCSC for your defense.

Friends: Gaby, I saw so many exceptional personal and professional strengths that you had. I strived to be more like you. I cannot express how valuable you have been to my journey through grad school. I hope we get to be coworkers in the future. Regardless, I know we'll always be friends. Juliana, I wish we had gone on more walks, but the

ones that we did were some of my favorite memories. Anna, thank you for organizing fantastic bike rides and other events. You have come through for me in big crucial moments. Eefei, I thoroughly enjoyed every conversation that we had. Thank you for teaching me about stone soup. To my Boyz, I couldn't have made it this far without your support. I also thank my Spark community for so much prayer and support.

Family: Thank you, Jessica, for being my rock. I love you so much. Thank you, dad and mom, for supporting me from the beginning. I am here because you all sacrificed, encouraged, and nurtured me. Thank you, Dimetra, Faye, Bre, and Chris, for rooting for me from the top of your lungs. Despite the distance, I could hear your voices, and I always felt your love.

Mengyu: I will cherish the many nights you kept me company in the lab, lent your time to help me run experiments, and were someone I could discuss the details of my challenges. You helped me develop many of my ideas in complete projects. Because of you, UC Santa Cruz was transformed from just my place of work to one of my favorite places. I am so glad that we met. I love you.

Jeff: Thank you for going on this adventure of grad school together. You have seen me grow the most out of everyone in my adult life. I hope I continue to make you proud and inspire you to live life with hope. Here's to completing one big life goal together. I hope there are many more. I love you.

_____The text of this dissertation includes reprints of the following previously published material:

Chapter 2: Allen, A. C., Romero-Mangado, J., Adams, S., Flynn, M., Chen, B., Zhang, J. Z., "Detection of Saturated Fatty Acids Associated with a Self-Helaing Synthetic Biological Membrane Using Fiber-Enhanced Surface Enhanced Raman Scattering". The Journal of Physical Chemistry B 122, 35, **2018**, 8396-8403.

Amberchan, G., Allen, A. C., Golden, J. H., Singaram, B., Zhang, J. Z., "Real-Time Monitoring of Aqueous Organic Reduction Reactions Using *Ex Situ* Fiber Optic Raman Spectroscopy". ACS Sustainable Chemistry & Engineering 9, 17, **2021**, 6068-6078.

Chapter 3: Allen, A. C., Efrem, M., Mahalingam, U., Guarino-Hotz, M., Foley, A. R., Raskatov, J. A., Song, C., Lindley, S. A., Li, J., Chen, B., Zhang, J. Z., "Hollow Gold Nanosphere Templated Synthesis of PEGylated Hollow Gold Nanostars and Use for SERS Detection of Amyloid Beta in Solution". The Journal of Physical Chemistry B 125, 44, **2021**, 12344-12352.

Chapter 4: Allen, A. C., Guarino-Hotz, M., Getahun, A., Ophus, C., Zhang, J. Z. "Toward Improving Lateral Flow Assays by Versatile Histidine Conjugation to AgAu Multibranched Nanoshells for the Detection of SARS-CoV-2 via Surface Enhanced Raman Scattering". *To be Submitted*

CHAPTER 1

Introduction

1.1. Introduction to Raman Spectroscopy

Molecular vibrations absorb and emit infrared electromagnetic radiation.[1] Raman spectroscopy utilizes a monochromatic excitation source to probe the molecular vibrations. The vibrational frequencies are measured by calculating the difference between elastically scattered and inelastically scattered photons, as seen in Equation 1.1.[2] The difference in energy is known as the Raman Effect. It was predicted by Adolf Smekal in 1923 and experimentally verified by Sir Chandrasekhara Venkata Raman in 1928. Smekal derived inelastic collisions from the conservation of kinetic energy. A simple derivation of Raman scattering is below. Equation 1.2 shows a photon interacting with matter, and emitted photon could either lose energy to the matter as in Equation 1.3 or gain energy as seen in Equation 1.4.

$$\boldsymbol{E_i + h\nu_i = E_f + h\nu_f} \qquad \text{Equation 1.1}$$

$$\boldsymbol{h\nu_i - h\nu_f = (E_f - E_i) = \Delta E = h\Delta\nu} \qquad \text{Equation 1.2}$$

$$\boldsymbol{\nu_{Stokes} = \nu - \Delta\nu} \qquad \text{Equation 1.3}$$

$$\boldsymbol{\nu_{Anti-Stokes} = \nu + \Delta\nu} \qquad \text{Equation 1.4}$$

The initial and final energy states are represented by i and f. The Stokes line represents kinetic energy transfer from the molecule to the photon. The Anti-Stokes line represents the kinetic energy transfer from the photon to the molecule. Figure 1.1 shows an incident photon transferring energy to a water molecule inducing a very short-

lived excited state called a virtual state. The Jablonski diagram shows the energy transitions of the different scattering phenomena. A scattering event where there is no energy exchange between light and matter is called Rayleigh scattering. However, one in a million photons experience an inelastic scattering process where a change of kinetic energy results in a Stokes or Anti-stokes shift.[2] Figure 1.2 shows the three scattering processes in terms of the difference between the incident photon and the scattered photon called the Raman

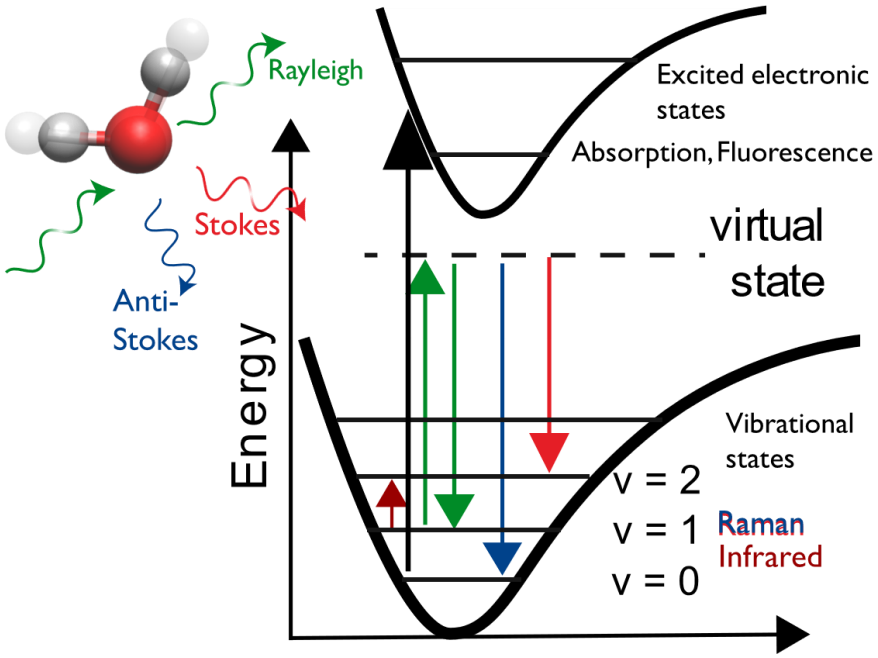

Figure 1.1 Diagram of Raman scattering the energy transitions when a molecule interacts with electromagnetic radiation. Rayleigh scattering (shown in green) has no change in energy as compared to the incident photon. Stokes scattering (shown in bright red) has a loss of energy. Anti-Stokes scattering (shown in blue) gains energy.

shift. The Rayleigh scattered photons do not experience a Raman shift and are at zero, while the Stokes shift is plotted to the right of zero as seen in Raman spectrographs and represents a loss of photon energy.[3] The Anti-Stokes shifts are plotted to the left of the Rayleigh line in Raman spectrographs. The magnitude of the Raman shift can be expressed by Equation 1.5.

$$\boldsymbol{\Delta\nu}\ (\boldsymbol{cm^{-1}}) = \left(\frac{\mathbf{1}}{\boldsymbol{\lambda_0}\ (\boldsymbol{nm})} - \frac{\mathbf{1}}{\boldsymbol{\lambda_1}\ (\boldsymbol{nm})}\right) \times \left(\frac{\mathbf{10^7}\boldsymbol{nm}}{\boldsymbol{cm}}\right) \qquad \text{Equation 1.5}$$

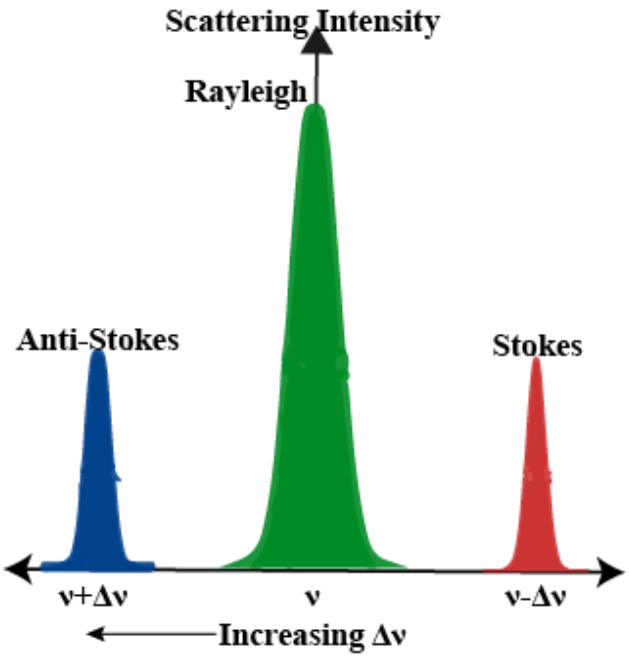

Figure 1.2. Diagram showing Raman shifts in relation to the Raleigh line in green that exists in experimental Raman spectrographs. The Stokes shift (in red) by convention is plotted to the right of the Rayleigh line, and the anti-stokes shift in blue is plotted to the left of the Rayleigh line.

1.2. Plasmonic Nanoparticles as Surface Enhanced Raman Scattering Substrates

As a sub-field of nanophotonics, plasmonics has attracted extraordinary interest in recent years due to its promise of revolutionary impacts on nanotechnology and medicine. Surface plasmons are a coherent oscillation of electron charge that exists in the presence of an oscillating electromagnetic (EM) field. Under resonant conditions, a transverse wave propagates along with the interface of a dielectric and a conductor. The SPR response is not chemically specific but can be overcome using nanoparticles as surface enhanced Raman scattering (SERS) substrates. When the wavelength (λ) of the EM field is 10-20 times smaller than the size (d) of the metal nanostructure, a localized surface plasmon occurs, resulting in localized surface resonance (LSPR) which is very valuable for SERS sensing.[4]

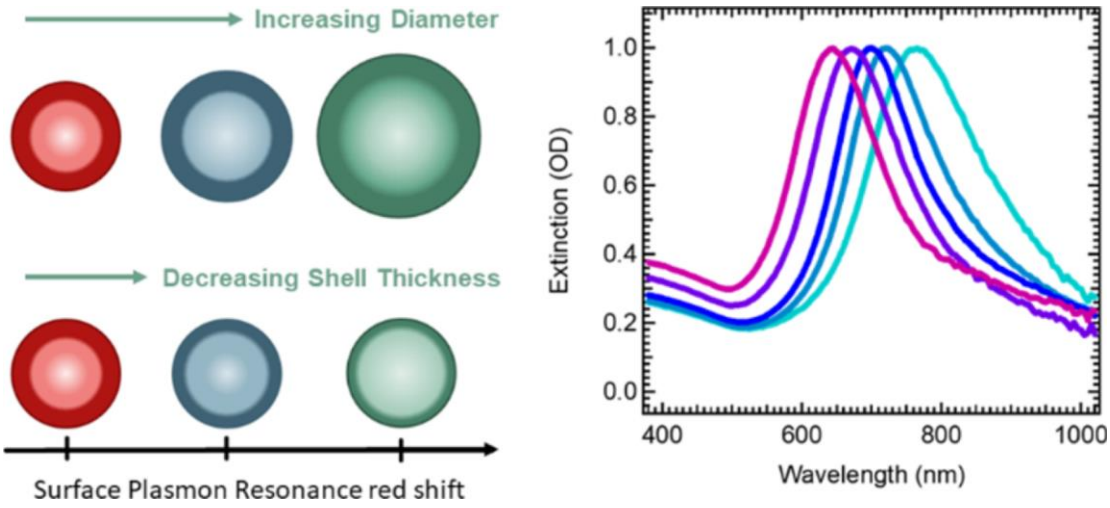

Figure 1.3. Increasing the nanoparticle diameter or decreasing the shell thickness of a hollow gold nanosphere red-shifts the extinction spectra.

SERS overcomes the low count of Raman scattered photons by utilizing plasmons to enhance the Raman scattering intensity. The SERS process, as seen in Figure 1.5, is a two-step process where incident light interacts with both the analyte and a metal nanoparticle to create a localized surface plasmon that couples to the molecule, significantly increasing the total scattered Raman light.[5-9] The intensity of the electric field for each process is E^2. The effect is an increase in scattering intensity proportional to E^4. Effective SERS substrates are tunable and have surface morphologies that further increase the localized electromagnetic field. The SERS intensity of a molecule may be described by Equation 1.6.

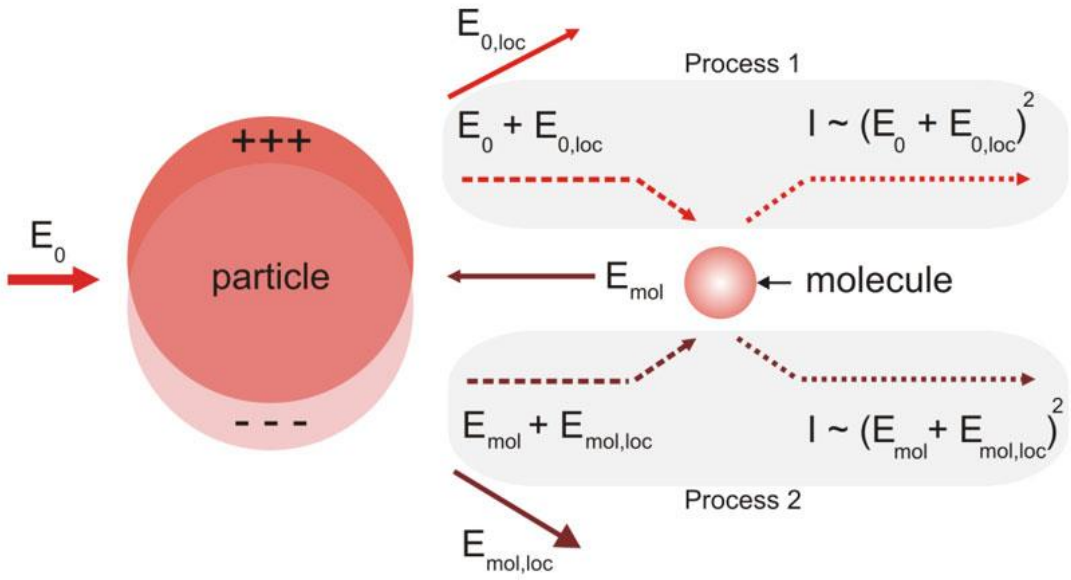

Figure 1.4. Diagram of the SERS enhancement mechanism. In process 1, an incident electric field (E_0) excites a metal nanoparticle localized surface plasmon which generates a large localized electric field ($E_{0,loc}$). In process 2, both the incident electric field and localized electric field interact with a molecule close to the surface of the nanoparticle. The Raman intensity of the molecule is enhanced by E^2 in each step.

$$\boldsymbol{I_{SERS}} \propto \boldsymbol{N \cdot \sigma_{SERS} \cdot \frac{|E_{loc}|^4}{|E_0|^4} \cdot |E_0|^2} \qquad \text{Equation 1.6}$$

Small changes to hollow gold nanoparticles' core size, shell thickness, and surface morphology cause their surface plasmon resonance to span the visible and NIR. Figure 1.3 shows how the changes to HGNs cause a broadly tunable LSPR. Increasing the core diameter and decreasing the shell thickness red-shifts the LSPR.[10] Multibranched nanostructures behave similarly to nanorods and nanospheres, meaning that the spikes have a transverse plasmon mode while the core retains a spherical plasmon mode. The spikes give broad LSPR and enable better electron confinement, increasing the electric field strength, thus increasing the Raman scattering intensity.

Figures 1.5 shows the extinction spectra of each category of SERS substrate used in this work: silver, gold, hollow, and multibranched nanoparticles. When plotted by wavelength, silver nanoparticles have the furthest blue-shifted localized surface plasmon resonance (LSPR) followed by solid gold nanoparticles. Hollow gold nanoparticles (HGNs) and gold nanostars have the most broadly tunable LSPR.

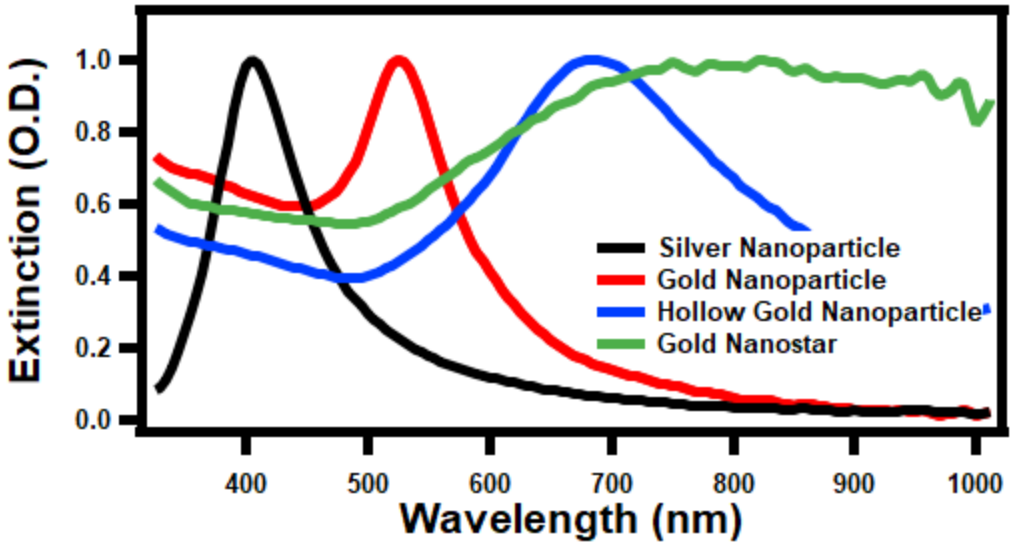

Figure 1.5 Extinction spectra of silver, gold, hollow, and urchin-like gold nanostar nanoparticles plotted by intensity vs wavelength.

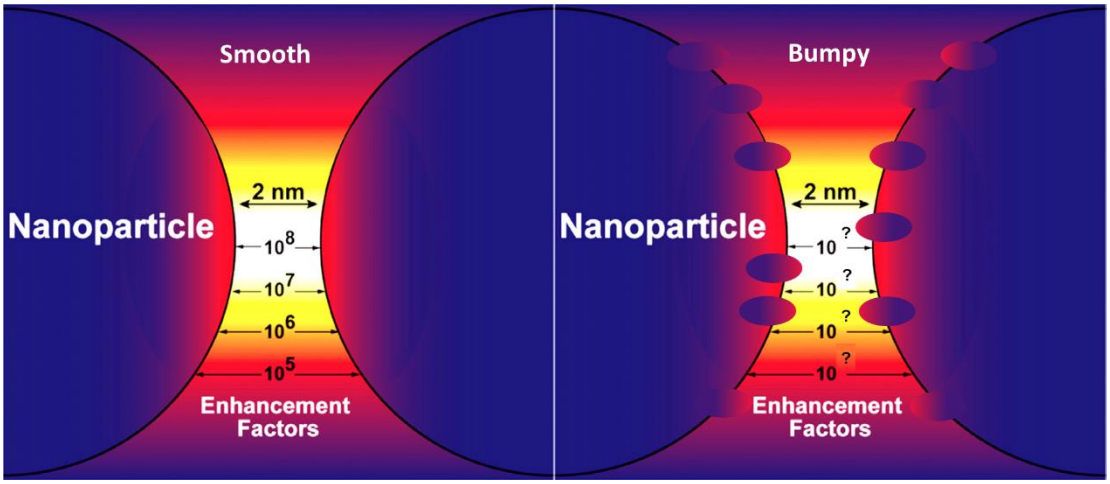

Figure 1.6. Illustration of the enhancement factor of surface roughened nanoparticles is theorized to be higher due to hot spots being closer in physical proximity.

1.3. Characterizing Nanomaterials Using Electron Microscopy

Transmission electron microscopy (TEM) is a high magnification measurement technique that images the transmission of a beam of electrons through a sample. Amplitude and phase variations in the transmitted beam provide imaging contrast that is a function of the sample thickness (the amount of material that the electron beam must pass through) and the sample material (heavier atoms scatter more electrons and therefore have a smaller electron mean free path than lighter atoms). Because this technique uses electrons rather than light to illuminate the sample, TEM imaging has a significantly higher resolution than light-based imaging techniques.

Successful imaging of nanoparticles using TEM depends on the contrast of the sample relative to the background. Samples are prepared for imaging by drying nanoparticles on a copper grid coated with a thin layer of carbon. Materials with electron densities that are significantly higher than amorphous carbon are easily imaged.

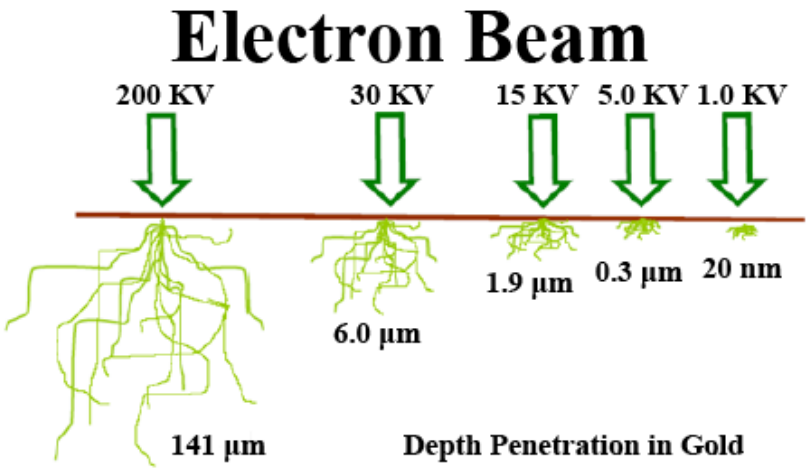

Figure 1.7. Illustration of the penetration depth of an electron beam with various voltages in gold from Kanaya-Okayama depth penetration formula.

$$R = \frac{0.0276\ A\ E^{1.67}}{Z^{0.89}\ \rho}\ \mu m \qquad \text{Equation 1.5}$$

R stands for depth penetration, A means atomic weight, E is the beam energy in KeV, Z is the atomic number, and ρ is the density in $\left(\frac{g}{cm}\right)^2$

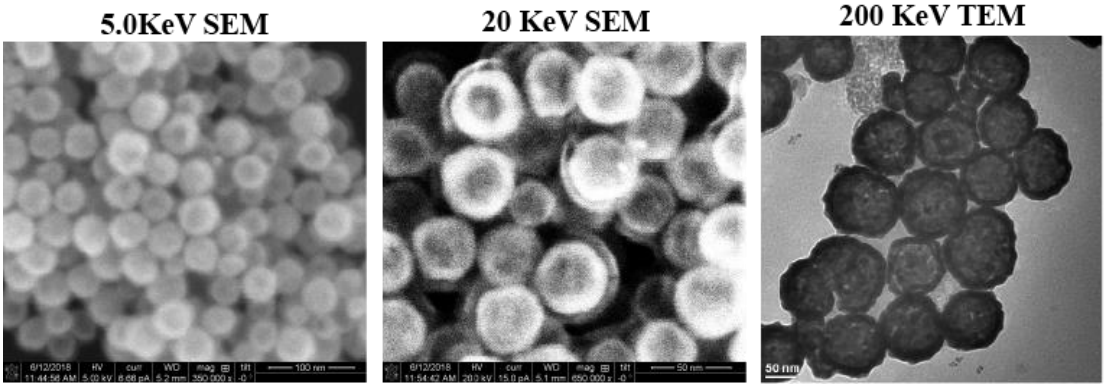

Figure 1.8. Comparison of electron microscopy images at an increasing voltage from left to right. Increasing electron volts increases the penetration depth and resolution of the image.

1.4. Conclusion

The sections introduced here give a background for the following chapters. Raman spectroscopy has the specificity and sensitivity to detect biomolecules of interest in aqueous solution. Unique plasmonic nanomaterials can be synthesized to enhance the Raman scattering intensity of weak Raman scatterers. Silver and gold nanomaterials were used as SERS substrates. The subsequent work focuses on integrating the benefits of a hollow cavity with multibranched gold nanostructures. The sensitivity was additionally increased by utilizing a hollow core photonic crystal fiber waveguide. Furthermore, a comprehensive analysis of the novel substrates was performed using absorption spectroscopy, elemental analytical techniques, electron microscopy, and electron tomography.

1.5. References

1. Bukasov, R.; Dossym, D.; Filchakova, O. Detection of Rna Viruses from Influenza and Hiv to Ebola and Sars-Cov-2: A Review. *Anal. Methods* **2021,** *13* (1), 34-55.
2. Dixon, M. G.; Schafer, I. J. Ebola Viral Disease Outbreak—West Africa, 2014. *MMWR. Morbidity and mortality weekly report* **2014,** *63* (25), 548.
3. Sarmiento-Ospina, A.; Vásquez-Serna, H.; Jimenez-Canizales, C. E.; Villamil-Gómez, W. E.; Rodriguez-Morales, A. J. Zika Virus Associated Deaths in Colombia. *Lancet Infect. Dis.* **2016,** *16* (5), 523-524.
4. Dong, E.; Du, H.; Gardner, L. An Interactive Web-Based Dashboard to Track Covid-19 in Real Time. *Lancet Infect. Dis.* **2020,** *20* (5), 533-534.

5. Lee, Y. L.; Liao, C. H.; Liu, P. Y.; Cheng, C. Y.; Chung, M. Y.; Liu, C. E.; Chang, S. Y.; Hsueh, P. R. Dynamics of Anti-Sars-Cov-2 Igm and Igg Antibodies among Covid-19 Patients. *J Infect* **2020,** *81* (2), e55-e58.
6. Jadhav, S. A.; Biji, P.; Panthalingal, M. K.; Murali Krishna, C.; Rajkumar, S.; Joshi, D. S.; Sundaram, N. Development of Integrated Microfluidic Platform Coupled with Surface-Enhanced Raman Spectroscopy for Diagnosis of Covid-19. *Med. Hypotheses* **2021,** *146*, 110356.
7. Yin, G.; Li, L.; Lu, S.; Yin, Y.; Su, Y.; Zeng, Y.; Luo, M.; Ma, M.; Zhou, H.; Orlandini, L.; Yao, D.; Liu, G.; Lang, J. An Efficient Primary Screening of Covid-19 by Serum Raman Spectroscopy. *J. Raman Spectrosc.* **2021**.
8. Ferreira, A. L.; de Lima, L. F.; Torres, M. T.; de Araujo, W. R.; de la Fuente-Nunez, C. Low-Cost Optodiagnostic for Minute-Time Scale Detection of Sars-Cov-2. *ACS Nano* **2021**.
9. Xu, K.; Chen, Y.; Yuan, J.; Yi, P.; Ding, C.; Wu, W.; Li, Y.; Ni, Q.; Zou, R.; Li, X. Factors Associated with Prolonged Viral Rna Shedding in Patients with Coronavirus Disease 2019 (Covid-19). *Clin. Infect. Dis.* **2020,** *71* (15), 799-806.
10. Lo, I. L.; Lio, C. F.; Cheong, H. H.; Lei, C. I.; Cheong, T. H.; Zhong, X.; Tian, Y.; Sin, N. N. Evaluation of Sars-Cov-2 Rna Shedding in Clinical Specimens and Clinical Characteristics of 10 Patients with Covid-19 in Macau. *Int. J. Biol. Sci.* **2020,** *16* (10), 1698.
11. McCreery, R. L. *Raman Spectroscopy for Chemical Analysis*; John Wiley & Sons: 2005; Vol. 225.
12. Bohren, C. F.; Huffman, D. R. *Absorption and Scattering of Light by Small Particles*; John Wiley & Sons: 2008.
13. Colthup, N. *Introduction to Infrared and Raman Spectroscopy*; Elsevier: 2012.
14. CLARK, R. H.; Hester, R. E. Infrared and Raman Spectroscopy. *Advances in Infrared and Raman Spectroscopy* **1984,** *11*.

15. Cañamares, M. V.; Pozzi, F.; Lombardi, J. R. Raman, Sers, and Dft Analysis of the Main Alkaloids Contained in Syrian Rue. *J. Phys. Chem. C* **2019,** *123* (14), 9262-9271.
16. Fleming, G. D.; Golsio, I.; Aracena, A.; Celis, F.; Vera, L.; Koch, R.; Campos-Vallette, M. Theoretical Surface-Enhanced Raman Spectra Study of Substituted Benzenes I. Density Functional Theoretical Sers Modelling of Benzene and Benzonitrile. *Spectrochim Acta A Mol. Biomol. Spectrosc.* **2008,** *71* (3), 1049-55.
17. Królikowska, A.; Cukras, J.; Witkowski, M.; Tymecka, D.; Hernik-Magoń, A.; Misicka, A.; Dzwolak, W. Sers and Dft Study of Noble-Metal-Anchored Cys-Trp/Trp-Cys Dipeptides: Influence of Main-Chain Direction and Terminal Modifications. *J. Phys. Chem. C* **2020,** *124* (13), 7097-7116.
18. Allen, A. C.; Efrem, M.; Mahalingam, U.; Guarino-Hotz, M.; Foley, A. R.; Raskatov, J. A.; Song, C.; Lindley, S. A.; Li, J.; Chen, B.; Zhang, J. Z. Hollow Gold Nanosphere Templated Synthesis of Pegylated Hollow Gold Nanostars and Use for Sers Detection of Amyloid Beta in Solution. *J. Phys. Chem. B* **2021,** *125* (44), 12344-12352.
19. Chang, R. *Surface Enhanced Raman Scattering*; Springer Science & Business Media: 2013.
20. Van Duyne, R. P. Laser Excitation of Raman Scattering from Adsorbed Molecules on Electrode Surfaces. *Chem. Biochem. Appl. Lasers* **1979,** *4*, 101.
21. Kim, S. K.; Kim, M. S.; Suh, S. W. Surface-Enhanced Raman Scattering (Sers) of Aromatic Amino Acids and Their Glycyl Dipeptides in Silver Sol. *J. Raman Spectrosc.* **1987,** *18* (3), 171-175.
22. Kneipp, K.; Wang, Y.; Kneipp, H.; Perelman, L. T.; Itzkan, I.; Dasari, R. R.; Feld, M. S. Single Molecule Detection Using Surface-Enhanced Raman Scattering (Sers). *Phys. Rev. Lett.* **1997,** *78* (9), 1667.

23. Cyrankiewicz, M.; Wybranowski, T.; Kruszewski, S. Study of Sers Efficiency of Metallic Colloidal Systems. *Journal of Physics: Conference Series* **2007,** *79*, 012013.
24. McQuillan, A. J. The Discovery of Surface-Enhanced Raman Scattering. *Notes and Records of the Royal Society* **2009,** *63* (1), 105-109.
25. Lindley, S. A.; Cooper, J. K.; Rojas-Andrade, M. D.; Fung, V.; Leahy, C. J.; Chen, S.; Zhang, J. Z. Highly Tunable Hollow Gold Nanospheres: Gaining Size Control and Uniform Galvanic Exchange of Sacrificial Cobalt Boride Scaffolds. *ACS Appl. Mater. Inter.* **2018,** *10* (15), 12992-13001.

CHAPTER 2

Detection of Saturated Fatty Acids Associated with a Self-Healing Synthetic Biological Membrane Using Fiber-Enhanced Surface Enhanced Raman Scattering

2.1 Abstract

The Synthetic Biological Membrane (SMB) project designed a novel biomaterial to improve the reliability of NASA's next-generation water recycling systems modeled after the human small intestine. This membrane is designed to recover from chemical, physical, and oxidative damage caused by calcium scaling, organic fouling, and cosmic radiation-induced reactive species.[1,2,3] The SBM is a semipermeable membrane made of two layers of phospholipids in contact with genetically engineered organisms that hyper-express fatty acids, which provide a protective layer to the active side of the membrane.[4,5] The SBM, as shown in Figure 2.1, was configured to be integrated into a forward osmosis purification system for wastewater treatment applications. Forward osmosis membranes are semipermeable membranes that separate two solutions of different solute concentrations driven by the osmotic potential difference.[6] The lipid membrane has been engineered to be permeable to fatty acids that will be transported across the membrane.[7] Once on the feed side of the membrane, the fatty acids either precipitate from the solution then adhere to the membrane creating a protective layer or react with contaminants in the solute layer that builds up adjacent to this side of the membrane. Solubilized fatty acids have previously been characterized *in vitro* using gas chromatography; however, a more sensitive and non-destructive technique is needed to integrate the SBM into a forward osmosis purification system for wastewater treatment applications.[8,9]

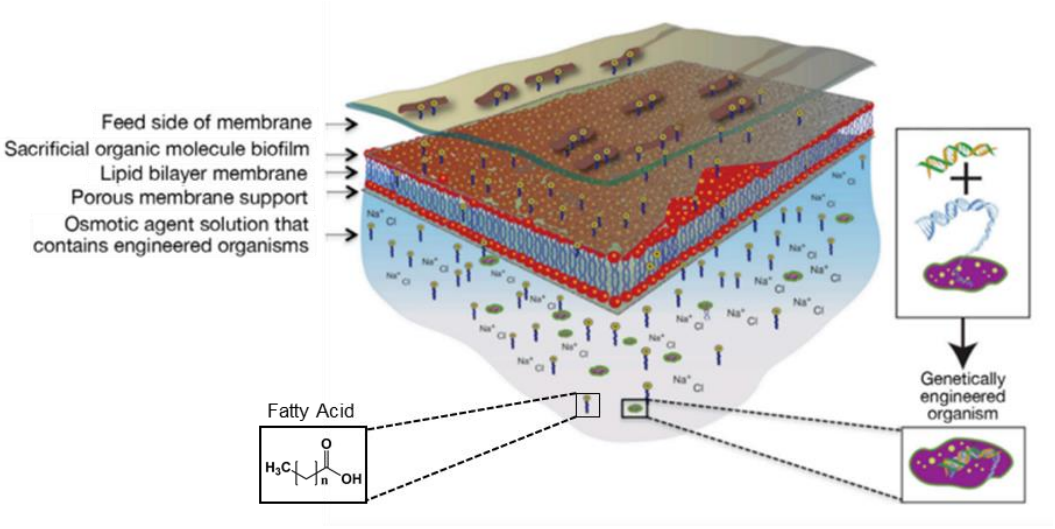

Figure 2.1. Overview of the Synthetic Biological Membrane displaying the overall design and how the phospholipid bilayer can be repaired with Fatty Acids that are produced by genetically engineered organisms.

Raman spectroscopy is an excellent technique for characterizing the C-C and C-H bonds in fatty acids.[10,11,12,13] This technique has been used to study the differentiate fatty acids in various oils, profile lipid content and unsaturation, and characterize the health of cell tissue. [10,14,15,16, 17] The hydrocarbon backbone found in fatty acids has multiple Raman active modes which can be divided into three regions: (I) the low-frequency region below 400 cm^{-1} associated with phonons of the crystal lattice vibrations, (II) the skeletal optical mode between 1000 cm^{-1} and 1500 cm^{-1} associated with different conformations such as gauche and trans, and (III) the complex C-H stretching region above 2700 cm^{-1} containing overtones of low-order vibrations and several vibrations associated with chain packing.[18]

2.2 Challenges with Studying Saturated Fatty Acids

In the SBM project, the fatty acid molecules of interest are decanoic acid, myristic acid, palmitic acid, and stearic acid, and their chemical structures are shown in Figure 2.2. The Raman band associated with the hydrocarbon backbone and the carboxylate group have been well characterized.[11,18,19,20] The distinguishing Raman shifts are primarily found in Region II: C-C trans stretch around 1063 cm^{-1} and 1128 cm^{-1}, C-C gauche around 1100 cm^{-1}, and CH_2 twist around 1296 cm^{-1}. The chain length of the fatty acid causes small shifts in the peak location, allowing for spectroscopic differentiation.

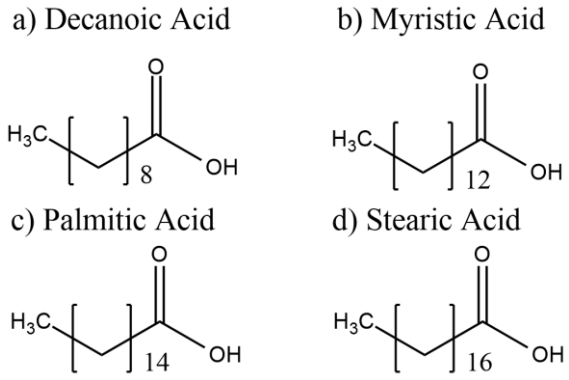

Figure 2.2. The chemical structure of the four fatty acids consists of a tail length of (a) 9 carbons for decanoic acid, (b) 13 for myristic acid, (c) 15 for palmitic acid, and (d) 17 for stearic acid.

Raman spectroscopy alone is insufficient for studying solubilized fatty acids due to their low solubility at ambient temperature.[21,22] Plasmonic nanomaterials such as silver nanoparticles increase the local electric field by $E^{4,}$ enabling ultrasensitive

detection via Surface-enhanced Raman scattering (SERS). SERS enhancements originate from the excitation wavelength of the laser stimulating resonant electronic oscillations in the SERS substrate. The localized electronic oscillations generate a large local electric field. The total electromagnetic field excites molecules close to the surface of the SERS substrate. The improvement of SERS depends on the metal nanoparticle size and shape.[23] The enhancement factor A series of experiments starting in 1985 demonstrated the capabilities of SERS for characterizing fatty acids and distinguishing lipids based on fatty acid content. Moskovits and Suh found that carboxylate ions bind to silver surfaces as evidenced by Raman shifts at 930 cm^{-1} and 1400 cm^{-1}.[24] The binding event alters the vibrational frequency of the carboxylate head and aliphatic tail resulting in small shifts in peak position compared to crystalline spectra. Suh and Weldon *et al.* further characterized the phonon vibrations in Regions I and III in palmitic acid and triglycerides. [15,25] These studies elucidated the differences in peak position, full width at half the maxima for SERS measurements of fatty acids.

2.2.1 Raman Fiber Probes Used for Reaction Monitoring

Raman spectrometers with a fiber optic probe have been used to monitor chemical reactions in both *in situ and ex situ* methods. *In* situ denotes the probe was immersed into the reaction vessel, and *ex situ* denotes the probe was placed outside of the reaction vessel to perform "real-time" monitoring and analysis of any reaction as seen in Figure 2.3. The *ex situ* probe allows for fast monitoring that is easy to use, noninvasive, and requires little to no sample preparation. Utilization of this *ex situ* analytical tool ranges in disciplines from art conservation analysis to forensic science.

Raman spectroscopy lacks widespread use to monitor reactions in an aqueous medium, especially *ex situ* real-time reaction monitoring, despite its capability.

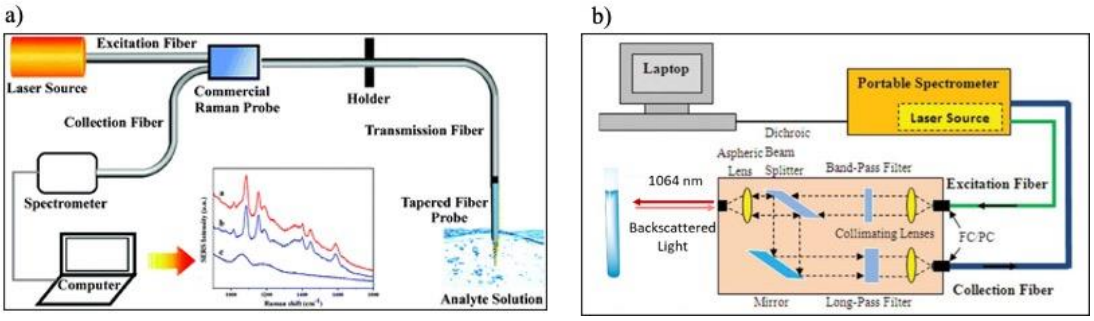

Figure 2.3. a) An example of the setup for an *in situ* reaction monitoring with Raman spectroscopy. b) An example of the setup for an *ex situ* reaction monitoring with Raman spectroscopy.

Raman spectroscopy has been used to monitor some organic reactions. Many of them involve the *in situ* method, or the reactions occur under neat or organic solvents, which have distinct signals that may obscure the signal of interest. For instance, the synthesis of substituted imidazoles and epoxides were two reactions where *in situ* Raman spectroscopy was used to monitor the reaction mixtures' progress. In both reactions, an immersible probe was dipped into the reaction flask, and as the reaction progressed, scans were taken to monitor the decrease of the reactant signals and the increase of the product signals. After normalizing the Raman signals and isolating distinct signals relating to starting materials and products, the Raman data could be plotted against time. By doing this, researchers were able to identify the moment when the reactions reached completion.

Accordingly, aqueous reductions of nitroarenes and ketones, using a nickel boron composite (NBC) catalyst and dimethylamine borane, respectively, were undertaken to evaluate the utility of *ex situ* Raman spectroscopy (Figure 2.4). The instrument's sensitivity in calculating reaction kinetics and substrate selectivity demonstrate the efficacy and practicality of this analytical tool. Herein, we report the viability of using Raman spectroscopy as *ex situ*, real-time, and noninvasive reaction monitoring technique for reactions in aqueous medium.

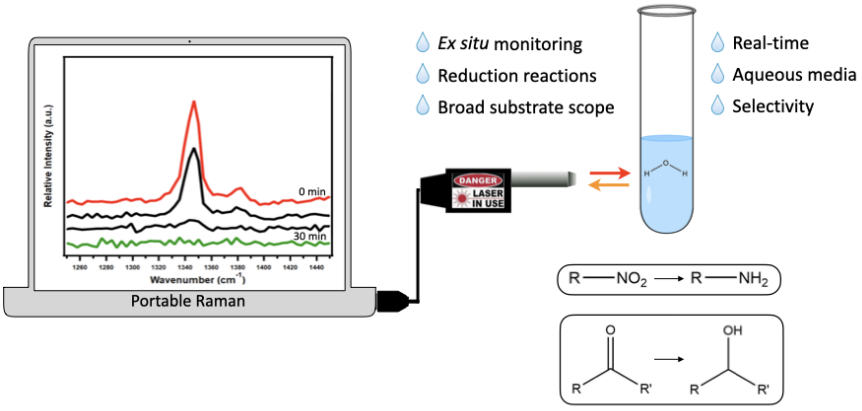

Figure 2.4. *Ex situ* reaction monitoring with Raman spectroscopy for aqueous reduction reactions.

Tri-nitroarenes are explosive compounds that may be neutralized by chemical reduction in aqueous media before safe disposal. Advantageously, the aromatic nitro groups exhibit Raman signals (1330 – 1370 cm^{-1}) and thus enable the safe real-time monitoring of the transformation to more innocuous amines. The facile reduction of 4-nitrotoluene to the amine was achieved using a catalysis procedure. The nitro group is reduced to the amine using a nickel boron composite (NBC) catalyst (Scheme 2.1).[26]

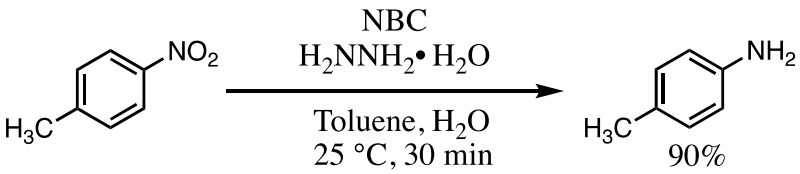

Scheme 2.1. Reduction of 4-nitrotoluene to 4-toluidine (90% isolated yield) using NBC catalyst and hydrazine hydrate.

We were able to continuously monitor the nitro group reduction by positioning the fiber optic probe against the test tube. The laser focal point was focused just inside the vial glass wall to collect a signal from the reaction mixture. This *ex situ* technique is convenient because it avoids the need for an immersion probe or the need to remove aliquots for analysis. The reduction of 4-nitrotoluene was considered complete when the nitro group signal (1350 cm^{-1}) was no longer observed or was undifferentiated from the baseline noise and completed within 30 min (Figure 2.5).

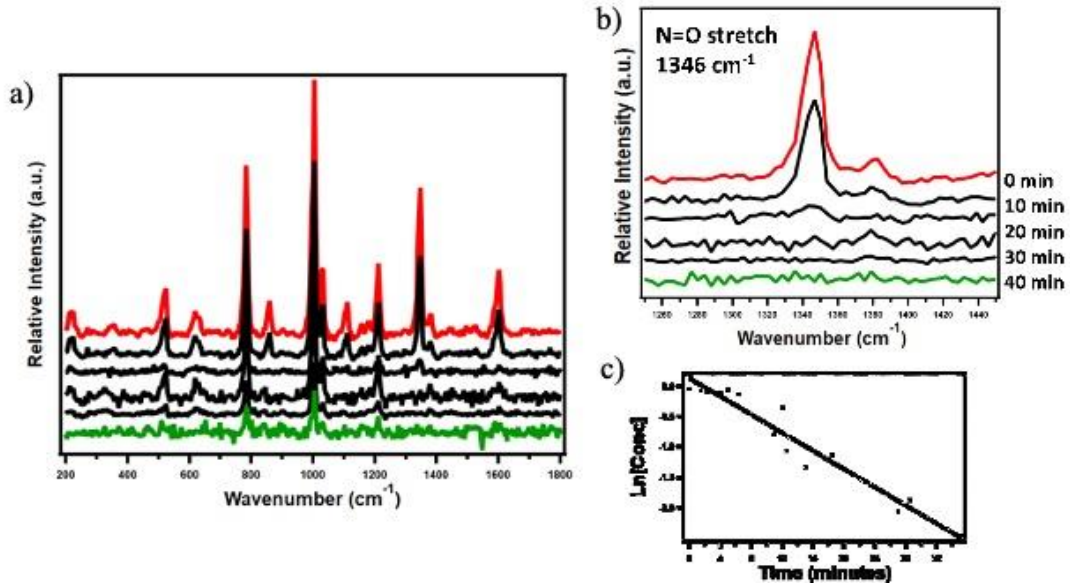

Figure 2.5. a) *Ex situ* Raman monitoring of the reduction of 4-nitrotoluene catalyzed with NBC catalyst and hydrazine hydrate in toluene at 25 °C. Red and green highlight the start and end of the reaction. b) A plot of the natural log of concentration vs. time to extract the rate constant of the nitro reduction reaction.

Visually, the reaction mixture transformed from a yellow solution to a turbid yellow mixture, and then finally to a clear colorless solution (Figure 2.6). Quantitative product formation was confirmed by determining ^{1}H NMR spectrum of the isolated product, which showed signals corresponding to the complete conversion of 4-nitrotoluene to 4-toluidine.

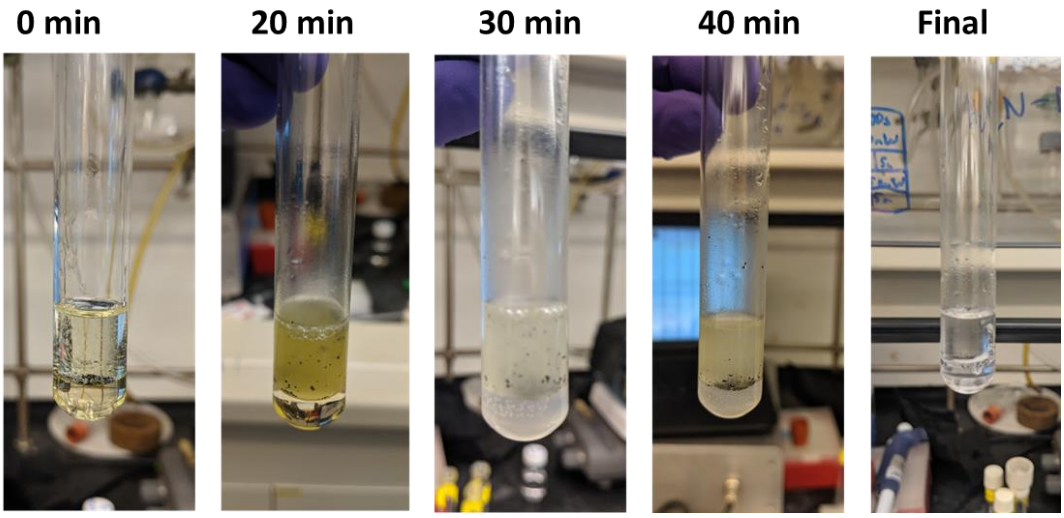

Figure 2.6. Photographs showing the reduction of 4-nitrotoluene at various time points. Overtime the reaction mixture transforms from clear and yellow to turbid and yellow/colorless to a clear and colorless solution.

A calibration curve of 4-nitrotoluene was used to determine the concentration of the reactant as the reaction proceeded. Before initiating the reaction or reagent addition, the intensity of the nitro stretch at 10 concentrations between 1.0 M and 0.01 M were measured and normalized to a toluene co-solvent peak at 1379 cm^{-1} (Figure 2.6). The rate of reaction could then be determined. By comparing the normalized peak intensity of 4-nitrotoluene as the reaction progressed over time, Raman spectroscopy provided a straightforward method to calculate that the reduction follows a pseudo first order rate law (Equation 1).

$$Ln[C(t)] = kt + Ln[C(0)]; k = -0.018 \pm 0.003; C(0) = 1.0\ M \qquad \text{Equation 1}$$

2.2.2. Use of Photonic Crystal Fibers for Raman Spectroscopy

Recently, several groups have employed photonic crystal fibers (PCF) as optical waveguides to develop *in situ* detection methods for gases and liquids. This technique has been referred to as fiber-optic Raman spectroscopy and fiber enhanced Raman spectroscopy.[26,27,28,29] The two predominant types of PCF used in SERS-based molecular detection are hollow core photonic crystal fibers (HCPCF) and solid-core photonic crystal fibers (SCPCF). Both have a two-dimensional photonic bandgap where allowed wavelengths propagate along the direction of the fiber. However, spectra collected using SCPCF have a significant Raman background of SiO_2.[30,31,32] PCF offers even more advantages to SERS-based molecular sensors because fiber optic probes can be used as *in situ* sampling probes, require only a few hundred nanoliters per sample volume, operate with portable Raman systems, and have reported a 10x increased enhancement in the Raman signal.[32,33,34]

In this chapter, we first investigated the limits of detection of decanoic acid, myristic acid, palmitic acid, and stearic acid using silver nanoparticles prepared using hydroxylamine to nucleate aqueous silver ions. Then we evaluated the detection capabilities of SCPCF and HCPCF (both used together with SERS) to find the best PCF to use in an *in situ* method for monitoring the repair process of the SBM. The combined advantages of SERS for Raman enhancement and efficient collection of signals due to waveguiding property of the HCPCF provide the necessary sensitivity of molecules that have relatively small polarizability or Raman signal, such as fatty acids.

2.3. Results and Discussion

Figure 2.7 illustrates the methodology of the subsequent experiment. First, an aliquot of freshly prepared silver sols was mixed with each fatty acid sample. Then the analyte was loaded into the hollow core photonic crystal fiber waveguide using capillary action. The samples were aligned in the fiber chuck then analyzed using Raman spectroscopy. The samples prepared with silver sols experienced appreciable enhancement making detection of each fatty acid possible. Additionally, the fiber optic waveguide increased the interaction of the light with the analyte, which augmented the SERS enhancement.

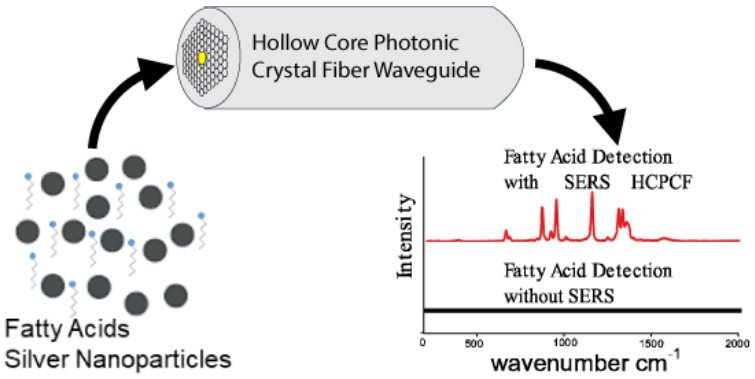

Figure 2.7. Capillary action loads a mixture of fatty acid and silver nanoparticles into a hollow core photonic crystal fiber waveguide then the chemical identification via SERS.

2.3.1 Determination of Concentrations of Fatty Acid Solutions

Decanoic, myristic, palmitic, and stearic acids all have low solubility in water. The total concentration of each fatty acid in the solution was found by calculating the solubility limit and measuring the TOC of each stock solution. The concentrations

presented in Table 2.1 were calculated using the TOC results in mg/L. The concentration was expected to decrease with increasing aliphatic tail length; thus, decanoic and myristic acids would be lower than palmitic and stearic acids. Decanoic, myristic, and palmitic acid concentrations were above the instrument limit of detection and approximately followed the expected trend. The fatty acid with the longest hydrocarbon tail had an exceedingly low solubility resulting in a concentration below the instrument's detection limit. The published solubility of stearic acid at 300 K is 11 mM. This value was expected to be the smallest concentration. However, 11 mM is nearly 100 times higher than palmitic acid, which indicates that the actual concentration in this instance is likely much lower than reported.[21]

Table 2.1. Results of the TOC analysis and the resulting concentration of each fatty acid.

Sample	TOC (mg/L)	pH	Concentration (mM)
Decanoic Acid	45	9	0.469
Myristic Acid	83	11.8	0.494
Palmitic Acid	17	11.7	0.089
Stearic Acid	Idl*	10.1	11.2**

*Idl = lower than the detection limit; **concentration calculated from published solubility in water at 30 ^{o}C.[21]

2.3.2. Characterization of SERS Substrate and HCPCF

A modified Lee-Meisel synthesis using hydroxylamine hydrochloride, a weaker reducing agent, produced silver nanoparticles with an average diameter of 53 ±18 nm.[35, 36] Figure 2.8 shows the electronic absorption and SEM/TEM results of the silver

nanoparticles. The change of reducing agent resulted in a more red-shifted surface plasmon resonance of 415 nm, as seen in Figure 2.8a, indicating larger nanoparticles comparable to Leopold and Lendl's results.[36] This is desirable because the SPR is closer to the Raman laser excitation wavelength of 514.5 nm. This synthesis has a larger distribution of sizes, as seen in Figure 2.8b. Representative SEM images can be seen in Figures 2.8c and 2.8d where Figure 3c is a scanning mode SEM image and Figure 2.8d is a transmission mode SEM image. Nanoparticles of size greater than 70 nm tend to be semi-spherical aggregates of smaller particles, as shown in Figure 2.8c. However, nanoparticles of size less than 50 nm are spherical and aggregated, as shown in Figure 2.8d. Figure 2.8b shows that the distribution of particles centers around fully coalesced and thus spherical nanoparticles. The TEM image in Figure 2.8e displays four nanoparticles (38 nm, 48 nm, 58 nm, 68 nm) with a single crystalline domain confirming that the particles are not aggregates of smaller particles.

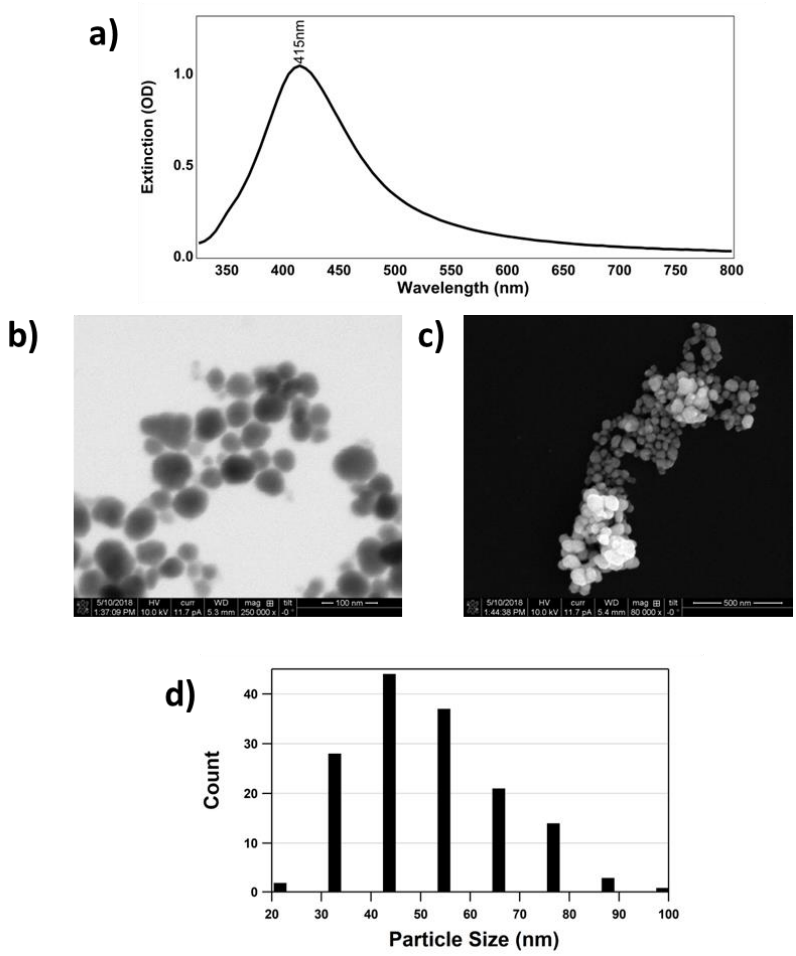

Figure 2.8. (a) Extinction spectra of the silver nanoparticle SERS substrate. (b) The distribution of particle sizes of the synthesis. SEM images of the SERS substrate. (c) Scanning-mode SEM image of nanoparticles with scale bar representing 200 nm. (d) Transmission-mode SEM image with scale bar representing 100 nm. (e) TEM image of the silver nanoparticles.

The PCF+SERS measurements were performed in a method similar to Gu *et al*.[34] Figure 2.9 shows the experimental fiber setup. Two objective lenses are used to focus the laser light into the core of the PCF. The distances between the objectives and the PCF were first calculated based on numerical aperture then experimentally optimized to have a bare fiber coupling efficiency above 30%. Figure 2.9a shows an

example schematic for clarity, and Figure 2.9b shows the typical set up with a 50x objective focusing the laser light into the photonic crystal fiber, and the transmitted light is collimated using a 5x or 10x objective then focused back into the fiber. Figures 2.9c and 2.9d show the surface of a cleaned HCPCF and a closer image of the cladding.

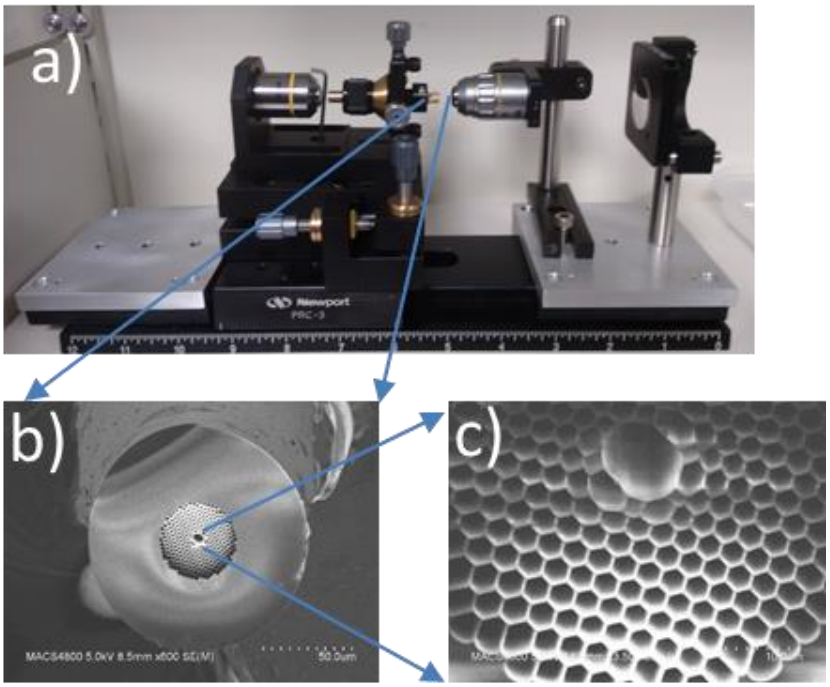

Figure 2.9 (a) Bare fiber coupling where the laser light is focused onto the fiber using an objective then recollected using another objective and (b) the experimental set up where the fiber is outlined in red. (c) SEM image of the hollow core photonic crystal fiber where the scale bar is 50 µm and (d) a close-up SEM image of the core and cladding of the fiber where the scale bar is 5µm.

2.3.3 Raman, SERS, and Fiber-Assisted SERS Measurements

Each fatty acid was characterized by Raman spectroscopy, SERS, and PCF-assisted SERS. The Raman spectra in Figure 2.10a were collected using a crystalline sample of each fatty acid. They identically matched the previously reported spectra from Moens *et al.*[13] Figures 5b-d display the crystalline samples dissolved in water,

representing SERS and SERS + HCPCF spectra, respectively. Table 2.2 summarizes the experimental and published Raman shifts and their assignments.[18, 24] There is a lack of published values for decanoic acid. Still, the unreported peak positions at 893 cm^{-1}, 1063 cm^{-1}, 1297 cm^{-1}, 1410 cm^{-1}, and 1433 cm^{-1} differ by less than 5 cm^{-1} from the corresponding Raman shifts in the other fatty acid samples. The Raman spectra of the aqueous stock solution as seen in Figure 2.10b contained no discernible fatty acid peaks, and the only peak present is associated with a bending mode of water at 1645 cm^{-1}. Figure 2.10c shows a representative SERS spectrum of each fatty acid sample and the Raman spectrum of a 3x washed silver nanoparticle solution. In the SERS spectra, additional peaks appear at 923 cm^{-1} and 1395 cm^{-1}, which have been associated with carboxylate groups bound to the surface of colloidal silver. The silver nanoparticle solution independently has peaks at 771 cm^{-1}, 927 cm^{-1}, 1100 cm^{-1}, 1128 cm^{-1}, and 1398 cm^{-1}. The peaks in the silver nanoparticle solution at 1100 cm^{-1} and 1128 cm^{-1} overlap with two characteristic peaks in the fatty acid samples at 1090 cm^{-1} and 1124 cm^{-1}. Therefore, the peaks at 890 cm^{-1}, 1062 cm^{-1}, and 1296 cm^{-1} were used to find the detection limit. Figure 2.10d shows a representative HCPCF measurement for each fatty acid and the Raman spectrum of a cleaned HCPCF. Further discussion of the SERS and HCPCF data follows.

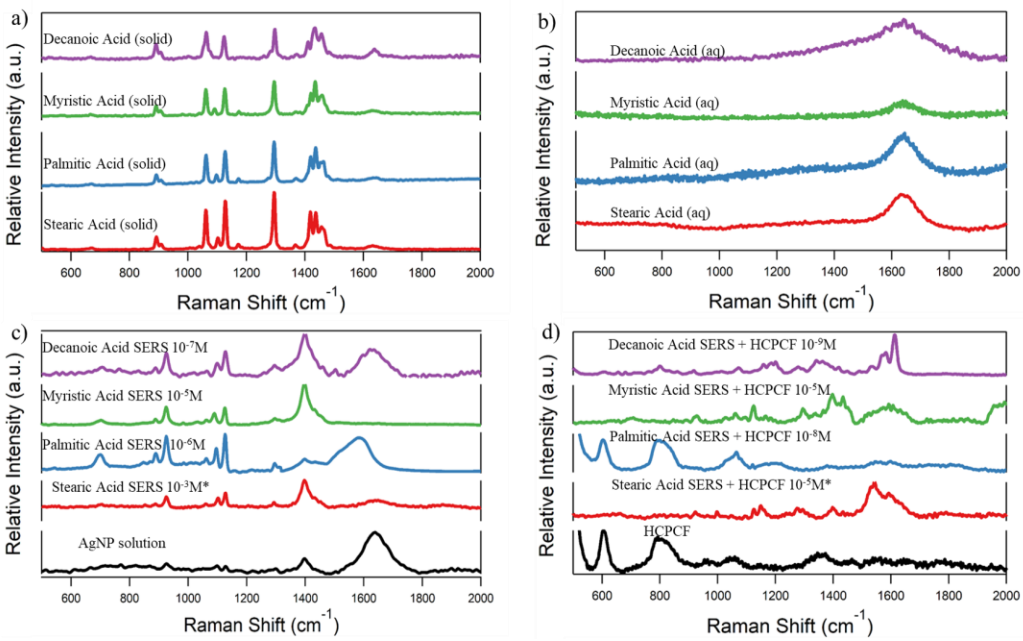

Figure 2.10. Comparison of the (a) crystalline Raman spectra (b) aqueous Raman spectra (c) SERS spectra and (d) SERS + HCPCF spectra of decanoic (purple), myristic (green), palmitic (blue) and stearic (red) acids.

Table 2.2. Assignment of Raman bands of crystalline decanoic, myristic, palmitic, and stearic acids and comparison of differences between the database and experimental values.

		Raman Shift (cm^{-1})			Raman Shift (cm^{-1})			Raman Shift (cm^{-1})			Raman Shift (cm^{-1})	
Assignment	**Fatty Acid**	**Lit.**	**Exp.**	**Fatty Acid**	**Lit.**	**Exp.**	**Fatty Acid**	**Lit.**	**Exp.**	**Fatty Acid**	**Lit.**	**Exp.**
COO^-	Decanoic Acid	-	893	Myristic Acid	893	891	Palmitic Acid	893	894	Stearic Acid	890	892
C-C (trans)		1062	1063		1063	1061		1063	1062		1062	1061
C-C (gauche)		-	-		1092	1091		1099	1098		1100	1103
C-C (trans)		1123	1124		1128	1126		1129	1127		1129	1128
CH_2 twist			1297		1296	1295		1296	1295		1296	1295
CH_2 sciss		-	1433		1438	1435		1438	1437		1441	1437

The results of the SERS analysis of decanoic, myristic, palmitic, and stearic acids are displayed in Figure 2.11a-d. The Raman shifts associated with molecular vibrations from the aliphatic chain (C-C and C-H), carboxylic acid (C-COO^-), and additional shifts associated with vibrations from the carboxylic acid coordinating to the silver nanoparticle surface. When the carboxylate ion binds to the surface of the silver substrate, the Ag-COO^- bond at 1400 cm^{-1} experiences the most enhancement in the signal due to the strong distance dependence of SERS. In all the SERS spectra, the strongest peak is at 1400 cm^{-1}. An additional peak associated with C-COO^- at 923 cm^{-1} also appears in the SERS spectra. Fitting the SERS spectra with Lorentzian peaks revealed that the broad peak at 1400 cm^{-1} can be decomposed into individual peaks at 1399 cm^{-1}, 1370 cm^{-1} and 1410 cm^{-1}. The shift at 1399 cm^{-1} is associated with COO- binding to silver, but the other two peaks have ambiguous assignments in literature. They are possibly due to different binding modes of the COO^- on the Ag nanoparticles. In this study, the primary objective was to find the lowest possible limit of detection for each fatty acid. The detection limits were found using the Raman shifts associated with COO^-, C-C (trans), and CH_2 twist labeled in Figure 2.11. The limits of detection were determined to be: 10^{-9} M for decanoic acid, 10^{-8} M for myristic acid, 10^{-9} M for palmitic acid, and 10^{-6} M for stearic acid.

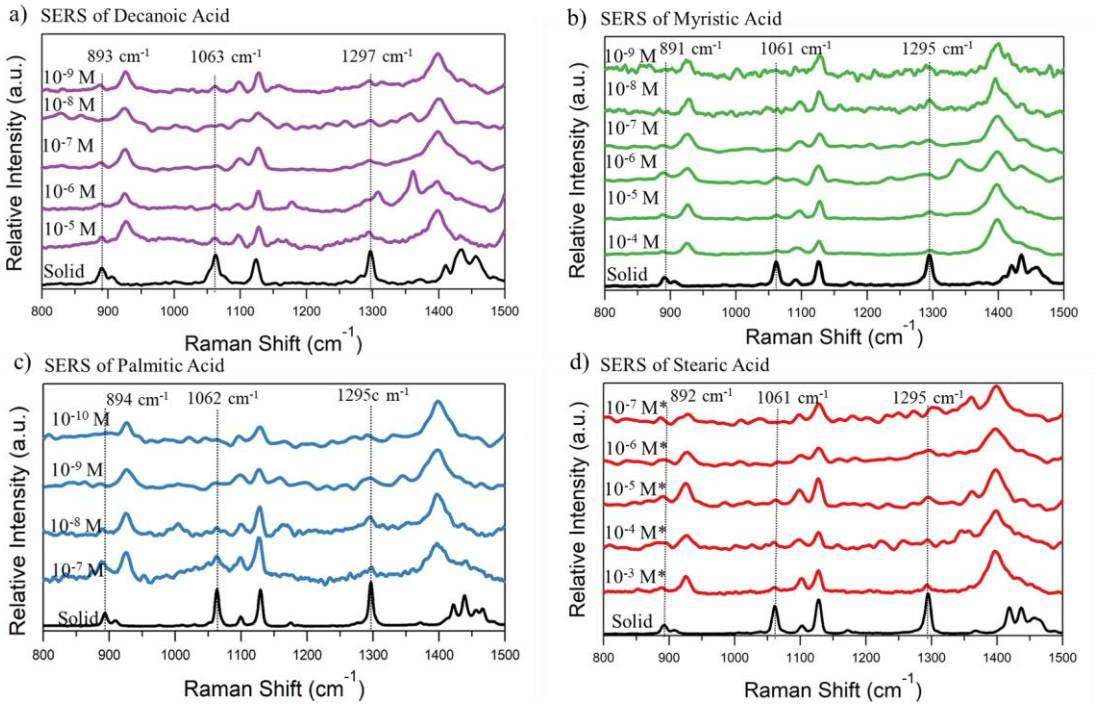

Figure 2.11. SERS spectra of the dilution series used to determine the lowest detectable signal of (a) decanoic acid, (b) myristic acid, (c) palmitic acid, and (d) stearic acid.

The aliphatic chain (C-C and C-H) and carboxylic acid ($C\text{-}COO^-$) peaks in the 890 cm^{-1}, 1060 cm^{-1}, and 1290 cm^{-1}regions decrease with decreasing concentration while the $Ag\text{-}COO^-$ peaks at 923 cm^{-1} and 1300 cm^{-1} decrease to a minimum. The SERS data for palmitic acid was plotted as a function of concentration, as seen in Figure 2.11. The Raman shifts at 894 cm^{-1}, 1062 cm^{-1}, and 1295 cm^{-1} decreased in intensity with decreasing concentration until they were no longer discernible at 10^{-9} M. The Raman shift at 1128 cm^{-1} and 1098 cm^{-1}also decreased with concentration until 1.0 nM where the peak intensity remained constant This indicates that the C-C (gauche) and C-C

(trans) vibrations could have contributed to the signal intensity. Still, the residual signal intensity is from the silver nanoparticle solution.

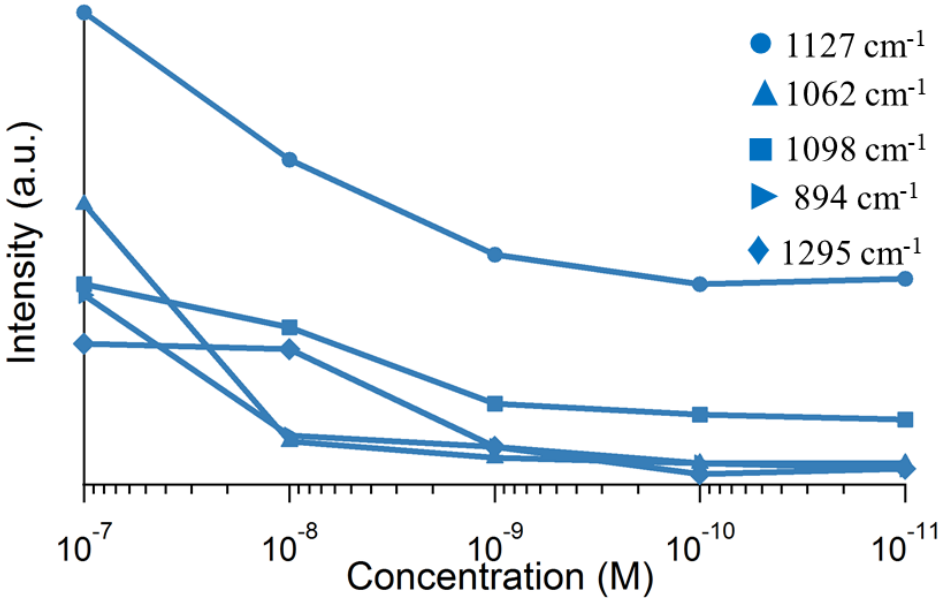

Figure 2.12. SERS detection results of palmitic acid as a function of concentration for the specified wavenumbers.

The SERS and SERS + PCF spectra of 10^{-5} M stearic acid are shown in closer detail in Figure 2.13. Both the SERS + HCPCF and SERS + SCPCF spectra show two peaks at 1546 cm^{-1} and 1590 $cm^{-1,}$ which could be associated with an enhancement of the SiO_2 background. The SERS + HCPCF spectra show enhancement of the Raman shifts at 892 cm^{-1}, 1103 cm^{-1}, 1128 cm^{-1}, 1295 cm^{-1}, and 1400 cm^{-1} as similar to the SERS spectra, but the spectra for SERS + SCPCF is primarily dominated by a large SiO_2 background with a low intensity 1395 cm^{-1} peak. Table 2.3 shows values for the SERS and SERS + HCPCF results. Columns 2 and 3 were normalized to the SERS +

HCPCF 1400 cm^{-1} peak. Column 4 shows the result if the SERS + HCPCF data were at the same power level as the SERS data. The enhancement of using an HCPCF as seen in column 5 was calculated by dividing the SERS + HCPCF data in column 4 by the SERS data in column 2. The Ag-COO^- intensity was increased 11 fold while the CH_2 twist intensity was increased by 18 fold. Enhancement from the HCPCF is believed to result from better light confinement along the fiber's core, which results in increased Raman scattering from the analyte molecules. The variable enhancement is likely from the core of the HCPCF, restricting the orientation of the fatty acid molecules. The resulting anisotropy causes an asymmetric increase in signal for molecular vibrations.

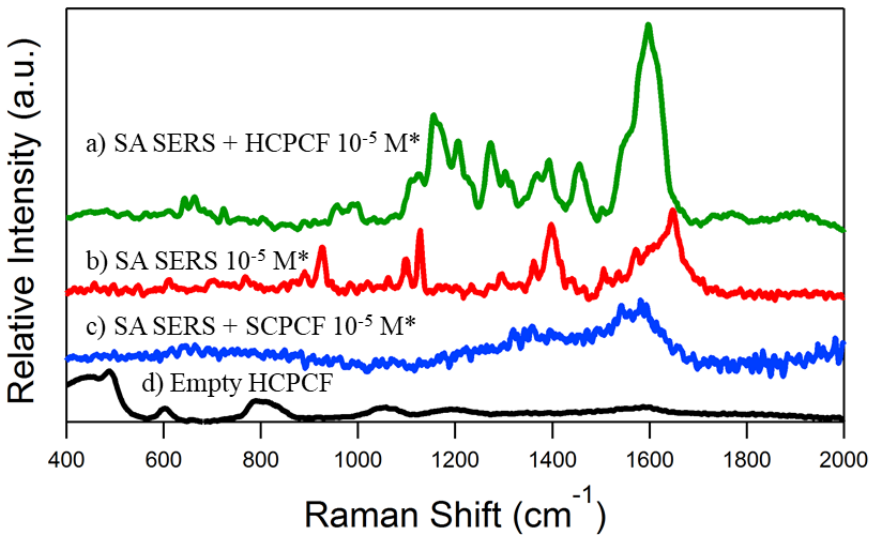

Figure 2.13. SERS spectra of 10^{-5} M stearic acid samples (a) SERS + HCPCF only (b) SERS, (c) SERS + SCPCF (d) Raman spectrum of an empty HCPCF where the * indicates that the actual concentration is likely lower than reported.

Table 2.3. Comparison of SERS and SERS + HCPCF peak intensity ratios for stearic acid.

Column 1	Column 2	Column 3	Column 4	Column 5
Raman Shift (cm^{-1})	**SERS Intensity** rel. to Col. 3 1400cm^{-1}	**SERS + HCPCF Intensity** rel. to 1400cm^{-1}	**SERS + HCPCF Intensity** Norm. for 60% power loss	**Enhancement** Calculated by $\frac{Col.4\ Value}{Col.2\ Value}$
892	0.03	0.12	0.20	6.81
927	0.01	0.41	0.68	6.69
1103	0.07	0.59	0.98	13.43
1128	0.15	1.01	1.69	11.49
1295	0.04	0.40	0.63	17.98
1400	0.15	1.00	1.67	10.87

2.4 Conclusion

There previously lacked a reliable method to evaluate the progression of the repair process of the SBM. In this work, we demonstrate the detection of decanoic, myristic, palmitic, and stearic acids in aqueous media using non-destructive and *in situ* SERS + HCPCF. The limit of detection determined using the SERS results was 10^{-6} M for stearic acid, 10^{-9} M for palmitic acid, 10^{-8} M for myristic acid, and 10^{-9} M for decanoic acid. The addition of the HCPCF provided an 18-fold enhancement of the CH_2 twist vibration at 1295 cm^{-1} and variable enhancements for the other aliphatic chain (C-C and C-H) and carboxylic acid (C-COO) vibrations. Both SERS and SERS + HCPCF techniques presented here could aid the SBM project to characterize the fatty acid produced by their genetically modified organisms. The latter provides an *in situ* method that is easier to implement in practice. Furthermore, the SERS + HCPCF combination could also detect lipids other aqueous media such as blood, urine, or saliva. Future work includes utilizing more specialized SERS substrates to further

enhance the SERS signal and further study how the surface chemistry of the SERS substrate affects the interaction between fatty acid and the SERS substrate.

2.5. References

1. Rosenberger, S.; Evenblij, H.; Te Poele, S.; Wintgens, T.; Laabs, C. The Importance of Liquid Phase Analyses to Understand Fouling in Membrane Assisted Activated Sludge Processes—Six Case Studies of Different European Research Groups. *Journal of Membrane Science* **2005,** *263* (1-2), 113-126.
2. Meng, F.; Chae, S.-R.; Drews, A.; Kraume, M.; Shin, H.-S.; Yang, F. Recent Advances in Membrane Bioreactors (Mbrs): Membrane Fouling and Membrane Material. *Water research* **2009,** *43* (6), 1489-1512.
3. Agrawal, A.; Kale, R. Radiation Induced Peroxidative Damage: Mechanism and Significance. **2001**.
4. Ruffing, A. M. Improved Free Fatty Acid Production in Cyanobacteria with Synechococcus Sp. Pcc 7002 as Host. *Frontiers in bioengineering and biotechnology* **2014,** *2*, 17.
5. Margesin, R.; Schinner, F. Potential of Halotolerant and Halophilic Microorganisms for Biotechnology. *Extremophiles* **2001,** *5* (2), 73-83.
6. Lutchmiah, K.; Verliefde, A.; Roest, K.; Rietveld, L. C.; Cornelissen, E. R. Forward Osmosis for Application in Wastewater Treatment: A Review. *Water research* **2014,** *58*, 179-197.
7. Kamp, F.; Hamilton, J. A. Movement of Fatty Acids, Fatty Acid Analogs, and Bile Acids across Phospholipid Bilayers. *Biochemistry* **1993,** *32* (41), 11074-11085.
8. Miller, D. J.; Hawthorne, S. B. Solubility of Liquid Organics of Environmental Interest in Subcritical (Hot/Liquid) Water from 298 K to 473 K. *Journal of Chemical & Engineering Data* **2000,** *45* (1), 78-81.

9. Khuwijitjaru, P.; Adachi, S.; Matsuno, R. Solubility of Saturated Fatty Acids in Water at Elevated Temperatures. *Bioscience, biotechnology, and biochemistry* **2002,** *66* (8), 1723-1726.
10. Tomar, V. Raman Spectroscopy of Algae: A Review. *Journal of Nanomedicine & Nanotechnology* **2012,** *03* (02).
11. Wiberley, S. E.; Colthup, N.; Daly, L. Introduction to Infrared and Raman Spectroscopy. *ed. NB Colthup and LH Daly, Academic Press, Inc., San Diego* **1990**.
12. Beattie, J. R.; Bell, S. E.; Moss, B. W. A Critical Evaluation of Raman Spectroscopy for the Analysis of Lipids: Fatty Acid Methyl Esters. *Lipids* **2004,** *39* (5), 407-419.
13. De Gelder, J.; De Gussem, K.; Vandenabeele, P.; Moens, L. Reference Database of Raman Spectra of Biological Molecules. *J. Raman Spectrosc.* **2007,** *38* (9), 1133-1147.
14. Dong, W.; Zhang, Y.; Zhang, B.; Wang, X. Rapid Prediction of Fatty Acid Composition of Vegetable Oil by Raman Spectroscopy Coupled with Least Squares Support Vector Machines. *J. Raman Spectrosc.* **2013,** *44* (12), 1739-1745.
15. Weldon, M. K.; Zhelyaskov, V. R.; Morris, M. D. Surface-Enhanced Raman Spectroscopy of Lipids on Silver Microprobes. *Appl. Spectrosc.* **1998,** *52* (2), 265-269.
16. Wu, H.; Volponi, J. V.; Oliver, A. E.; Parikh, A. N.; Simmons, B. A.; Singh, S. In Vivo Lipidomics Using Single-Cell Raman Spectroscopy. *Proc. Natl. Acad. Sci. U.S.A.* **2011,** *108* (9), 3809-14.
17. Samek, O.; Jonáš, A.; Pilát, Z.; Zemánek, P.; Nedbal, L.; Tříska, J.; Kotas, P.; Trtílek, M. Raman Microspectroscopy of Individual Algal Cells: Sensing Unsaturation of Storage Lipids in Vivo. *Sensors* **2010,** *10* (9), 8635-8651.

18. Theophanides, T. *Infrared and Raman Spectroscopy of Biological Molecules: Proceedings of the Nato Advanced Study Institute Held at Athens, Greece, August 22–31, 1978*; Springer Science & Business Media: 2012; Vol. 43.
19. Tasumi, M.; Shimanouchi, T.; Miyazawa, T. Normal Vibrations and Force Constants of Polymethylene Chain. *Journal of Molecular Spectroscopy* **1962,** *9*, 261-287.
20. Spiker Jr, R. C.; Levin, I. W. Phase Transitions of Phospholipid Single-Wall Vesicles and Multilayers. Measurement by Vibrational Raman Spectroscopic Frequency Differences. *Biochimica et Biophysica Acta (BBA)-Biomembranes* **1976,** *433* (3), 457-468.
21. Ralston, A.; Hoerr, C. The Solubilities of the Normal Saturated Fatty Acids. *The Journal of Organic Chemistry* **1942,** *7* (6), 546-555.
22. Ralston, A.; Hoerr, C.; Pool, W.; Harwood, H. Solubilities of High Molecular Weight Normal Aliphatic Primary Amines. *The Journal of Organic Chemistry* **1944,** *9* (1), 102-112.
23. Hu, J.; Wang, Z.; Li, J. Gold Nanoparticles with Special Shapes: Controlled Synthesis, Surface-Enhanced Raman Scattering, and the Application in Biodetection. *Sensors* **2007,** *7* (12), 3299-3311.
24. Moskovits, M.; Suh, J. Conformation of Mono-and Dicarboxylic Acids Adsorbed on Silver Surfaces. *JACS* **1985,** *107* (24), 6826-6829.
25. Suh, J. Overtones of Longitudinal Acoustical Vibration of Palmitic Acid Adsorbed on Silver. *Chemical physics letters* **1992,** *193* (5), 327-330.
26. Konorov, S. O.; Addison, C. J.; Schulze, H. G.; Turner, R. F.; Blades, M. W. Hollow-Core Photonic Crystal Fiber-Optic Probes for Raman Spectroscopy. *Opt. Lett.* **2006,** *31* (12), 1911-1913.
27. Frosch, T.; Yan, D.; Popp, J. Ultrasensitive Fiber Enhanced Uv Resonance Raman Sensing of Drugs. *Anal Chem* **2013,** *85* (13), 6264-71.

28. Yan, D.; Popp, J.; Frosch, T. Analysis of Fiber-Enhanced Raman Gas Sensing Based on Raman Chemical Imaging. *Analytical chemistry* **2017,** *89* (22), 12269-12275.
29. Zhang, Y.; Shi, C.; Gu, C.; Seballos, L.; Zhang, J. Z. Liquid Core Photonic Crystal Fiber Sensor Based on Surface Enhanced Raman Scattering. *Applied Physics Letters* **2007,** *90* (19), 193504.
30. Roberts, P.; Couny, F.; Sabert, H.; Mangan, B.; Williams, D.; Farr, L.; Mason, M.; Tomlinson, A.; Birks, T.; Knight, J. Ultimate Low Loss of Hollow-Core Photonic Crystal Fibres. *Optics Express* **2005,** *13* (1), 236-244.
31. Pristinski, D.; Du, H. Solid-Core Photonic Crystal Fiber as a Raman Spectroscopy Platform with a Silica Core as an Internal Reference. *Optics letters* **2006,** *31* (22), 3246-3248.
32. Gong, T.; Cui, Y.; Goh, D.; Voon, K. K.; Shum, P. P.; Humbert, G.; Auguste, J. L.; Dinh, X. Q.; Yong, K. T.; Olivo, M. Highly Sensitive Sers Detection and Quantification of Sialic Acid on Single Cell Using Photonic-Crystal Fiber with Gold Nanoparticles. *Biosens Bioelectron* **2015,** *64*, 227-33.
33. Aust, J. F.; Booksh, K. S.; Myrick, M. L. Novel in Situ Probe for Monitoring Polymer Curing. *Applied spectroscopy* **1996,** *50* (3), 382-387.
34. Yang, X.; Shi, C.; Wheeler, D.; Newhouse, R.; Chen, B.; Zhang, J. Z.; Gu, C. High-Sensitivity Molecular Sensing Using Hollow-Core Photonic Crystal Fiber and Surface-Enhanced Raman Scattering. *J Opt Soc Am A Opt Image Sci Vis* **2010,** *27* (5), 977-84.
35. Leopold, N.; Lendl, B. A New Method for Fast Preparation of Highly Surface-Enhanced Raman Scattering (Sers) Active Silver Colloids at Room Temperature by Reduction of Silver Nitrate with Hydroxylamine Hydrochloride. *J. Phys. Chem. B* **2003,** *107* (24), 5723-5727.
36. Lee, P.; Meisel, D. Adsorption and Surface-Enhanced Raman of Dyes on Silver and Gold Sols. *The Journal of Physical Chemistry* **1982,** *86* (17), 3391-3395.

CHAPTER 3

Hollow Gold Nanosphere Templated Synthesis of PEGylated Hollow Gold Nanostars and Use for SERS Detection of Amyloid Beta in Solution

3.1. Abstract

Hollow gold nanospheres (HGNs) have been used as the template for seed-mediated growth of multibranched hollow gold nanostars (HNS). The HGNs were synthesized via anerobic reduction of cobalt chloride to cobalt nanoparticles then the formation of a gold shell via galvanic replacement followed by the oxidation of the cobalt core. Control of the inner core size of the HGNs was obtained by increasing the size of the sacrificial cobalt core, by varying the ratio of $B(OH)_3/BH_4$ using boric acid rather than 48-hour aged borohydride. The HNS were synthesized by reducing Au^{3+} ions in the presence of Ag^{+} ions using ascorbic acid, creating a spiky morphology that varied with the ratio of Au^{3+}/Ag^{+}. A broadly tunable localized surface plasmon resonance was achieved by controlling both the inner core and the spike length. Amyloid beta (Aβ) was conjugated to the HNS using a heterobifunctional PEG linker and identified by the vibrational modes associated with the conjugated ring phenylalanine side chain. A bicinchoninic acid assay was used to determine the concentration of Aβ conjugated to HNS as 20 nM, which is below the level of Aβ that negatively affects long-term potentiation. Both the core size and spike length were shown to affect the optical properties of the resulting nanostructures. This HGN templated method introduced a new parameter for enhancing the plasmonic properties of gold nanostars, namely the addition of a hollow core. Hollow gold nanostars are highly desirable for many applications, including high sensitivity disease detection and monitoring.

3.2. Introduction

One in nine people age 65 and older experiences the life-altering cognitive impairment from Alzheimer's dementia.[1] However, little can be done to alleviate symptoms unless the disease is diagnosed in its early stages.[1, 2] Amyloid beta$_{1-42}$ (Aβ42) modulates synaptic activity in the hippocampal neuronal networks, but its effect varies based on concentration.[3-5] At picomolar concentrations, there is a positive effect on synaptic plasticity and memory; however, between 50 – 500 nanomolar, Aβ42 reduces the synaptic activity leading to lowered long term potentiation.[6, 7] Furthermore, neurotoxic levels of Aβ42 that lead to dementia have been found at micromolar concentrations.[8]

The most common approaches for detecting amyloid beta in cerebrospinal fluid are based on classical enzyme-linked immunosorbent assay (ELISA), modified ELISA, electrochemical and chemiluminescent assay, mass spectroscopy, and surface enhanced Raman scattering (SERS) based assay.[9-11] A SERS based immunoassay is advantageous due to its demonstrated speed, simplicity, and molecular specificity.[12-15] Overwhelmingly SERS based studies of Aβ have struggled to achieve sensitive, label-free detection.[16, 17] Improving SERS based assays could be done by extending the high sensitivity of Raman scattering to near-IR excitation sources through the use of near-IR absorbing SERS substrates and specific binding via bioconjugation. The successful detection of Aβ could lead to noninvasive spectroscopic techniques that could aid *in situ* early detection and active monitoring of the production of amyloid beta and other tau proteins.

3.2.1 Limitation of Previous SERS Based Detection of Amyloid Beta Protein

SERS has been successful with the use of plasmonic particles and combines the molecular specificity and easy sample preparation of Raman spectroscopy while helping to overcome its limited sensitivity. In 2017, Solís *et al.* analyzed widely used SERS substrate morphologies, namely spheres, rods, and stars.[18] They concluded that nanoparticles with higher anisotropy such as gold nanostars outperform nanospheres and rods at longer wavelengths needed for near-IR sensing. Additionally, nanostars achieve a significantly higher enhancement without aggregation.[19-21] Since the introduction of gold nanostars in 2006, much work has been done to elucidate the relationships between gold ions, silver ions, reducing agents, surfactants, and pH and their influence on the length, density, and morphology of their spicules.[22-30] Additionally, both seed-mediated and seedless gold nanostar synthetic techniques have been successfully developed. However, there have not been any studies with hollow gold nanospheres (HGNs) as a seed. Therefore, there are no studies on how a hollow core affects the localized plasmon resonance and electromagnetic field enhancement. It is thus of interest to add another dimension of control to the gold nanostar syntheses using HGNs as seed particles to demonstrate a high yield synthesis of hollow gold nanostars (HNS).

In this chapter, we have synthesized highly nanostructured particles with sharp edges for enhancing the electromagnetic field around a target analyte to create a better SERS substrate. This was done by a seed-mediated method using HGN as the template to synthesize HNS. The void-space core diameter was controlled through

tuning size of the sacrificial cobalt template by optimizing the concentration of borohydride reducing agent with commercially available boric acid. Boric acid expedites the hydrolysis of borohydride to borate which reduces the reductive capability enabling the synthesis of larger cobalt scaffold particles. Rhodamine 6G was then used to determine the analytical enhancement factors of the HNS. Furthermore, the HNS were conjugated to $A\beta_{1-14}$, a mouse-derived, non-aggregating segment of Aβ42, using a heterobifunctional PEG linker. Ultimately, direct, label-free detection of $A\beta_{1-14}$ was achieved at low molar concentrations utilizing HNS with tunable plasmonic properties gained via highly modular synthetic techniques. Figure 3.1 shows a summary of the work in this chapter.

Figure 3.1 illustrates an overview of the results of this chapter. The SERS analysis of amyloid beta was preceded by the HGN seed templated synthesis of hollow gold nanostars and PEGylation.

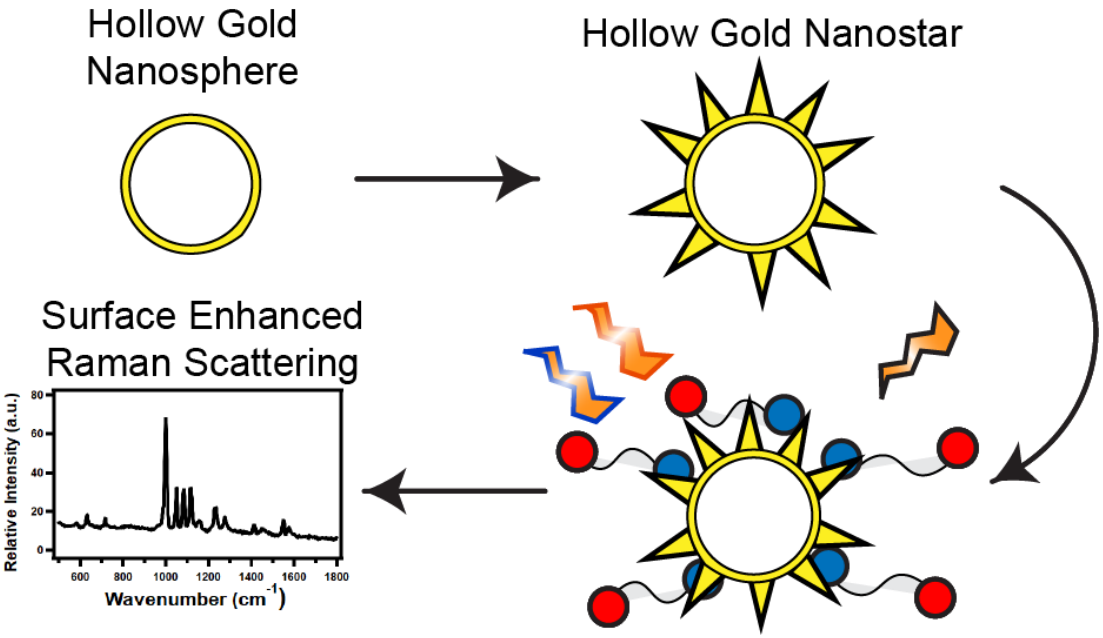

Figure 3.1. Overview of the experiments performed in this chapter. Hollow gold nanospheres were used a template to synthesize hollo gold nanostars. The hollow gold nanostars were conjugated to amyloid beta via a heterobifunctional PEG linker then analyzed using Raman spectroscopy.

3.3. Results and Discussion

Multi-branched HNS were synthesized in four steps as shown in Figure 3.2A: (1) the deaeration of a solution containing cobalt chloride and trisodium citrate using a Schlenk line apparatus; (2) the reduction of Co^{2+} ions to Co^{0} nanoparticles using a 1:3 mixture of 1.0 M sodium borohydride and 1.0 M boric acid; (3) the anaerobic galvanic exchange of Au^{3+} with Co^{0} to form a gold layer followed by exposure to atmosphere; and (4) the reduction of Au^{3+} ions onto the HGN template in the presences of Ag^{+} using ascorbic acid.[31, 32] The synthesis of an HGN template followed well-established protocols where the interior core size was tuned via fine control of the borohydride ion concentration.[32-35] In this chapter, boric acid was used to eliminate the need to hydrolyze borohydride for 48 hours. The reaction of

borohydride with boric acid is seen in Equation 1.[36] Ultimately, the borohydride and boric acid formed a sodium tetraborate hydrate.

$$2\,NaBH_4 + 2H_3BO_3 + H_2O \rightarrow Na_2BO_7\,XH_2O + 8H_2 \qquad \text{Equation 1}$$

The surface morphology of HGNs was made urchin-like by the addition of gold salt following the work by the Dinh group.[26] In the present work, we found a range where gold salt achieved different shapes, as seen in Figure 3.2B. The crystal structure of the seed HGN particles was verified using lattice spacing from HRTEM images and was found to be identical to solid colloidal gold this deposition of silver and gold follows published work. The HNS with the highest length and density of

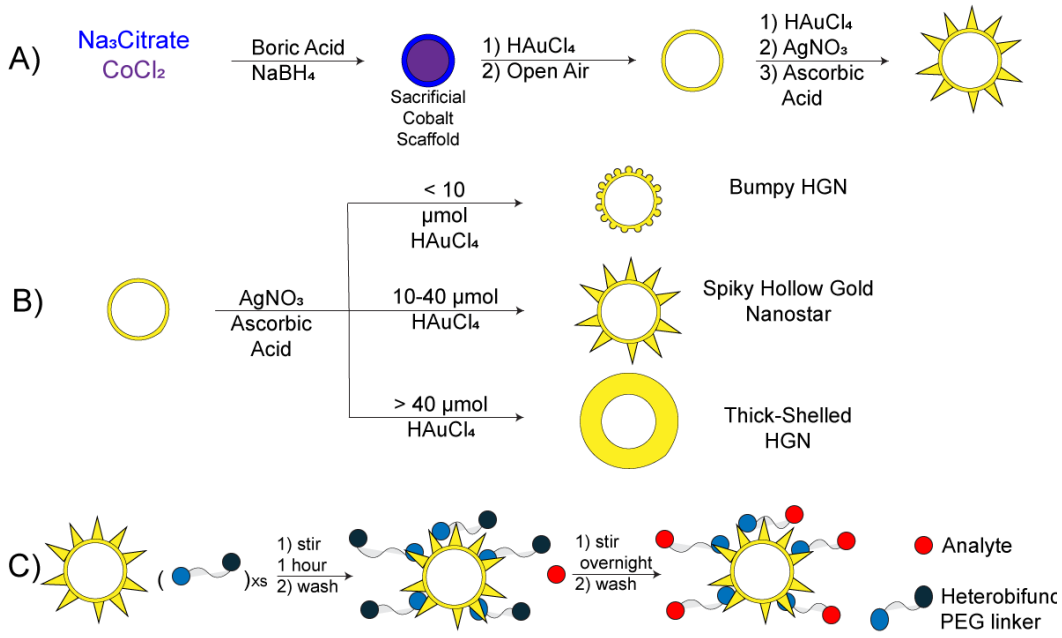

Figure 3.2. HGN seed templated synthesis of each SERS substrate. Control of the surface morphology of the SERS substrate was achieved by controlling the ratio of Au^{3+}/Ag^{+}.

spikes were selected for SERS measurements. As illustrated in Figure 3.2C, the HNS are conjugated to a heterobifunctional PEG linker then to $A\beta_{1-14}$ and characterized using SERS.

The values from Table 3.1. Were used to generate Figure 3.2B. The ratio of gold ions to silver ions increased nonlinearly with a sharp increase between 15 to 40 to hollow smooth gold nanoparticle.

Table 3.1. The amount of silver and gold in the HGN seed and each HGNS as measured by ICP-OES.

	Au (ppm)	σ	Ag (ppm)	σ	Au/Ag	σ
HGN seed	1.02	0.27	NA	NA	NA	NA
Bumpy HGN	0.99	0.15	0.37	0.02	2.67	0.43
HGNS 1	2.68	0.22	0.82	0.04	3.27	0.31
HGNS 2	2.60	0.06	0.63	0.02	4.10	0.16
Thick Shelled HGN 1	15.97	0.68	1.05	0.03	15.17	0.78
Thick Shelled HGN 1	13.32	0.84	0.62	0.02	21.42	1.52

a)

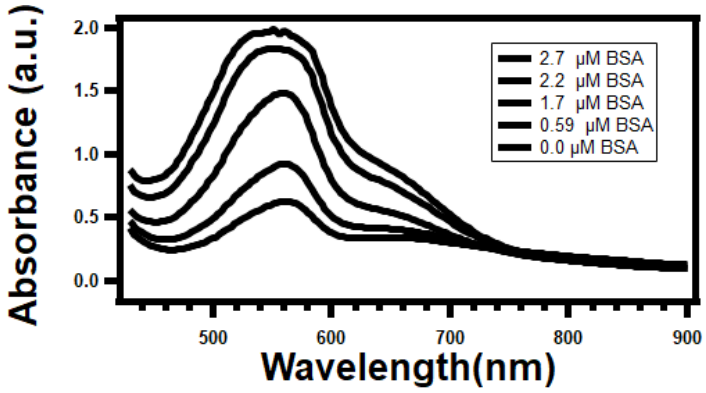

b)

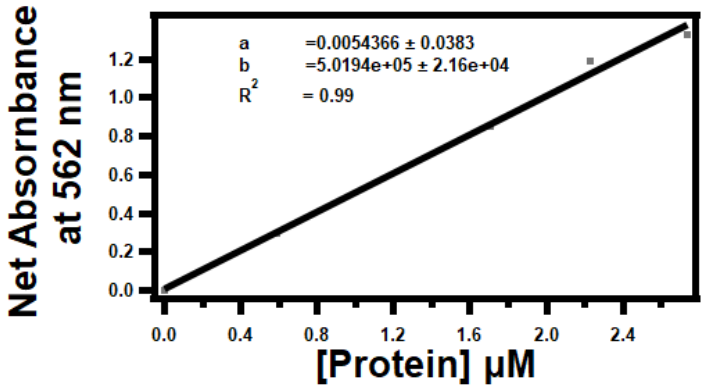

c)

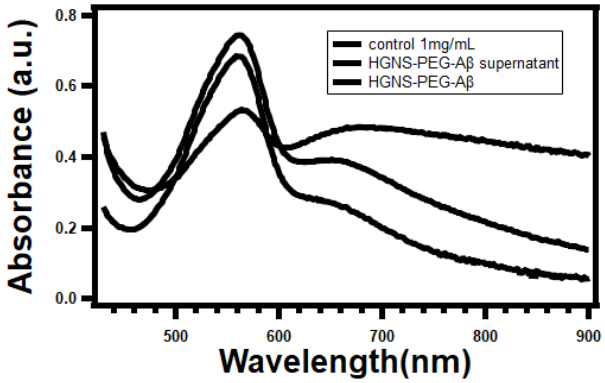

Figure 3.3. Results of the Bicinchoninic acid whereas a) and b) are the UV Vis spectra and calibration curve of the BSA standard dilution series and c) is the UV Vis spectra of a known amount of Aβ and the nanostars-PEG-Aβ complex.

Table 3.2. The amount of protein as calculated by Bicinchoninic acid assay for BSA control and the nanostar-PEG-Aβ complex.

	Standard Concentration	Net A 562 nm	[Aβ] μM
Control	10 μg/mL	0.12	0.23
HGNS-PEG-Aβ supernantant	unknown	0.10	0.18
HGNS-PEG-Aβ	unknown	0.02	0.02

3.3.1. Optical and Structural Properties

HNS synthesized from an HGN template show a red-shifted localized surface plasmon resonance (LSPR). During the HNS synthesis, Au^{3+} ions are reduced on the HGN seed using ascorbic acid in the presence of Ag^{+} ions. As shown in Figure 3.4A, the HGN seed had an LSPR peak at 550 nm. For ease of discussion, the nanostructures were named bumpy HGN (BHGN), HNS 2, HNS 1, thick-shelled HGN 1 (TSHGN 1), and thick-shelled HGN 2 (TSHGN 2) corresponding to the addition of 5, 10, 20, 40, and 60 μmol of Au^{3+} to the hollow nanostar growth solution. All other parameters such as Ag^{+} and ascorbic acid remained constant. The BHGN had a 100 nm red-shifted LSPR of 655 nm. Additionally, the spectral profile broadens due to the formation of polydisperse nodules. The formation of spikes as seen in HNS 1 further red-shifted the LSPR to 665 nm but a decrease in polydispersity occurred and the spectral width narrowed. The largest red-shift occurred for HNS 2 where the LSPR was 815 nm. This is attributed to longer spikes with a higher density. Upon the

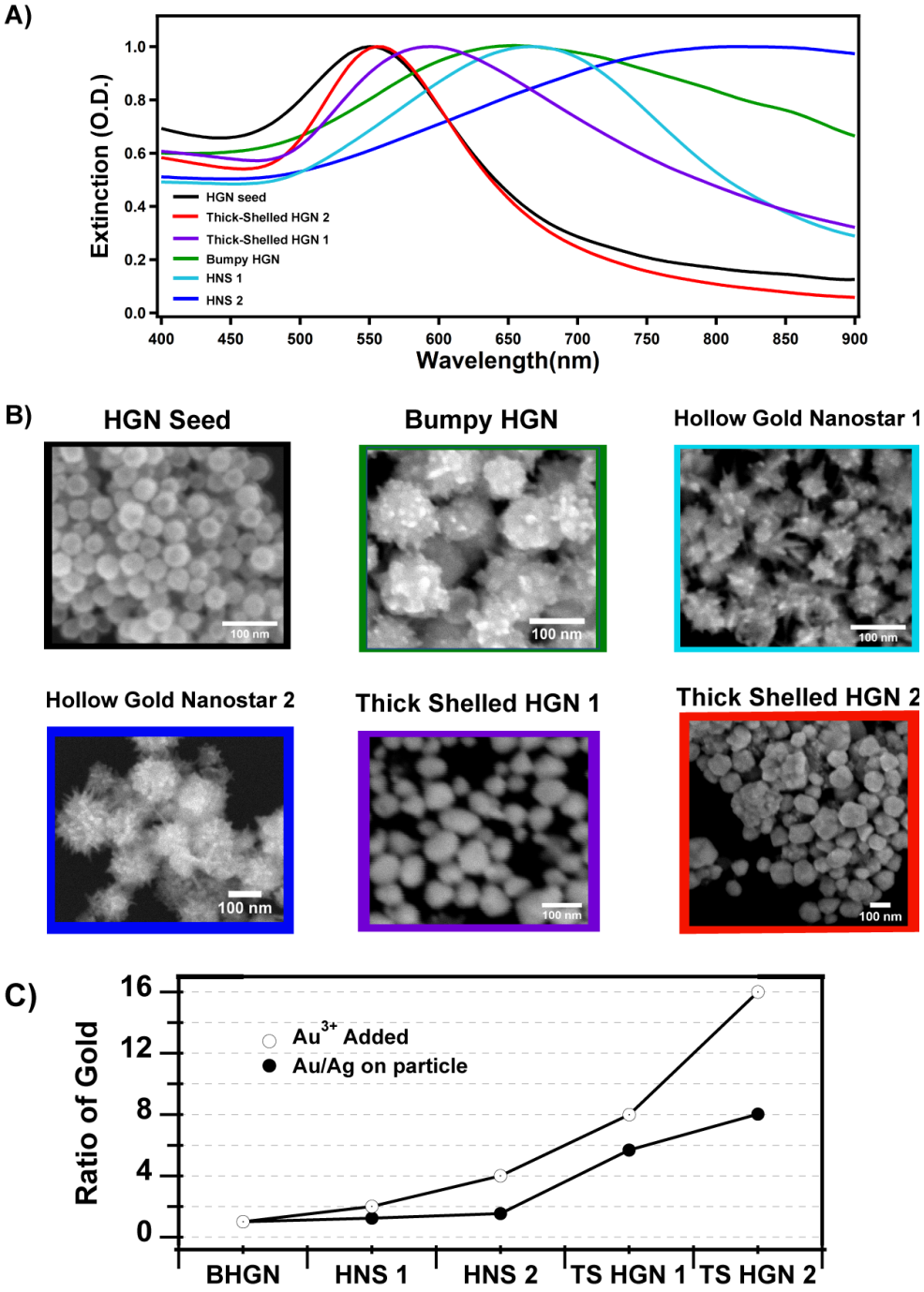

Figure 3.4. The optical and structural properties of the HGN seed, bumpy HGN, HGNS1, HGNS2, TSHGN1, and TSHGN2 where a) is the UV Vis spectra of each nanostructure normalized to 1.0 optical density, b) are the scanning electron microscope images of each nanostructure where the scale bar is 100 nm in each image, and c) is the ratio of gold to silver.

addition of 40 and 60 μmol of Au^{3+}, the LSPR blue-shifted with respect to the HNS to 595 and 555 nm respectively. Because the LSPR is still severely red-shifted as compared to similarly sized solid gold nanoparticles, the last two nanostructures are likely hollow and were name thick-shelled HGNs.

Another trend observed in the UV-vis spectra in Figure 3.4A is the LSPR band broadening associated with the growth of the spiky surface. HNS 2 has the largest full-width at half the maximum intensity along with the most NIR shifted SPR followed by bHGN then HNS 1. There are many factors that can contribute to the changes in optical properties such as longer spikes, polydispersity in tip to tip diameter, shifting core thickness. In previous work, Nehl *et al*. and Hao *et al*. combined the plasmon hybridization with numerical approaches to elucidate how the physical structure of complex nanostructures affects the LSPR.[24, 29, 30] The major finding was that the extinction spectrum of gold nanostars was composed of scattering and absorption from both the core and tips of the nanoparticle.[24, 29, 30] The major changes in SPR were likely associated with the largest change in nanostructure namely the formation of spikes that increase the size of the nanoparticles.

The SEM images in Figure 3.4B further explain the SPR shifts seen in UV-vis spectra. As nodules lengthen to spikes, the SPR red-shifts, and as the spikes reduce to a smooth surface, the SPR blue-shifts. The surface roughened from smooths HGNs into nodules upon the addition of 5.0 μmol Au^{3+}. The longest spikes formed with 10 and 20 μmol of Au^{3+} added (HNS 1 and HNS 2), but there was a higher density of

spikes for HNS 2. Close up images of HNS 1 and HNS 2 shown in Figure 3.5 to help to visualize their difference in structure. SEM confirmed that both TSHGN were smooth and much larger. TSHGN 1 and 2 were 64 ± 14 nm and 81 ± 18 nm. Because the extinction spectrum is red-shifted compared to analogous solid gold sols, suggesting that the hollow core remained present. [37]

Each type of nanostructures can further be explained by the ICP-OES results in Figure 2C showing the amounts of Au and Ag in each nanostructure. From BHGN to HNS 2, there was an increase of four times the amount of μmol of Au^{3+} added to the growth solution, but ICP-OES revealed only a 1.5 increase in the amount of gold from BHGN to HNS 2. This shows that silver blocks much of the gold from depositing onto the HGN template which promoted the growth of spikes. From HNS 2 to the TSHGNs the ratio of μmol of Au^{3+} added to the growth solution was 8 and 12 times the amount added to make BHGN. ICP-OES for TSHGN1 and 2 showed 5.7 and 8.0 times the amount of gold added onto the particle as compared to BHGN. ICP-OES and SEM images suggested that the gold atoms deposited over the previously blocked sites to form smooth nanoparticles. The specific ppm values of Au and Ag for each sample are given in Table 3.1.

Overall, the HGN seed provided a way to control the void space inner diameter of the HNS. Electron microscopy images of the void space can be seen in Figure 3.5. The spiky surface was formed by reducing added gold ions onto the existing nanoparticle surface an HGN seed particle in the presence of silver ions. The silver ions help to limit available binding sites of gold, resulting in directed growth of

gold nodules that quickly form spikes.[38] Lastly, ascorbic acid was used as a reducing agent to prevent the development of new gold or silver nanoparticles. The resulting HNS had sharp spikes with SPR tunable throughout the visible and near-IR spectrum.

Figure 3.5 shows the lattice spacing of a representative sample of HGN seed and bumpy HGN. The d spacing match gold based on the Winchell Elements of Optical Mineralogy database.

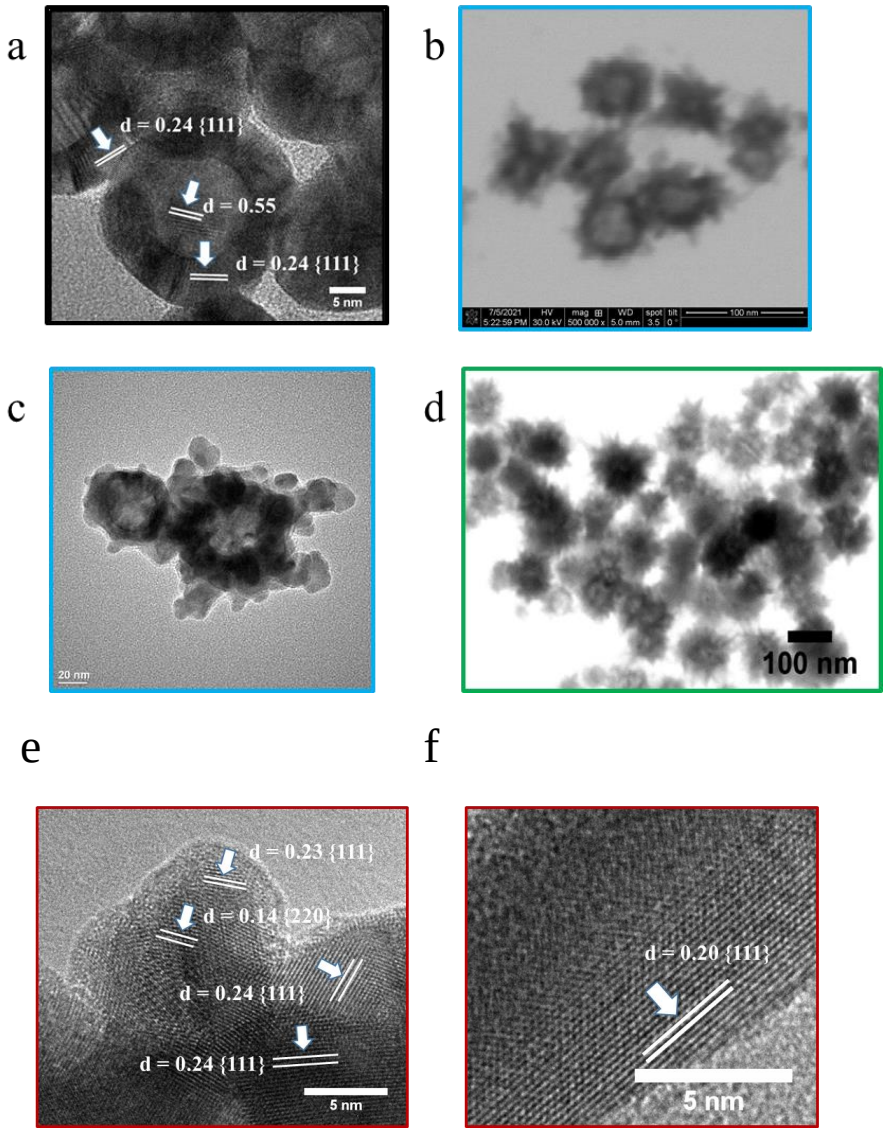

Figure 3.5. Transmission electron microscopy images of a) the HGN seed nanoparticle with lattice spacing measurements visible, b and c) low resolution image of image of HNS1 and high-resolution image of HNS1 next to an unreacted HGN seed nanoparticle, d) low resolution image of HNS 2, and e and f) lattice spacings of bHGN and HNS.

3.3.2. Raman and SERS Analysis of OPSSPEGSVA

Figure 3.6 shows the Raman spectra of crystalline OPSSPEGSVA, the calculated spectra of OPSSPEGSVA with varying length of repeat PEG units, and the

SERS spectra of the PEG linker with each nanostructure. Figure 3.6a shows the Raman spectra of a solid OPSSPEGSVA sample along with the calculated DFT Raman spectra of a monomer (OPSSPEG$_1$SVA), heptamer (OPSSPEG$_7$SVA), and pentedecamer (OPSSPEG$_{15}$SVA) linkers. There is good agreement between the observed and calculated PEG peaks. The results also agreed with previously published results on PEG.[46] A comprehensive list of the Raman and SERS peaks of OPSSPEGSVA along with the peak assignments is given in Table 3.2. A full list of peak positions and assignments of the calculated spectra are given in Table 3.3. The optimized structure of the calculated monomer, heptamer, and pentedecamer are given in Figures 3.8a-c.

The peaks associated with solid PEG have been well documented. Both Raman and SERS results of the solid OPSSPEGSVA and HNS-PEG are in agreement with each other and the previously published values for PEG. The peaks of interest are 990 cm^{-1} (C-C δ), 1047 cm^{-1} (CH_2), 1066 cm^{-1} (CH_2), 1128 cm^{-1} (CH_2), 1237 cm^{-1} (CH_2), 1284 cm^{-1} (CH_2), and 1400 cm^{-1} (CH_2), and 1487 cm^{-1} (CH_3). A complete list of the peaks is given in Tables 3.2 and S3. HNS-PEG differs from the solid PEG linker in that the 990 cm^{-1} peak shifted to 998 cm^{-1}, the 1284 cm^{-1} peak shifted to 1335 cm^{-1}, and lastly, the other peaks did not overlap with the dominant peaks from the dipeptide, TP. A

full comparison is given in Table 3.3.

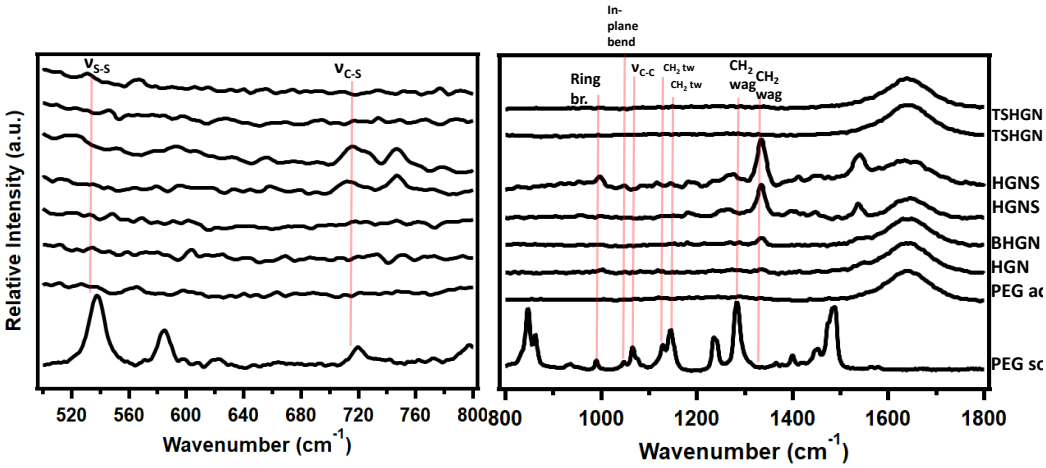

Figure 3.6. Observed Raman spectra of solid OPSSPEGSVA linker (5000k MW) and SERS spectra OPSSPEGSVA conjugated to each HGNS.

Figure 3.7 shows the optimized structures of the OPSSPEGSVA linker monomer, heptamer, pentedecamer, and pentedecamer conjugated to tyrosyl phenylalanine.

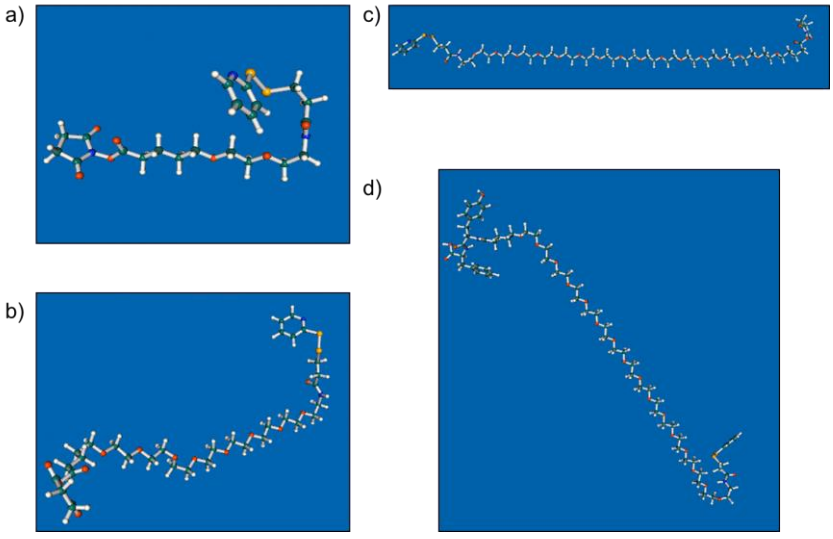

Figure 3.7. The DFT/B3LYP 6-31 (d,p) optimized structure of a) $OPSSPEG_1SVA$, b) $OPSSPEG_7SVA$ and c) $OPSSPEG_{15}SVA$, and d) Tyrosyl Phenylalanine - $OPSSPEG_{15}SVA$.

Table 3.3 shows the peak positions and assignments of solid and aqueous OPSSPEGSVA along with the peak assignments.

Table 3.3. Summary of the vibrational modes and peak assignments of OPSSPEGSVA as compared the results of a crystalline and the HGNS-OPSSPEGSVA conjugate.

ref 38		OPSSPEGSVA (s)	HNS-OPSSPEGSVA (l)	Assignment
cal	obs	obs	obs	
-	-	225	-	CH_2 ρ
-	-	281	-	CH_2 ρ
-	-	365	-	CH_2 ρ
-	-	430	-	-
-	-	538	-	SVA ring CH_2 ρ, CH_2 ρ
-	-	584	-	SVA ring CNC ν, CH_2 ρ
-	-	721	717	OPSS ring def
-	-		746	CH_2 ρ
845	844	847	-	CH2 , CO
890	863	862	-	CC, CO, CH_2
926	935	935	954	CC, CH_2
994	989	990	998	CC, CH_2
1048	1040	1047	-	CO, CH_2
1061	1061	1066	-	CO,CC
1128		1128	1116	CO,CH_2 ρ
1151	1145	1145	1171	CO
1235	1234	1237	-	CH_2 ω
1289	1280	1284	1276	CH_2 ω
1363	-	1364	1335	CH_2 ω
1399	1399	1399	1397	CH_2 ω
1451	-	1452	1446	CH_2 δ CH_3 δ
1488	1486	1484	1495	CH_3 δ
-	-	-	1538	-
-	-	1568	-	opss NCC def
-	-	1577	-	-
-	-	2836	-	CH_2 ν_{as} CH_2 ν_s
-	-	2889	-	CH_2 ν_{as} CH_2 ν_s
	-	2920	-	CH_2 ν_{as} CH_2 ν_s

* ν , δ , ρ, ω, τ, br, def represent stretching, scissoring, rocking, wagging, twisting, breathing, and deformation respectively. as – asymmetric and s – symmetric

Table 3.4 shows the peak positions and assignments of the calculated monomer, heptamer and pentedecamer spectra.

Table 3.4. Summary of the Raman spectra solid OPSSPEGSVA linker, $OPSSPEG_{15}SVA$, $OPSSPEG_7SVA$, and $OPSSPEG_1SVA$ with each peak assignment.

Calculated								
1mer	mode	Assignment	7mer	mode	Assignment	15mer	mode	Assignment
227	31	CH_2 ρ	239	56	CH_2 ρ	-	-	-
258	32	CH_2 ρ	281	59	CH_2 ρ	273	94	CH_2 ρ
359	38	CH_2 ρ	353	67	CH_2 ρ	-	-	-
430	43	CH_2 ρ, OH	420/442	73/74	CH_2 ρ, OH st	-	-	-
541	51	SVA ring CH_2 ρ, CH_2 ρ	543	85	SVA ring CH_2 ρ, CH_2 ρ	556	135	CH_2 ρ
584	52	SVA ring CNC st, CH_2 ρ	583	89	SVA ring CNC st, CH_2 ρ	586	138	SVA ring, CH_2 ρ
702	61	OPSS ring def	704	96	OPSS ring def	704	144	OPSS ring def
740	64	SVA ring breath	738	99	CH_2 ρ	780	150	CH_2 ρ
860	71	CH_2 , CO	845	112	CH_2 , CO	837	166	CH_2 ρ
871	72	OPSS ring wag	867	114	CC, CO, CH_2	865	169	CH_2 ρ
934	76	CH_2 ρ	-	-	-	-	-	-
997	84	CC SVA breath	984	127	CC CH_2 ρ	-	-	-
1050	90	CC SVA br CH_2 ρ	1053	141	CO SVA ring br CH_2 ρ	1030	203	OPSS ring br
1064	92	CN st, CH_2 ρ CH_2 τ	1067	145	CO CC	1067	211	CH_2 ρ ω
1129	102	CO CH_2 τ	1127	159	CO CH_2 ρ	1129	235	CH_2 ρ
-			1151	169	CH_2 τ	1156	257	CH_2 ρ
1232	113	CH_2 τ	1228	183	CH_2 τ	1233	278	CCH_2 τ
1279	121	CH_2 τ	1286	200	CH_2 τ	1284	302	CH_2 τ ω
1355	127	CH2 ω	1367	213	CH_2 ω	1367	322	CH_2 ω
1406	132	CH_2 δ	1404	216	CH_2 ω	1406	330	CH_2 ω
1451	141	CH_2 δ	1453	230	CH_2 δ	1450	347	CH_2 δ ρ
1500	145	CO, OH wag, CH_2 τ, CH_2 δ	1489	242	CH_2 δ	1483	359	CH_2 δ ρ
1558	147	opss NCC def	1560	248	opss NCC st	1563	384	opss def
-			1568	249	opss CCC st	1571	385	opss def
-	-	-	-	-	-	-	-	-
2840	152	CH_2 ν_s	2836	254	CH_2 ν_{as} CH_2 ν_s	2848	390	CH_2 ν_s out phase
2887	157	CH_2 ν_{as} CH_2 ν_s	2877	267	CH_2 ν_{as} CH_2 ν_s	2884	411	CH_2 ν_s in phase
2919	160	CH_2 ν_s	2919	283	CH_2 ν_{as}	2918	439	CH_2 ν_{as} CH_2 ν_s

* ν , δ , ρ, ω, τ, br, def represent stretching, scissoring, rocking, wagging, twisting, breathing, and deformation respectively, as – asymmetric and s – symmetric

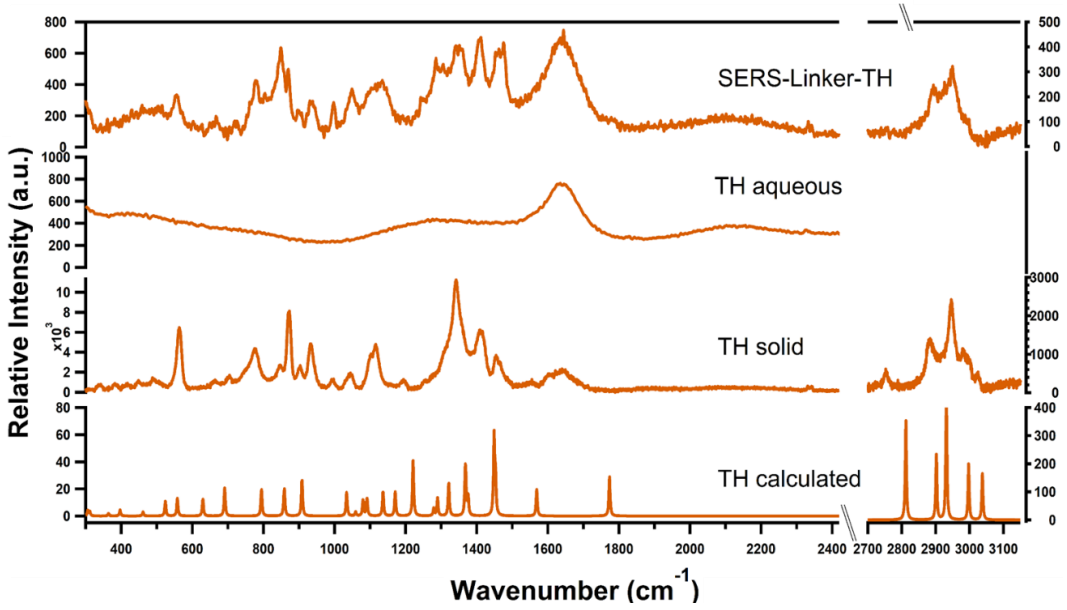

Figure 3.8. SERS and Raman spectra of threonine showing the HGNS-PEG-amino acid complex (top), threonine dissolved in water (1mg/mL), a Raman spectrum of solid threonine, and the calculated Raman spectra of threonine.

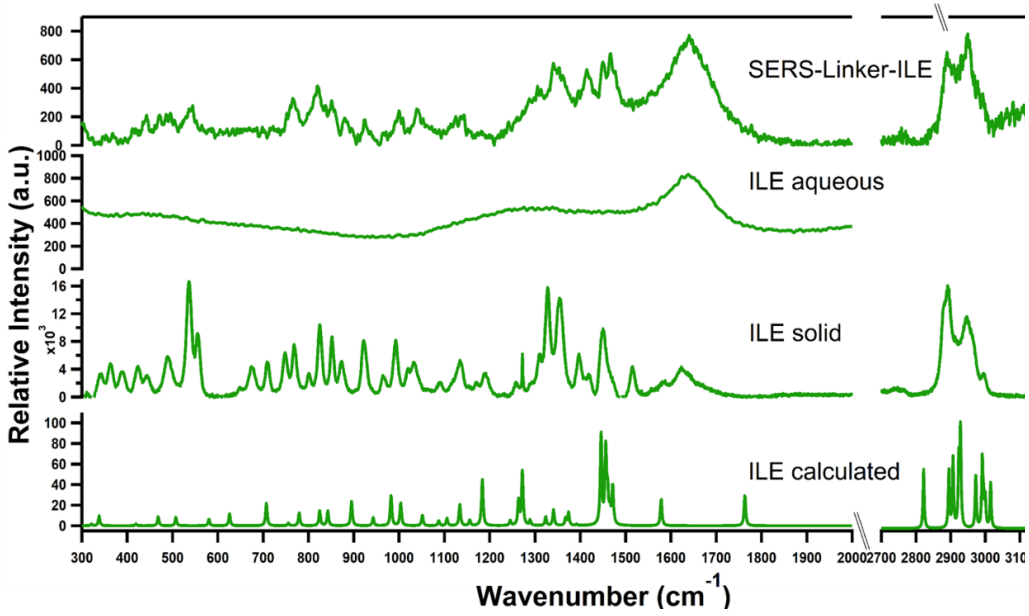

Figure 3.9. SERS and Raman spectra of isoleucine showing the HGNS-PEG-amino acid complex (top), isoleucine dissolved in water (1mg/mL), a Raman spectrum of solid isoleucine, and the calculated Raman spectra of isoleucine.

Table 3.5 shows the peak positions and assignments of the HNGS-PEG-TP/TH/ILE

complexes

Table 3.5. Summary of the Raman spectra of isoleucine (ILE), threonine (TH), and tyrosyl-phenylanine (TP), the SERS spectra of the HGNS-PEG-ILE, HGNS-PEG-TH, and HGNS-PEG-TP, and the calculated Raman spectra of ILE, TH, and TP with each peak assignment. Blue wavenumbers are contributions from the PEG linker.

ILE (s)	HNS-PEG-ILE (l)	ILE	Assignment	TH(s)	HNS-PEG-TH (l)	TH	Assignment	TP (s)	HNS-PEG-TP (l)	TP	Assignment
obs	obs	cal		obs	obs	cal		obs	obs	cal	
444	440	468		563	557	558	OH def	-	438	-	COH ω
537	539	580	NCO δ	777	783	795	NH_2 ω		483		
769	767	756	CH_2 CH_3 ρ	844	848	859	CC st, CH_3 τ, NH_2 τ		541		
825	820	825	NH_2 δ	872	871	-			621		
852	854	843	NH_2 δ	903	902	909	CC st, CH_3 ρ . NH_2 ρ	-	722	721	OPSS ring def
992	999	1004	CC st	934	937	-		1005	1003	1015	Phe ring def, CH_2 ρ
1031	1045	1052	CH_2 CH3 ρ	993	998	-	A CH_2 ρ CH_2 τ CH_2 δ ρ CH_2 ω	1043	1051	1066	Tyr ring def, CH_2 ρ , αCC ν
1309	1309	1320	CH_2 ω CH_3 ρ	1043	1046	1034	CC ν, CH_3 ρ. NH_2 ρ	1081	1085	-	
1355	1341	1341	CH_2 ω, CC st	1112	1122	1137	CH def, CO ν, OH def	1118	1122	1114	αCN ν, NH_2 δ
1418	1412	1446	CH_2 sc CH_3 ρ	1254	1246	-		1163	1159	1155	Tyr ring def, OH def
1450	1449	1457	CH_3 δ τ	1276	1291	1290	CH def, NH_2 τ, OH def, CH_3 δ	1247	1233	1242	CH def, CH_2 τ, NH_2 τ
1463	1466	1471	CH_3 δ	1343	1350	-		1279	1276	1287	PHE ring def
2878	-	2895	CH ν_s	1412	1409	-		1344	1368	1332	COO- st, CH_2 τ
2893	2893	2907	CH_2 ν_s	1455	1464	1450	CH_3 δ	1406	1415	1431	Tyr ring def, CH_2 τ
2946	2945	2927	CH_3 ν_s	2753	2898	2812	αCC ν	1447	1453	1441	CH_2 δ, PHE ring def
2965	-	2972	CH_2 CH_2 ν_{as}	2886	2926	2902	CH st	-	1554	-	
2996	2990	2993	CH_2 CH_2 ν_{as}	2945	2951	2932	CH_3 ν_s	1585	1579	1580	Tyr ring def, CH_2 τ , NH_2 δ
				2989	2989	2997	CH_3 ν_{as}	2934	-	2923	CH_2 ν_s
				3049	-	3038	CH_3 ν_{as}	2968	-	2968	CH_3 ν_{as} , CH ν
								3014	-	3014	CH_2 ν_{as}
								3047	-	3042	Tyr ring CH ν
								3066	-	3067	Phe ring CH ν

* ν , δ , ρ, ω, τ, br, def represent stretching, scissoring, rocking, wagging, twisting, breathing, and deformation respectively, as – asymmetric and s – symmetric

3.3.3. Comparative Analysis of $A\beta_{1-14}$ Raman and SERS

Proteins are often difficult to directly detect Raman spectroscopy due to low cross section and complex three-dimensional structures that vary among proteins. To increase the Raman signal, we covalently linked $A\beta_{1-14}$ to the SERS substrate using a PEG linker. The PEG linker contained two moieties that easily undergo a substitution reaction: the orthopyridyl disulfide moiety formed a gold-thiol bond with the HNS and the succinimidyl ester reacts with the N-terminus of $A\beta_{1-14}$ to form a new amide bond. The result is that $A\beta_{1-14}$ is closer to the surface of the HNS. All the SERS measurements were performed in aqueous solutions to minimize variations in the SERS intensities that occur upon drying.[41, 42] $A\beta_{1-14}$ was detected using HNS 2 that showed the highest enhancement in earlier studies. Figure 3.11 shows the Raman and SERS spectra of $A\beta_{1-14}$ along with the SERS spectra of tyrosine-phenylanine (Tyr-Phe), isoleucine, and threonine conjugated to HNS 2 using the same procedure. Lastly, Figure 3.11 shows the Raman spectrum of solid OPSSPEGSVA and the SERS spectra of HNS 2 conjugated to only the PEG linker.

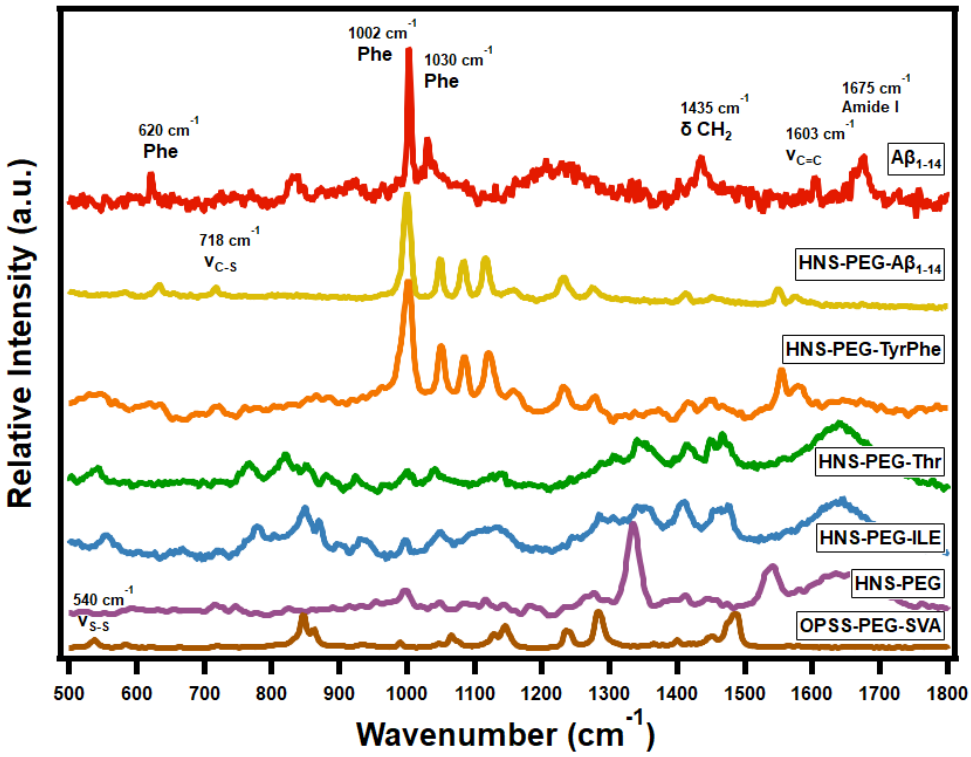

Figure 3.10. The Raman spectra of Aβ and OPSSPEGSVA for comparison to the SERS spectra of HNS-PEG and HNS-PEG conjugated to Aβ, Tyrosyl phenylalanine, threonine, and isoleucine.

$A\beta_{1-14}$ contained only one aromatic side chain, phenylalanine. The vibrations associated with the conjugated ring dominated both the Raman spectra of solid $A\beta_{1-14}$ and the SERS spectra of the HNS-PEG- $A\beta_{1-14}$ conjugate. The vibrational modes involving the benzene ring were 620 cm^{-1}, 1002 cm^{-1}, 1030 cm^{-1}, 1603 cm^{-1}.[12, 17, 43-47] There are several differences between the Raman spectra of $A\beta_{1-14}$ and the SERS spectra of SERS spectra of HNS-PEG- $A\beta_{1-14}$. The intensity of the amide I stretch of solid $A\beta_{1-14}$ was greatly diminished in the SERS spectra, and the C-CH_2 stretch at 1054 cm^{-1}, C-N stretch at 1156 cm^{-1}, and the amide III region at 1233 cm^{-1} appeared or increased in intensity. Lastly, the appearance of the C-S stretch at 718 cm^{-1}.

Analysis of the solid PEG linker and HNS conjugated solely to PEG further evinced the successful conjugation of HNS to PEG. The dominant peaks and assignments from solid PEG and HNS-PEG were 990 cm^{-1} (C-C), 1047 cm^{-1} (CH_2), 1066 cm^{-1} (CH_2), 1128 cm^{-1} (CH_2), 1237 cm^{-1} (CH_2), and 1284 cm^{-1} (CH_2). Both the Raman spectra from solid OPSSPEGSVA and the SERS spectra from HNS-PEG conjugate matched the well documented peaks associated with poly ethylene glycol, orthopyridyl disulfide and succinimydal valeric acid.[48] The appearance of the C-S stretch at 718 cm^{-1} appeared due to cleaving the orthopyridyl disulfide group.[49, 50] The disappearance of the S-S stretch at 540 cm^{-1} and the simultaneous increase in intensity of the C-S stretch at 718 cm^{-1} support the conclusion that PEG conjugated to gold. A complete list of the peaks is given in Tables 3.3 and 3.4.

Two amino acids and a dipeptide were studied to help understand the differences between the Raman spectra of solid $A\beta_{1-14}$ and the SERS spectra of the HNS-PEG- $A\beta_{1-14}$ conjugate. The amino acids selected contained side groups that resembled the PEG backbone, and the Tyr-Phe dipeptide selected contained the same aromatic side group found in $A\beta_{1-14}$. The SERS spectra of the HNS-PEG- amino acid conjugates were entirely dominated by CH_2, and CH_3 deformation modes that largely did not share any peaks assignments from solid $A\beta_{1-14}$ and were also shifted slightly from solid PEG and HNS-PEG. Conversely, the SERS spectra of the HNS-PEG-TyrPhe complex shared every major peak position and intensity with the HNS-PEG-$A\beta_{1-14}$ complex.

The full results given in Tables 3.4, 3.5, and 3.6. The dominant peaks found in HGNSPEGTP were 438 cm^{-1} (C-O-H ω), 1003 cm^{-1} (Phe ring deformation), 1051 cm^{-1} (CH_2 ρ), 1085 cm^{-1} (CC δ), 1122 cm^{-1} (CN δ, NH_2 δ), 1232 cm^{-1} (CH_2 ρ, CH_2τ), and 1277 cm^{-1} (CH_2 ρ, Phe ring deformation). The two bands at 1003 and 1277 cm^{-1} were similar in peak position and intensity to the phenylalanine ring deformation and CH_2 rocking modes found in both the observed and calculated TP spectra. The band at 1085 cm^{-1} experienced a large enhancement compared to the simulated spectra. Since HNS-PEG-TyrPhe contains two conjugated ring systems which are widely known to experience a strong SERS enhancement, the authors can confidently state that we directly detect $A\beta_{1-14}$ at a concentration of 20 nM as determined by BCA assay.

3.4. Conclusion

In summary, we have developed a new SERS substrate capable of detecting mouse derived $A\beta_{1-14}$ via OPSSPEGSVA which covalently linked both the hollow gold nanostars and $A\beta_{1-14}$ Through a BCA assay, it was determined that 20 nM of $A\beta_{1-14}$ was captured and detected via SERS performed in a colloidal solution. The success of the SERS measurements flourished from a seed-mediated method to synthesize HNS with a controllable interior core utilizing tunable HGNs. Boric acid eliminated the need to age the borohydride, reducing synthesis time by two days while retaining tunability. HNS were shown to also have a tunable LSPR by varying the one parameter. The amount of Au^{3+} ions added controlled the LSPR position and width.

Furthermore, the AEF of the HNS was determined to be 4.5 x 10^7 for the C-H out of plane bending vibration at 777 cm^{-1} peak in R6G. While the HGN seed particle demonstrated an AEF of 6.2 x 10^5 for the C-C-C ring in-plane bending vibration at 614 cm^{-1}. DFT calculated Raman spectra were used to distinguish OPSSPEGSVA peaks from analyte peaks. SERS spectra of the HGNS-PEG linker and HGNS-PEG-TP were analyzed using %PED to distinguish peaks from the PEG linker and the dipeptide analyte. The major finding is that tyrosylphenylalanine was directly detected despite overlaps in peak positions. Thus, a HNS-PEG linker-peptide conjugate could be used for direct detection of more structurally complex molecules in solution. This is exemplified by covalent bonding and detection of $A\beta_{1-14}$ in solution. The SERS intensity of the aromatic ring of the Phe residue in the HNS-PEG-$A\beta_{1-14}$ conjugate was greatly enhanced and was confirmed using a simpler Tyr-Phe dipeptide. The system may be useful for direct detection of full-length Aβ and other bioactive peptides with nanomolar sensitivity.

3.5 References

1. Blennow, K.; Zetterberg, H., Biomarkers for Alzheimer's disease: current status and prospects for the future. *J. Intern. Med.* **2018,** *284* (6), 643-663.
2. Harper, L. C., 2020 Alzheimer's Association Facts and Figures.
3. Cooke, S. F.; Bliss, T. V., Plasticity in the human central nervous system. *Brain* **2006,** *129* (7), 1659-1673.

4. Puzzo, D.; Privitera, L.; Leznik, E.; Fa, M.; Staniszewski, A.; Palmeri, A.; Arancio, O., Picomolar amyloid-β positively modulates synaptic plasticity and memory in hippocampus. *J. Neurosci.* **2008,** *28* (53), 14537-14545.
5. Hwang, S. S.; Chan, H.; Sorci, M.; Van Deventer, J.; Wittrup, D.; Belfort, G.; Walt, D., Detection of amyloid β oligomers toward early diagnosis of Alzheimer's disease. *Anal. Biochem.* **2019,** *566*, 40-45.
6. Abramov, E.; Dolev, I.; Fogel, H.; Ciccotosto, G. D.; Ruff, E.; Slutsky, I., Amyloid-β as a positive endogenous regulator of release probability at hippocampal synapses. *Nat. Neurosci.* **2009,** *12* (12), 1567-1576.
7. Raskatov, J. A., What is the "Relevant" Amyloid β 42 Concentration? *Chembiochem* **2019,** *20* (13), 1725.
8. Ono, K.; Condron, M. M.; Teplow, D. B., Structure–neurotoxicity relationships of amyloid β-protein oligomers. *Proc. Natl. Acad. Sci.* **2009,** *106* (35), 14745-14750.
9. Palmqvist, S.; Mattsson, N.; Hansson, O.; Initiative, A. s. D. N., Cerebrospinal fluid analysis detects cerebral amyloid-β accumulation earlier than positron emission tomography. *Brain* **2016,** *139* (4), 1226-1236.
10. Diba, F. S.; Kim, S.; Lee, H. J., Electrochemical immunoassay for amyloid-beta 1–42 peptide in biological fluids interfacing with a gold nanoparticle modified carbon surface. *Catal. Today* **2017,** *295*, 41-47.
11. Veerabhadrappa, B.; Delaby, C.; Hirtz, C.; Vialaret, J.; Alcolea, D.; Lleó, A.; Fortea, J.; Santosh, M. S.; Choubey, S.; Lehmann, S., Detection of amyloid beta peptides in body fluids for the diagnosis of alzheimer's disease: Where do we stand? *Crit. Rev. Clin. Lab. Sci.* **2020,** *57* (2), 99-113.
12. Wang, J.; Lin, D.; Lin, J.; Yu, Y.; Huang, Z.; Chen, Y.; Lin, J.; Feng, S.; Li, B.; Liu, N., Label-free detection of serum proteins using surface-enhanced Raman spectroscopy for colorectal cancer screening. *J. Biomed. Opt.* **2014,** *19* (8), 087003.

13. Zhao, J.; Wu, C.; Zhai, L.; Shi, X.; Li, X.; Weng, G.; Zhu, J.; Li, J.; Zhao, J.-W., A SERS-based immunoassay for the detection of α-fetoprotein using AuNS@Ag@SiO2core–shell nanostars. *J. Mater. Chem. C* **2019,** *7* (27), 8432-8441.
14. Nguyen, A. H.; Peters, E. A.; Schultz, Z. D., Bioanalytical applications of surface-enhanced Raman spectroscopy: de novo molecular identification. *Rev. Anal. Chem.* **2017,** *36* (4).
15. Li, D.; Wang, Y. In Na*noplasmonics Fundamentals and Application*;. Barbillon, G., Ed.; InTech: Croatia, **2017**; pp 341-352.
16. Altuntas, S.; Buyukserin, F., Fabrication of thioflavin-T-modified nanopillared SERS substrates for ultrasensitive beta-amyloid peptide detection. *J. Raman Spectrosc.* **2018,** *49* (8), 1247-1256.
17. Guerrini, L.; Arenal, R.; Mannini, B.; Chiti, F.; Pini, R.; Matteini, P.; Alvarez-Puebla, R. A., SERS detection of amyloid oligomers on metallorganic-decorated plasmonic beads. *ACS Appl. Mater. Interfaces* **2015,** *7* (18), 9420-9428.
18. Solís, D. M.; Taboada, J. M.; Obelleiro, F.; Liz-Marzán, L. M.; García de Abajo, F. J., Optimization of nanoparticle-based SERS substrates through large-scale realistic simulations. *ACS photonics* **2017,** *4* (2), 329-337.
19. Sánchez-Iglesias, A.; Barroso, J.; Solís, D. M.; Taboada, J. M.; Obelleiro, F.; Pavlov, V.; Chuvilin, A.; Grzelczak, M., Plasmonic substrates comprising gold nanostars efficiently regenerate cofactor molecules. *J. Mater. Chem. A* **2016,** *4* (18), 7045-7052.
20. Solis, D. M.; Taboada, J. M.; Obelleiro, F.; Liz-Marzan, L. M.; García de Abajo, F. J., Toward ultimate nanoplasmonics modeling. *Acs Nano* **2014,** *8* (8), 7559-7570.
21. Zhu, J.; Gao, J.; Li, J.-J.; Zhao, J.-W., Improve the surface-enhanced Raman scattering from rhodamine 6G adsorbed gold nanostars with vimineous branches. *Appl. Surf. Sci.* **2014,** *322*, 136-142.

22. Atta, S.; Beetz, M.; Fabris, L., Understanding the role of AgNO3 concentration and seed morphology in the achievement of tunable shape control in gold nanostars. *Nanoscale* **2019,** *11* (6), 2946-2958.
23. Zhu, J.; Liu, M.-J.; Li, J.-J.; Zhao, J.-W., Synthesis of gold nanostars with fractal structure: application in surface-enhanced Raman scattering. *Eur. Phys. J. B* **2017,** *90* (11).
24. Hao, F.; Nehl, C. L.; Hafner, J. H.; Nordlander, P., Plasmon resonances of a gold nanostar. *Nano Lett.* **2007,** *7* (3), 729-732.
25. Kumar, P. S.; Pastoriza-Santos, I.; Rodriguez-Gonzalez, B.; De Abajo, F. J. G.; Liz-Marzan, L. M., High-yield synthesis and optical response of gold nanostars. *Nanotechnology* **2007,** *19* (1), 015606.
26. Khoury, C. G.; Vo-Dinh, T., Gold nanostars for surface-enhanced Raman scattering: synthesis, characterization and optimization. *J. Phys. Chem C* **2008,** *112* (48), 18849-18859.
27. Barbosa, S.; Agrawal, A.; Pastoriza-Santos, I.; Rodríguez-Lorenzo, I.; Alvarez-Puebla, R.; Kornowski, A., Size tuning and sensing capabilities of gold nanostars. *Langmuir* **2010,** *26*, 14943-14950.
28. Sau, T. K.; Rogach, A. L.; Doblinger, M.; Feldmann, J., One-step high-yield aqueous synthesis of size-tunable multispiked gold nanoparticles. *Small* **2011,** *7* (15), 2188-94.
29. Nehl, C. L.; Liao, H.; Hafner, J. H., Optical properties of star-shaped gold nanoparticles. *Nano Lett.* **2006,** *6* (4), 683-688.
30. Nehl, C. L.; Hafner, J. H., Shape-dependent plasmon resonances of gold nanoparticles. *J. Mater. Chem.* **2008,** *18* (21), 2415-2419.
31. Adams, S.; Thai, D.; Mascona, X.; Schwartzberg, A. M.; Zhang, J. Z., Key factors affecting the reproducibility of synthesis and growth mechanism of near-infrared absorbing hollow gold nanospheres. *Chem. Mater.* **2014,** *26* (23), 6805-6810.

32. Lindley, S. A.; Cooper, J. K.; Rojas-Andrade, M. D.; Fung, V.; Leahy, C. J.; Chen, S.; Zhang, J. Z., Highly Tunable Hollow Gold Nanospheres: Gaining Size Control and Uniform Galvanic Exchange of Sacrificial Cobalt Boride Scaffolds. *ACS Appl. Mater. Interfaces* **2018,** *10* (15), 12992-13001.
33. Lindley, S. A.; Zhang, J. Z., Bumpy Hollow Gold Nanospheres for Theranostic Applications: Effect of Surface Morphology on Photothermal Conversion Efficiency. *ACS Appl. Nano Mater.* **2019,** *2* (2), 1072-1081.
34. Schwartzberg, A. M.; Olson, T. Y.; Talley, C. E.; Zhang, J. Z., Synthesis, characterization, and tunable optical properties of hollow gold nanospheres. *J. Phys. Chem B* **2006,** *110* (40), 19935-19944.
35. Olson, T. Y.; Schwartzberg, A. M.; Orme, C. A.; Talley, C. E.; O'Connell, B.; Zhang, J. Z., Hollow gold− silver double-shell nanospheres: structure, optical absorption, and surface-enhanced Raman scattering. *J. Phys. Chem C* **2008,** *112* (16), 6319-6329.
36. Balbay, A.; Şahin, Ö., Hydrogen production from sodium borohydride in boric acid-water mixtures. *Energy Sources* **2014,** *36* (11), 1166-1174.
37. Liu, X.; Atwater, M.; Wang, J.; Huo, Q., Extinction coefficient of gold nanoparticles with different sizes and different capping ligands. *Colloids Surf. B* **2007,** *58* (1), 3-7.
38. Yuan, H.; Khoury, C. G.; Hwang, H.; Wilson, C. M.; Grant, G. A.; Vo-Dinh, T., Gold nanostars: surfactant-free synthesis, 3D modelling, and two-photon photoluminescence imaging. *Nanotechnology* **2012,** *23* (7), 075102.
39. Le Ru, E.; Blackie, E.; Meyer, M.; Etchegoin, P. G., Surface enhanced Raman scattering enhancement factors: a comprehensive study. *J. Phys. Chem C* **2007,** *111* (37), 13794-13803.
40. He, X. N.; Gao, Y.; Mahjouri-Samani, M.; Black, P.; Allen, J.; Mitchell, M.; Xiong, W.; Zhou, Y.; Jiang, L.; Lu, Y., Surface-enhanced Raman spectroscopy using gold-coated horizontally aligned carbon nanotubes. *Nanotechnology* **2012,** *23* (20), 205702.

41. Fleger, Y.; Mastai, Y.; Rosenbluh, M.; Dressler, D., SERS as a probe for adsorbate orientation on silver nanoclusters. *J. Raman Spectrosc.* **2009,** *40* (11), 1572-1577.
42. Shaine, M.; Premasiri, W.; Ingraham, H.; Andino, R.; Lemler, P.; Brodeur, A.; Ziegler, L., Surface enhanced Raman scattering for robust, sensitive detection and confirmatory identification of dried bloodstains. *Analyst* **2020,** *145* (18), 6097-6110.
43. Beier, H. T.; Cowan, C. B.; Chou, I. H.; Pallikal, J.; Henry, J. E.; Benford, M. E.; Jackson, J. B.; Good, T. A.; Coté, G. L., Application of Surface-Enhanced Raman Spectroscopy for Detection of Beta Amyloid Using Nanoshells. *Plasmonics* **2007,** *2* (2), 55-64.
44. Kim, S. K.; Kim, M. S.; Suh, S. W., Surface-enhanced Raman scattering (SERS) of aromatic amino acids and their glycyl dipeptides in silver sol. *J. Raman Spectrosc.* **1987,** *18* (3), 171-175.
45. Zhou, Z.; Huang, G. G.; Kato, T.; Ozaki, Y., Experimental parameters for the SERS of nitrate ion for label-free semi-quantitative detection of proteins and mechanism for proteins to form SERS hot sites: a SERS study. *J. Raman Spectrosc.* **2011,** *42* (9), 1713-1721.
46. Rygula, A.; Majzner, K.; Marzec, K. M.; Kaczor, A.; Pilarczyk, M.; Baranska, M., Raman spectroscopy of proteins: a review. *J. Raman Spectrosc.* **2013,** *44* (8), 1061-1076.
47. Bao, Y.; Li, Y.; Ling, L.; Xiang, X.; Han, X.; Zhao, B.; Guo, X., Label-Free and Highly Sensitive Detection of Native Proteins by Ag IANPs via Surface-Enhanced Raman Spectroscopy. *Anal. Chem.* **2020,** *92* (21), 14325-14329.
48. Samuel, A. Z.; Umapathy, S., Energy funneling and macromolecular conformational dynamics: a 2D Raman correlation study of PEG melting. *Polym. J.* **2014,** *46* (6), 330.

49. Navarro, J. R.; Manchon, D.; Lerouge, F.; Blanchard, N. P.; Marotte, S.; Leverrier, Y.; Marvel, J.; Chaput, F.; Micouin, G.; Gabudean, A. M.; Mosset, A.; Cottancin, E.; Baldeck, P. L.; Kamada, K.; Parola, S., Synthesis of PEGylated gold nanostars and bipyramids for intracellular uptake. *Nanotechnology* **2012,** *23* (46), 465602.

50. Häkkinen, H., The gold–sulfur interface at the nanoscale. *Nat. Chem.* **2012,** *4* (6), 443.

CHAPTER 4

Toward Improving Lateral Flow Assays by Versatile Histidine Conjugation to AgAu Multibranched Nanoshells for the Detection and Study of SARS-CoV-2 via Surface Enhanced Raman Scattering

4.1 Abstract

Recently, the rapid spread of COVID-19 variants has overwhelmed the healthcare industry. There is an unprecedented need for more tests to adapt to reoccurring and emerging pathogens. Advances in serological tests have combined surface-enhanced Raman scattering (SERS) with lateral flow assays; however, the assays heavily rely on reporter molecules and multi-step nanoparticle conjugations. In this work, we have developed a new method to detect both the SARS-CoV-2 S1 spike protein and the anti-SARS-CoV-2 antibodies by anchoring the N_τ nitrogen on a his-tagged spike protein to a multibranched gold nanoshell for detection by SERS. Multibranched gold nanoshells were prepared using $HAuCl_4$, $AgNO_3$, and ascorbic acid to improve the optical and morphological properties of smooth ~150 nm gold nanoshells for detecting proteins. The multibranched gold nanoshells were gently mixed with a his-tagged SARS-CoV-2 S1 spike protein, purified then mixed with Anti-SARS-CoV-2 monoclonal antibodies. Raman and SERS measurements of the spike protein and monoclonal antibody with a histidine tag showed a significant increase in peak intensity as compared to samples without histidine. Enhanced SERS peaks from the spike protein at 1079, 1178, and 1592 cm^{-1} are attributed to δ =N-H, νC-N, νC=C, respectively. Enhanced peaks from the Anti-SARS-CoV-2 monoclonal antibody at 861, 1205, 1454, and 1630 cm^{-1} can be assigned to νN-H, νC-C, C-H def, and νC=O associated with the phenylalanine and tyrosine rich region closest to the binding sites on mAb. This method could improve and simplify serological assays while enabling the direct detection of SARS-CoV-2 S1 spike protein and Anti-SARS-

CoV-2 monoclonal antibody in aqueous solution without using Raman reporter molecules.

4.2 Introduction

Severe acute respiratory syndrome coronavirus 2 (SARS-CoV-2) has infected over 440 million people worldwide with COVID-19 as of February 2022.[1, 2] Frequent testing has been proven to be vital in limiting the spread of COVID-19.[3, 4] Paper-based lateral flow immunoassays (LFIA) are the most prevalent rapid screening method because they enable quick and point of care testing.[5-7] Current LFIA methods offer a yes/no answer dependent upon subjective interpretation of a colorimetric result. The stability of antibody-coated gold sols limits the accuracy of LFIA. LFIA was pared with surface enhanced Raman scattering (SERS) to improve the accuracy and precision by Liang *et al*.[8]

Pairing (SERS) with LFIA adds both a second metric to confirm the reliability of the results and a method to obtain quantitative data.[9, 10] Current SERS LFIA methods utilize a concoction of antibodies, dyes, and molecules for conjugation to achieve sensitivity down to pg/mL.[9-17] In 2021, Liu *et al.* used SERS LFIA to detect anti-SARS-CoV-2 IgM and IgG at 800 times the sensitivity of LFIA via the Raman reporter molecule DTNB. Studying anti-SARS-CoV-2 immunoglobulin and SARS-CoV-2 spike proteins directly could enable surveillance of the spread of variants.

However, to study the molecules directly, immobilizing SARS-CoV-2 spike protein and anti-SARS-CoV-2 antibodies within nanometers of the sensor surface is crucial.

The performance of the SERS substrate depends on its localized surface plasmon resonance (LSPR), and the plasmonic properties of the SERS substrate depend on its nanostructure. Gold nanostars have shown increased SERS activity, with reported enhancement factors 2−5 orders of magnitude higher than their solid spherical counterparts.[18] The increased SERS activity has been attributed to the spikes that produce strong EM field enhancements due to electron confinement. Additionally, an increase in surface area is associated with nanostars allowing more interaction of the analytes and the nanostar.[19-21] As such, nanostars exhibit both larger SERS activity without the need for aggregation.[22] Hollow structures such as HGNs are highly tunable with both internal and external surfaces, whose coupling further enhances the EM field as well as their SERS capabilities.[23] Our lab has recently demonstrated that it is possible to introduce spikes on the surface of HGNs, which allows the combination of the properties of HGNs with those of gold nanostars into one structure, hollow gold nanostars, (HNSs), with improved SERS activity.[24, 25]

4.2.1 Application of Histidine to Recover Metals from Solution

The challenges associated with direct detection are simplifying molecules associated with the conjugation process that adds to the spectroscopic background and removing Raman reporter molecules. Both processes would be aided by a small molecule capable of bringing the analytes within a few nanometers of the

nanoparticle surface. Options for simplifying the conjugation technique are EDC/NHS, PEGylation, and amino acid conjugation. Histidine conjugation is likely a competitive technique based on size and metal affinity.

Histidine-rich proteins are essential for biological processes involving pH buffer, antioxidant, and metal chelation.[26] While histidine has been largely used with Ni(II), Cu(II), Co(II), or Zn(II), there is evidence that the imidazole ring coordinates to Au(III) and likely gold nanoparticles.[26-39] A recent DFT study revealed that the imidazole ring higher rate of adsorption for gold than the carboxylate group.[32] Additionally, when bound to a metal such as gold, νC-N_τ shifts from 1577 to 1612 cm^{-1}.[37, 40, 41] These findings suggest that imidazole is a promising moiety for SERS based detection. Nitrogen on imidazole has a peak shift from 1577 to 1612 cm^{-1} when bound to gold. Spike proteins are purified using immobilized metal affinity chromatography via histidine tags. We can utilize his-tagged spike proteins to capture SARS-CoV-2 antibodies.

This study employs histidine over EDC/NHS and PEGylation for nanoparticle conjugation to achieve the direct detection of anti-SARS-CoV-2 monoclonal antibodies, SARS-CoV-2 spike protein, and SARS-CoV-2 antigen-antibody bond. Because histidine has an affinity for gold, we were able to conjugate the spike protein to the multibranched gold nanoshells directly, and then detect the spike protein binding to the antibody in an aqueous solution without any need for Raman reporter molecules. Our results show that his-tagged antigens can be used to detect SARS-

CoV-2 monoclonal antibodies down to 9.20x10-9 M without the need for Raman reporters.

4.3. Results and Discussion

Scheme 4.1 illustrates the metal coordination of histidine to the multibranched gold nanoshells for SERS based detection of Anti-SARS-CoV-2 monoclonal antibodies (mAbs) in solution. The SERS substrate, multibranched gold nanoshells (MGNs), was coated with a histidine-tagged SARS-CoV-2 spike protein. On imidazole, the nitrogen with an available lone pair of electrons (Nτ) anchored the spike protein to the MGN. The mAbs were linked to the MGNs through typical antibody-antigen reactions. Spectroscopic analysis at each step revealed the addition of Raman modes associated with successful conjugation.

4.3.1 Synthesis Optical and Structural Features of Multibranched Gold Nanoshells

Multibranched gold nanoshells were synthesized in a single step then conjugated to SARS-CoV-2 spike protein followed by an anti-spike mAb. First, Au^{3+}

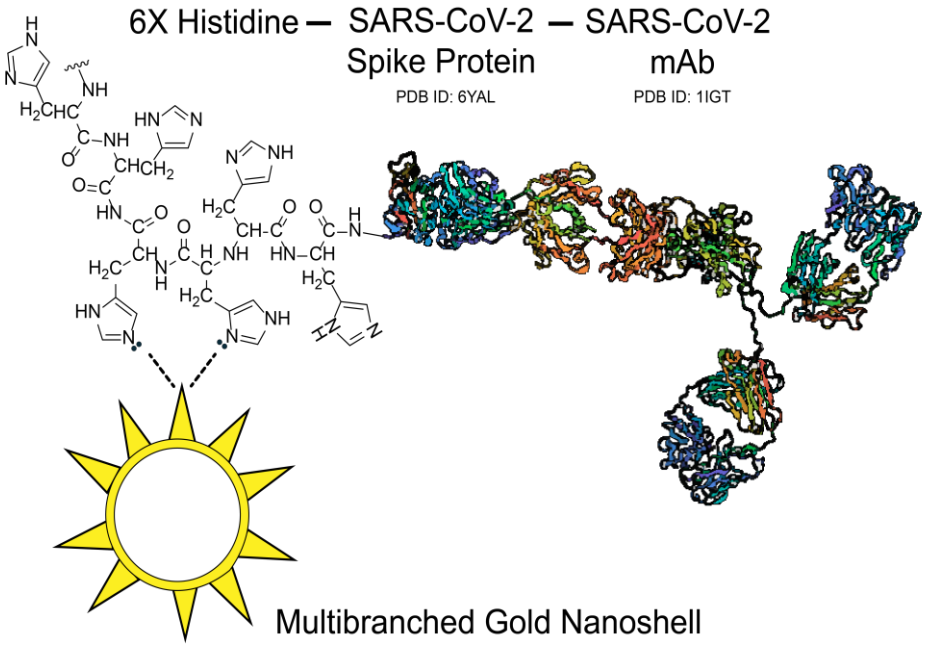

Scheme 4.1. Illustration of two adjacent imidazole rings from a 6-histidine tagged SARS-CoV-2 S1 spike protein coordinating to the SERS substrate. The Nτ anchors the spike protein and Anti-SARS-CoV-2 monoclonal antibody to the multibranched gold nanoshell.

ions were reduced onto the surface of 157± 10 nm gold nanoshells in the presence of Ag^{+} using ascorbic acid following modified a seed templated nanostars synthesis by the Dinh group.[20, 24] The surface of the nanoshells became spiny and urchin-like. Following the formation of MGNs, the nanoparticles were washed and resuspended in MilliQ water. Very soon after, His-tagged SARS-CoV-2 spike protein (S1) was mixed with the SERS substrate for 6 hours to ensure the His-tagged S1 coordinated to the MGNs via N_{τ} on the imidazole moitety.[20] Afterward, unbound S1 was removed via centrifugation and the loose pellet was resuspended then gently stirred with Anti-SARS-CoV-2 mAb for one hour. Unbound mAb was then removed via gentle centrifugation. The supernatant from both the S1 and mAb conjugation steps was

stored. After conjugation was completed, the amount of protein was characterized using a BCA assay for each sample and supernatant solution.

Quantitative results of the S1 and the mAb conjugation to the multibranched gold nanoshells were obtained using a BCA assay, as seen in Figure 4.1. A calibration curve was constructed using the absorption intensity of BSA complexing Cu^{+} ions at 562 nm. There results were averaged for three samples. The MGN+S1 samples contained of 1.0 mL of MGNs mixed with 30 µL of 100µg per 100 µL S1. A 30 µL samples of S1 was analyzed as a control. The BCA assay showed the molar concentration of the control was $3.43x10^{-8}$ M. $9.20x10^{-9}$ M of S1 adhered to the MGNs. The MGN+S1+mAb samples were prepared by adding 10 µL of 1.0 mg per 1.0 mL. The MGN+S1+mAb control contained 30 µL of S1 plus 10 µL of 1.0 mg per 1.0 mL. The BCA assay showed the molar concentration of the control was $4.03x10^{-7}$ M. The total protein content that adhered to the MGNs was $2.44x10^{-8}$ M.

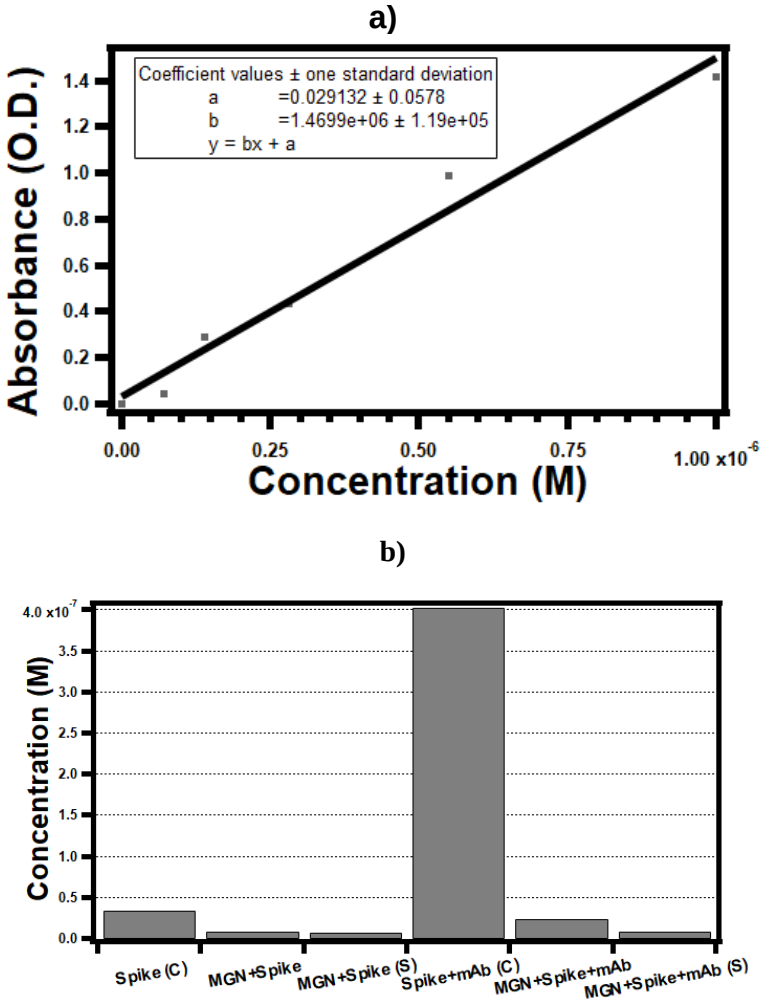

Figure 4.1. Results of the Bicinchoninic acid assay where a) is the calibration curve of the BSA standard dilution series constructed from absorption spectroscopy intensity at 562 nm b) the results of the BCA assay for multibranched gold nanoshell (MGN) coated in spike protein and spike protein plus Anti-SARS-CoV-2 mAb. Controls were marked with (C), and supernatant samples were marked with and (S).

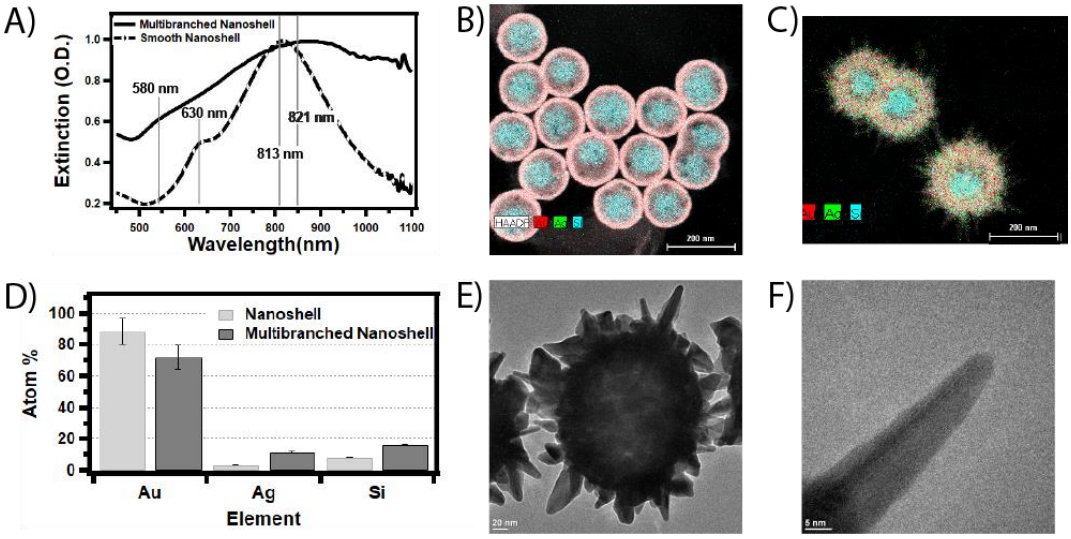

Figure 4.2. The optical, elemental, and structural properties of the nanoshell seed and multibranched gold nanoshells where (a) shows the UV-Vis extinction spectra of each, (b, c) show Au (red), Ag (green), and Si (teal) overlaid on the black and white HAADF image of each nanostructure, (d) shows the weight percent of each element in b, c, and (e, f) show the HRTEM analysis of the multibranch gold nanoshells with lattice resolved image of one of the branches.

As shown in Figure 4.2, the morphological changes improved the optical properties of the nanoshells. Multibranched gold nanoshells were synthesized from 157 ±10 nm nanoshell template. Extinction spectra in Figure 4.2A showed a blue-shift of the localized surface plasmon resonance (LSPR) peak associated with the nanoshell cavity and a red-shifted plasmon mode associated with nanoshell. During the multibranch synthesis, Au^{3+} ions form nanoscale Au^{0} cones on the nanoshell surface. Additionally, a small amount of Ag^{+} ions also deposit on the surface. The multibranch synthesis changes the structure in two pronounced ways: a thicker nanoshell and barbed projections form on the previously smooth surface.

The extinction spectrum of the nanoshell seed particle and multibranched nanoshells were characterized by two plasmon modes as seen in Figure 4.2A. The pair of peaks found in the nanoshells at 630 and 813 nm are caused by two dipolar plasmon modes. [42-44] The longer wavelength mode corresponds to symmetric coupling resembling a dipole bonding mode. The shorter wavelength mode corresponds to antisymmetric coupling of the cavity plasmon and the outer shell plasmon resembling a dipole antibonding mode (+- +-). Figure 4.3 shows the blue-shift and red-shift analysis of the extinction spectra of the nanoshell and the MGN. After the multibranch synthesis, the LSPR peak at 630 nm blue-shifted to 580 nm.

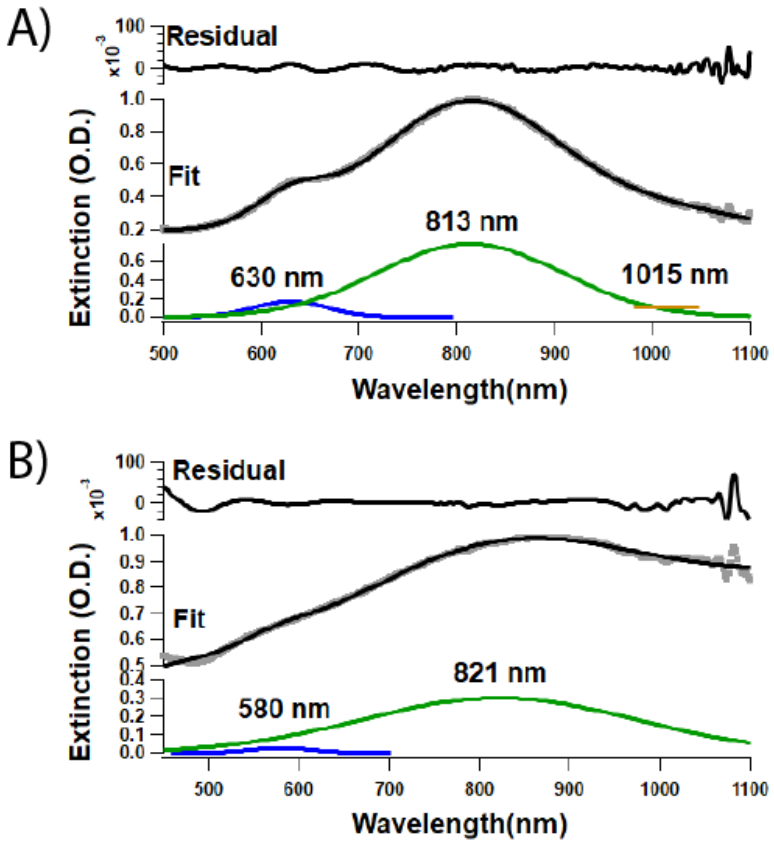

Figure 4.3. Multipeak fit of the extinction spectra of A) nanoshells and B) MGN. The top black spectra is the difference between the extinction spectrum and the fit spectrum. The grey peaks show the fit. The blue and green peaks show the fit results.

A change in shell thickness occurred because of increased shell thickness. The diameter shell thickness measurements were performed Image J using HAADF and HRTEM images as seen in Figures 4.2B, 4.2C, 4.2E, and 4.2F. Au deposited onto the nanoshell changing the shell thickness from 12 nm to over 44 nm. The ratio of the diameter to thickness also called the aspect ratio decreased from 12 to 2.7. The dramatically decreased aspect ratio may explain part of the 50 nm blue-shift of the plasmon mode associated with the cavity. Additionally, the blue shift can be

understood by analyzing the role of Ag^0. Atta, Beetz, and Fabris documented the cavity plasmon mode blue shifts with increasing $AgNO_3$ used in the multibranch synthesis.[45, 46] Increasing deposits of Ag^0 change the plasmon modes to be closer to colloidal silver. The amount of silver in both nanostructures was characterized with Energy Dispersive X-Ray Spectroscopy (EDX); the results are displayed in Figure 4.2D. The EDX spectra and elemental mapping of both the nanoshell and MGN can be seen in Figures 4.3 and 4.4. The atomic weight % of gold decreased by 10% from nanoshell to multibranched nanoshell. The atomic weight% of silver increased from 0% to 21 ± 2%. The amount of Ag^0 on the surface of the nanoparticle decreased the full width at half the maximum (FWHM) by 10 nm resembling the narrow peak width of silver nanoparticles.

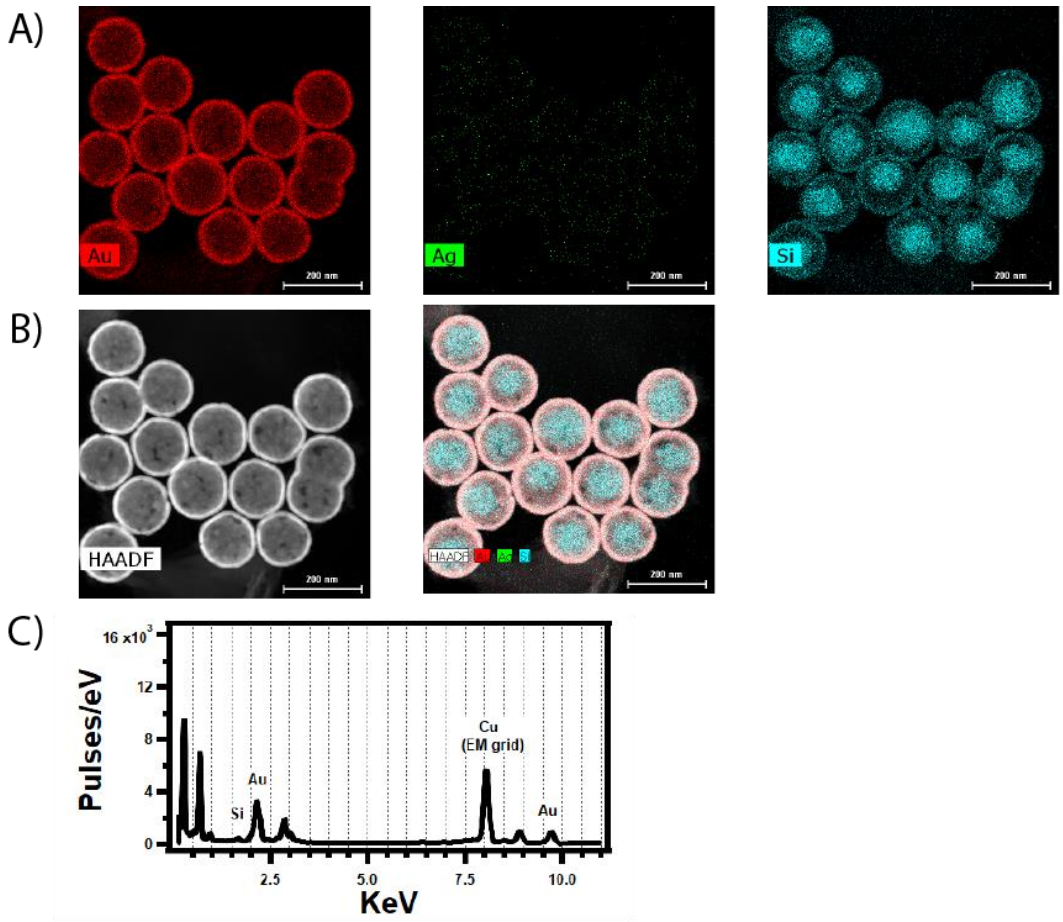

Figure 4.4. Elemental analysis with EDX spectra of the nanoshells where A) is the HAADF image, B) is the elemental map of gold, C) is the elemental map of silicon, and D) is the EDX spectra.

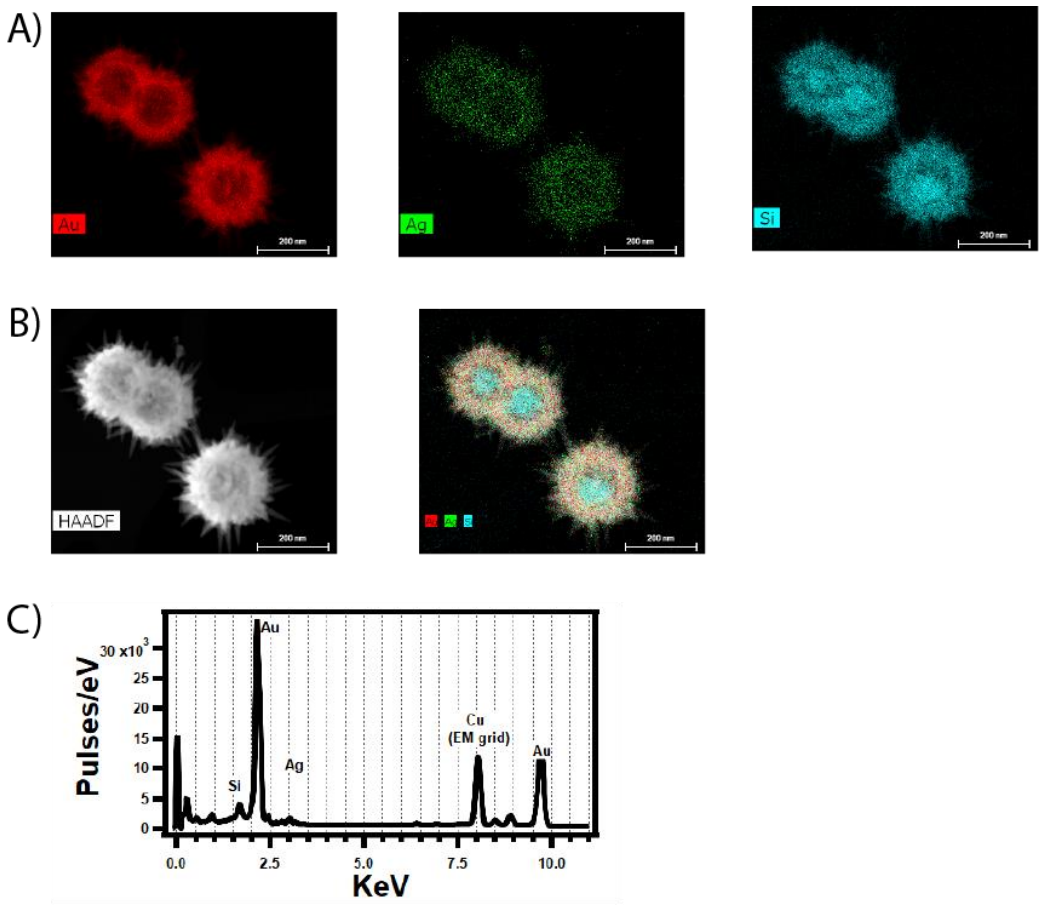

Figure 4.5. Elemental analysis with EDX spectra of the MGNs where A) is the HAADF image, B) is the elemental map of gold, C) is the elemental map of silver, and D) is the EDX spectra.

After the multibranch synthesis, the low-energy plasmon mode at 813 nm red-shifted to 821 nm, and the FWHM increased by 136 nm. The average core diameter remained relatively the same. Nehl and Nao used a combination of atomic orbitals to model the core and spike of nanostars. The nanostars tips contributed to the longer wavelength plasmon mode and caused peak broadening.[47-49] The core diameter of the nanoshells was 129 ± 8 nm, and the core diameter of the multibranched nanoshells was 122 ± 6 nm. Silver on the surface of the seed particle directed the growth of sharp

gold projections. The large peak broadening is characteristic of the formation of an urchin-like surface. The large increase in FWHM extends the LSPR into the near-IR boosting the utility of MGNs as a SERS substrate for proteins.

Multibranched structure is necessary to detect weak Raman scatters such as protein antigens and antibodies. An increase in the number of SERS hot spots at the tips of the branches and the large increase in surface area enable more sensitive detection. Electron tomography was utilized in reconstructing the 3D shape of the MGN from a series of 2D-TEM images taken at different tilt angles. Figure 4.5 displays the HAADF image of a single MGN, a slice of the reconstruction, and the full reconstructed volume. The HAADF image in Figure 4.5A resembled the average MGN core diameter and spike density. The slice in Figure 4.5B, allowed for a more accurate analysis of the thickness of the MGN. The reconstructed volume in Figure 4.5C, enabled quantification of characteristics about the spike length and number. There was an average of 15 spikes longer than 10 nm that were visible in Figure 4.5C and Figure 4.6. The average spike length was 19.3 nm, and the average width at half of the height was 7.14 nm. The calculated surface area of the average spike is 260 nm^2. The calculated surface area of an MGN is 0.106 μm^2 as compared to the surface area of the gold nanoshell seed, which was 0.072 μm^2. The large shifted LSPR, numerous hot spots, and increased surface area make MGNs an ideal SERS substrate. Additionally, the cavity in the MGNs help shift the LSPR to the near-IR and reduce the amount of total gold per particle.

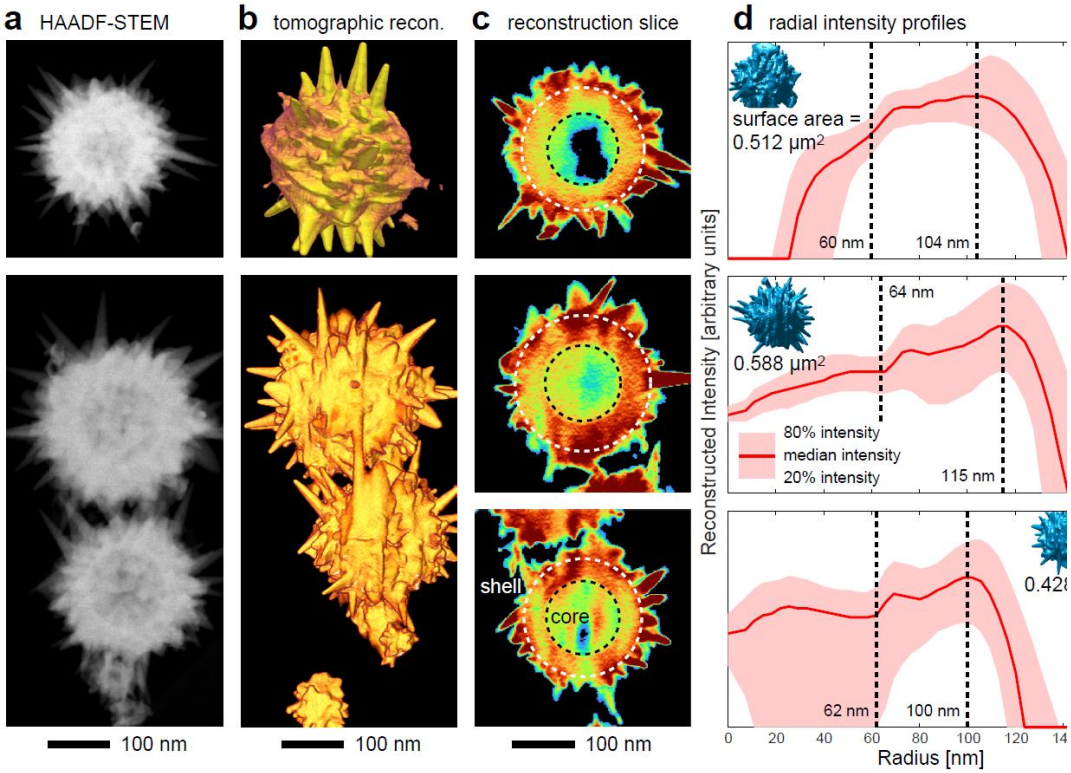

Figure 4.6. 3D tomographic reconstructions of MGNs. (a) A series of 2D STEM-HAADF images were acquired over a range of tilt angles. (b) Particle surface visualizations were rendered using TomViz. (c) Slices of the 3D reconstructions through the particle centers, with the estimated core and shell radii overlaid. (d) Radial intensity profiles for three multibranched gold nanoshells, showing the intensity distributions at 20%, 50% (the median), and 80% for each radial bin. Isosurfaces and associated estimates of the surface area are inset into each plot.

4.3.2 Evaluation of Histidine Tag via Raman and SERS

A key feature of the following experiments was the utilization of a histidine tag on the SARS-CoV-2 spike protein. The Raman and SERS spectra of histidine were first evaluated to understand whether imidazole could reliably coordinate to MGNs. Imidazole has two nitrogen atoms: one has a lone pair of electrons involved in resonance (N_π) and the other nitrogen has a lone pair perpendicular to the pi bonds

of the ring (N_τ).[50] A recent study on the protonation state of each nitrogen in imidazole revealed that N_π remains protonated from pH 1 to 13 while N_τ has a free lone pair at pH 7 and above.[51] Figure 4.7A displays the Raman and SERS spectra of histidine. The peaks of interest were 1267 cm^{-1} (δ=C-H, ν=C-N), 1370 cm^{-1} (Nτ-M), and 1577cm^{-1} (ν C=C, δN-H), and 1600 cm^{-1} (νC=C, νC=N). The full list of the Raman and SERS shifts along with the peak assignments of histidine are summarized in Table 4.1. Each of the four Raman shifts above involve the Nτ or Nπ nitrogen atoms and the and C_4=C_5 stretch, labeled in Figure 4.7B.

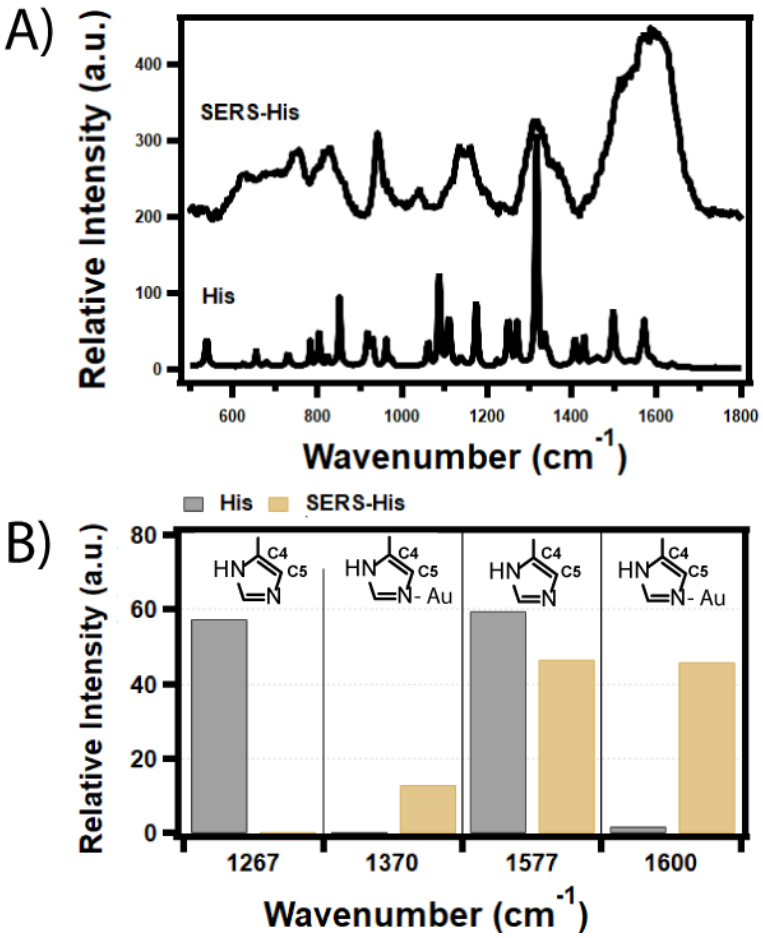

Figure 4.7. Comparison of A) Raman and SERS spectra of histidine along with B) a comparison of peaks association with unbound imidazole to gold bound imidazole. The small imidazole structure is labeled from left to right C_4 and C_5. Excitation wavelength: 785 nm, acquisition time: 30 sec and 10 sec.

Furthermore, histidine bound to gold underwent changes in intensity and peak position.[52] The peaks at 1267 and 1370 cm^{-1} correlated to the coordination state of Nτ.[53] As seen in Figure 4.3B, the intensities of 1267 and 1577 cm^{-1} are the highest for unbound Nτ. Chelating a metal center has been known to shorten the bond length of C_4=C_5 , labelled in Figure 4.3B, which in turn would increase the stretching

frequency. As a result, an increase in Raman shift from 1577 cm^{-1} to 1600 cm^{-1} was observed. This shift is a marker for the coordination of Nτ to MGNs.

4.3.3 SERS Detection of SARS-CoV-2 Spike Protein and Monoclonal Human Antibody

SARS-CoV-2 receptor binding domain-targeting mAbs interact with the receptor binding motif on the spike protein through key amino acid residues.[54, 55] The amino acids that are readily detected via Raman spectroscopy are phenylalanine, tyrosine, and Amide III (νC-N, δN-H). Figure 4.8 shows SERS spectra of his-tagged SARS-CoV-2 S1 and Anti-SARS-CoV-2 mAb along with the Raman spectra of his-tagged SARS-CoV-2 S1. The intensity of the Raman shifts of his-tagged SARS-CoV-2 S1 and Anti-SARS-CoV-2 mAb were weak without a SERS substrate – histidine anchor. The distinct peaks of the His-tagged spike protein were 1310 and 1600 cm^{-1}. Both peaks were broad and are likely attributed to histidine. The Anti-SARS-CoV-2 mAb SERS spectrum had three distinct peaks at 622, 1079, and 1590 cm^{-1}. The peak at 622 cm^{-1} is likely due to the in-plane ring bending of. Both the 1079 and 1590 cm^{-1} are associated with δ =N-H δ =N-H. The two spectra without both histidine and a SERS substrate suggest that this anchor is needed to achieve SERS sensitivity enough to detect both the spike protein and mAb.

Both samples with MGN and a his-tag had enhanced signals associated with amino acid residues of the spike protein and mAb. The enhanced peaks from the spike protein were 1079, 1178, and 1592 cm^{-1} and are associated with δ =N-H, νC-N,

νC=C respectively. The enhanced peaks from the his-S1-mAb were 861, 1205, 1454, 1605, and 1630 associated with phenylalanine, tyrosine, and amide stretches. The networks of hydrophilic interactions at spike/mAb interface quenched the SERS signals at 1079 cm^{-1}.[56] A full list of peaks associated with both samples can be seen in Table 4.1.

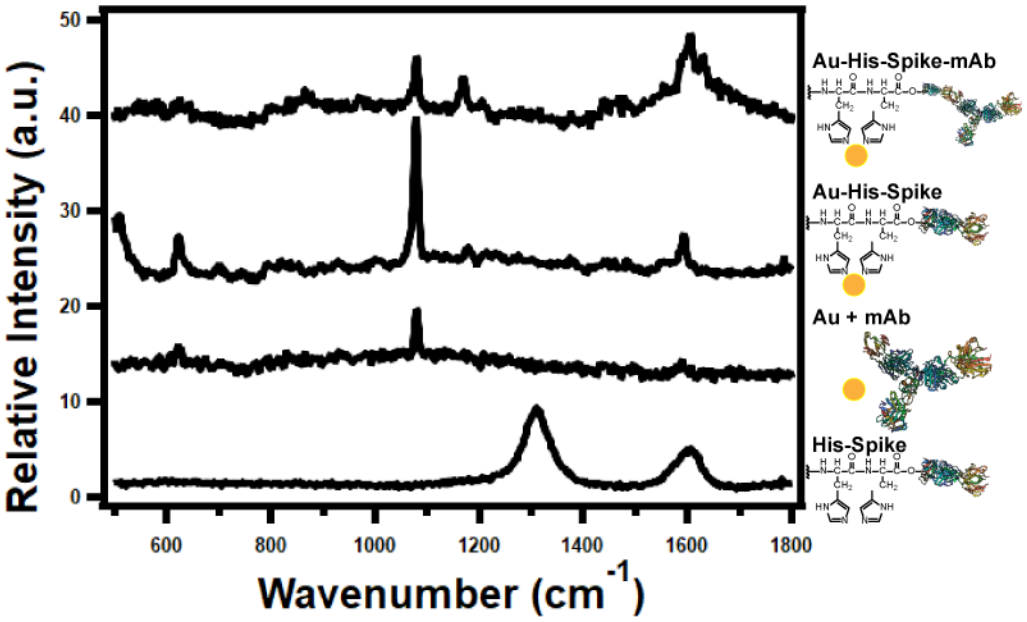

Figure 4.8. Representative SERS and Raman spectra of MGN-6X His-S1-mAb, MGN-6X His-S1, and MGN+mAb and 6XHis-S1 (from the top to the bottom). An illustration on the right shows the different components. Excitation wavelength: 785 nm, acquisition time: 30 sec.

Table 4.1. Present are the full assignements of the vibational modes associated with each compenent and combination of MGN-His-tagged Spike-Anti-SARS-CoV-2 mAb. Analysis of the Raman spectra of Histidine and His-tagged spike protein. Analysis of the SERS spectra of Histidine, His-tagged spike protein, Anti-SARS-CoV-2 mAb without a his-tag, and His-tagged spike-mAb.

Raman		**SERS**				**Assignment**
Histidine	His-Spike Antigen	Histidine	His-Spike Antigen	SARS-Cov-2 mAb	His-Spike-mAb	
		621	624	622	632	δ ring ip bend
		698				N-H def
760		753				δ =C-H oop
832		825				δ =C-H oop
					861	ν (N-H) Trp, Tyr
948		943				δ ring ip
		1013				δ=C-H, ip
1048		1042			1050	δ N-H ip
1075			1078	1079	1078	δ =N-H
1100		1106				ν=C-N, δ=C-H
1166		1160			1169	νC-N, δ=C-H
		1172	1178			νC-N, δ=C-H
					1205	ν (C-C) Trp, Phe
1245						δ=C-H, ν=C-N
1267						δ=C-H, ν=C-N
1314	1310	1316				νC=N, νC-N
		1370				Nτ-M
1407						δ CH COO-
1430		1433				δ CH2
					1454	C-H def
		1468				δ (N-H) ip
1501		1513				δ N-H ip
		1560				ν(C=C), δ(N-H)
1577						ν C=C, δN-H
	1600		1592	1590		δN-H, C-H ip, νC=C, νC=N
		1600			1605	C=C
					1630	Tyr, Trp, Phe ,νC=O

N- stretch, δ-deformation/bending, ip – in plane, oop – out of plane,

4.4. Conclusion

The method discussed throughout this paper aimed to eliminate the need for reporter molecules enabling the direct spectroscopic detection of SARS-CoV-2 spike and Anti-SARS-CoV-2 antibodies. Multibranched gold nanoshell SERS substrates were designed with a broad near-IR LSPR needed to avoid fluorescence backgrounds associated with biological molecules. The near-IR shift was achieved by introducing a spiky surface on 157 nm smooth gold nanoshells. After the multibranch synthesis, the low energy plasmon mode at 813 nm red-shifted to 821 nm, and the FWHM increased by 136 nm. The average spike length was 19.3 nm, and the average width at half of the height was 7.14 nm. The multibranched synthesis increased the surface area by 0.03 μm^2 per particle. The LSPR, numerous hot-spot generating spikes, and increased surface area made MGNs an ideal SERS substrate.

Histidine tags were utilized as a simple nanoparticle-analyte linker. Raman and SERS measurements of the spike protein and mAb without both histidine and a SERS substrate had weak Raman signals. Raman and SERS measurements of the spike protein and mAb with MGN and a his-tag had enhanced signals associated with amide stretches from the spike protein and phenylalanine, tyrosine from the mAb. The enhanced peaks from the spike protein at 861, 1205, 1454, 1605, and 1630 associated with phenylalanine, tyrosine, and amide stretches The method developed here could be applied to improve the speed and simplicity of serological assays.

4.5. References

1. Dong, E.; Du, H.; Gardner, L. An Interactive Web-Based Dashboard to Track Covid-19 in Real Time. *Lancet Infect. Dis.* **2020,** *20* (5), 533-534.
2. Zhou, F.; Yu, T.; Du, R.; Fan, G.; Liu, Y.; Liu, Z.; Xiang, J.; Wang, Y.; Song, B.; Gu, X.; Guan, L.; Wei, Y.; Li, H.; Wu, X.; Xu, J.; Tu, S.; Zhang, Y.; Chen, H.; Cao, B. Clinical Course and Risk Factors for Mortality of Adult Inpatients with Covid-19 in Wuhan, China: A Retrospective Cohort Study. *The Lancet* **2020,** *395* (10229), 1054-1062.
3. Younes, N.; Al-Sadeq, D. W.; Al-Jighefee, H.; Younes, S.; Al-Jamal, O.; Daas, H. I.; Yassine, H. M.; Nasrallah, G. K. Challenges in Laboratory Diagnosis of the Novel Coronavirus Sars-Cov-2. *Viruses* **2020,** *12* (6), 582.
4. Huang, Y.; Yang, C.; Xu, X. F.; Xu, W.; Liu, S. W. Structural and Functional Properties of Sars-Cov-2 Spike Protein: Potential Antivirus Drug Development for Covid-19. *Acta Pharmacol Sin* **2020,** *41* (9), 1141-1149.
5. Fu, X.; Cheng, Z.; Yu, J.; Choo, P.; Chen, L.; Choo, J. A Sers-Based Lateral Flow Assay Biosensor for Highly Sensitive Detection of Hiv-1 DNA. *Biosens Bioelectron* **2016,** *78*, 530-537.
6. Wang, C.; Liu, M.; Wang, Z.; Li, S.; Deng, Y.; He, N. Point-of-Care Diagnostics for Infectious Diseases: From Methods to Devices. *Nano Today* **2021,** *37*, 101092.
7. Kim, S.; Hao, Y.; Miller, E. A.; Tay, D. M. Y.; Yee, E.; Kongsuphol, P.; Jia, H.; McBee, M.; Preiser, P. R.; Sikes, H. D. Vertical Flow Cellulose-Based Assays for Sars-Cov-2 Antibody Detection in Human Serum. *ACS Sens* **2021,** *6* (5), 1891-1898.
8. Liang, J.; Liu, H.; Lan, C.; Fu, Q.; Huang, C.; Luo, Z.; Jiang, T.; Tang, Y. Silver Nanoparticle Enhanced Raman Scattering-Based Lateral Flow Immunoassays for Ultra-Sensitive Detection of the Heavy Metal Chromium. *Nanotechnology* **2014,** *25* (49), 495501.

9. Chen, S.; Meng, L.; Wang, L.; Huang, X.; Ali, S.; Chen, X.; Yu, M.; Yi, M.; Li, L.; Chen, X.; Yuan, L.; Shi, W.; Huang, G. Sers-Based Lateral Flow Immunoassay for Sensitive and Simultaneous Detection of Anti-Sars-Cov-2 Igm and Igg Antibodies by Using Gap-Enhanced Raman Nanotags. *Sens Actuators B Chem* **2021,** *348*, 130706.
10. Chen, Z.; Zhang, Z.; Zhai, X.; Li, Y.; Lin, L.; Zhao, H.; Bian, L.; Li, P.; Yu, L.; Wu, Y.; Lin, G. Rapid and Sensitive Detection of Anti-Sars-Cov-2 Igg, Using Lanthanide-Doped Nanoparticles-Based Lateral Flow Immunoassay. *Anal Chem* **2020,** *92* (10), 7226-7231.
11. Khlebtsov, B.; Khlebtsov, N. Surface-Enhanced Raman Scattering-Based Lateral-Flow Immunoassay. *Nanomaterials* **2020,** *10* (11), 2228.
12. Yadav, S.; Sadique, M. A.; Ranjan, P.; Kumar, N.; Singhal, A.; Srivastava, A. K.; Khan, R. Sers Based Lateral Flow Immunoassay for Point-of-Care Detection of Sars-Cov-2 in Clinical Samples. *ACS Appl. Bio Mater.* **2021,** *4* (4), 2974-2995.
13. Liu, H.; Dai, E.; Xiao, R.; Zhou, Z.; Zhang, M.; Bai, Z.; Shao, Y.; Qi, K.; Tu, J.; Wang, C. Development of a Sers-Based Lateral Flow Immunoassay for Rapid and Ultra-Sensitive Detection of Anti-Sars-Cov-2 Igm/Igg in Clinical Samples. *Sens. Actuators, B* **2021,** *329*, 129196.
14. Chen, R.; Ren, C.; Liu, M.; Ge, X.; Qu, M.; Zhou, X.; Liang, M.; Liu, Y.; Li, F. Early Detection of Sars-Cov-2 Seroconversion in Humans with Aggregation-Induced near-Infrared Emission Nanoparticle-Labeled Lateral Flow Immunoassay. *ACS Nano* **2021,** *15* (5), 8996-9004.
15. Serebrennikova, K. V.; Byzova, N. A.; Zherdev, A. V.; Khlebtsov, N. G.; Khlebtsov, B. N.; Biketov, S. F.; Dzantiev, B. B. Lateral Flow Immunoassay of Sars-Cov-2 Antigen with Sers-Based Registration: Development and Comparison with Traditional Immunoassays. *Biosensors (Basel)* **2021,** *11* (12).

16. Kim, K.; Kashefi-Kheyrabadi, L.; Joung, Y.; Kim, K.; Dang, H.; Chavan, S. G.; Lee, M.-H.; Choo, J. Recent Advances in Sensitive Surface-Enhanced Raman Scattering-Based Lateral Flow Assay Platforms for Point-of-Care Diagnostics of Infectious Diseases. *Sens. Actuators, B* **2021,** *329*, 129214.
17. Liu, H.; Dai, E.; Xiao, R.; Zhou, Z.; Zhang, M.; Bai, Z.; Shao, Y.; Qi, K.; Tu, J.; Wang, C.; Wang, S. Development of a Sers-Based Lateral Flow Immunoassay for Rapid and Ultra-Sensitive Detection of Anti-Sars-Cov-2 Igm/Igg in Clinical Samples. *Sens. Actuators, B* **2021,** *329*, 129196.
18. Nalbant Esenturk, E.; Hight Walker, A. Surface-Enhanced Raman Scattering Spectroscopy Via Gold Nanostars. *Journal of Raman Spectroscopy: An International Journal for Original Work in all Aspects of Raman Spectroscopy, Including Higher Order Processes, and also Brillouin and Rayleigh Scattering* **2009,** *40* (1), 86-91.
19. Yuan, H.; Khoury, C. G.; Hwang, H.; Wilson, C. M.; Grant, G. A.; Vo-Dinh, T. Gold Nanostars: Surfactant-Free Synthesis, 3d Modelling, and Two-Photon Photoluminescence Imaging. *Nanotechnology* **2012,** *23* (7), 075102.
20. Khoury, C. G.; Vo-Dinh, T. Gold Nanostars for Surface-Enhanced Raman Scattering: Synthesis, Characterization and Optimization. *J. Phys. Chem. C* **2008,** *112* (48), 18849-18859.
21. Barbosa, S.; Agrawal, A.; Rodriguez-Lorenzo, L.; Pastoriza-Santos, I.; Alvarez-Puebla, R. A.; Kornowski, A.; Weller, H.; Liz-Marzan, L. M. Tuning Size and Sensing Properties in Colloidal Gold Nanostars. *Langmuir* **2010,** *26* (18), 14943-50.
22. Le Ru, E. C.; Etchegoin, P. G. Quantifying Sers Enhancements. *MRS Bull.* **2013,** *38* (8), 631.
23. Mahmoud, M.; Snyder, B.; El-Sayed, M. Surface Plasmon Fields and Coupling in the Hollow Gold Nanoparticles and Surface-Enhanced Raman Spectroscopy. Theory and Experiment. *J. Phys. Chem. C* **2010,** *114* (16), 7436-7443.

24. Allen, A. C.; Efrem, M.; Mahalingam, U.; Guarino-Hotz, M.; Foley, A. R.; Raskatov, J. A.; Song, C.; Lindley, S. A.; Li, J.; Chen, B.; Zhang, J. Z. Hollow Gold Nanosphere Templated Synthesis of Pegylated Hollow Gold Nanostars and Use for Sers Detection of Amyloid Beta in Solution. *J. Phys. Chem. B* **2021,** *125* (44), 12344-12352.
25. Guarino-Hotz, M.; Allen, A. L. C.; Wang, A.; Zou, S.; Zhang, J. Z. Near-Infrared Light Absorbing Silver-Coated Hollow Gold Nanostars for Surface-Enhanced Raman Scattering Detection of Bovine Serum Albumin Using Capping Ligand Exchange. *J. Phys. Chem. C* **2022**.
26. Holecek, M. Histidine in Health and Disease: Metabolism, Physiological Importance, and Use as a Supplement. *Nutrients* **2020,** *12* (3).
27. Porath, J. Immobilized Metal Ion Affinity Chromatography. *Protein Expression Purif.* **1992,** *3* (4), 263-281.
28. Bornhorst, J. A.; Falke, J. J. [16] Purification of Proteins Using Polyhistidine Affinity Tags. *Methods Enzymol.* **2000,** *326*, 245-254.
29. Arnau, J.; Lauritzen, C.; Petersen, G. E.; Pedersen, J. Current Strategies for the Use of Affinity Tags and Tag Removal for the Purification of Recombinant Proteins. *Protein Expression Purif.* **2006,** *48* (1), 1-13.
30. Hutschenreiter, S.; Neumann, L.; Rädler, U.; Schmitt, L.; Tampé, R. Metal-Chelating Amino Acids as Building Blocks for Synthetic Receptors Sensing Metal Ions and Histidine-Tagged Proteins. *ChemBioChem* **2003,** *4* (12), 1340-1344.
31. Batchelor, L. K.; Ortiz, D.; Dyson, P. J. Histidine Targeting Heterobimetallic Ruthenium(Ii)-Gold(I) Complexes. *Inorg. Chem.* **2019,** *58* (4), 2501-2513.
32. Lim, J. K.; Kim, Y.; Lee, S. Y.; Joo, S.-W. Spectroscopic Analysis of L-Histidine Adsorbed on Gold and Silver Nanoparticle Surfaces Investigated by Surface-Enhanced Raman Scattering. *Spectrochim. Acta, Part A* **2008,** *69* (1), 286-289.

33. Ivanova, B. B.; Mitewa, M. I. Au (Iii) Interaction with Methionine-and Histidine-Containing Peptides. *J. Coord. Chem.* **2004,** *57* (3), 217-221.
34. Nivedhini Iswarya, C.; Kiruba Daniel, S. C. G.; Sivakumar, M. Studies on L-Histidine Capped Ag and Au Nanoparticles for Dopamine Detection. *Mater. Sci. Eng., C* **2017,** *75*, 393-401.
35. Warzajtis, B.; Glisic, B. D.; Savic, N. D.; Pavic, A.; Vojnovic, S.; Veselinovic, A.; Nikodinovic-Runic, J.; Rychlewska, U.; Djuran, M. I. Mononuclear Gold(Iii) Complexes with L-Histidine-Containing Dipeptides: Tuning the Structural and Biological Properties by Variation of the N-Terminal Amino Acid and Counter Anion. *Dalton Trans.* **2017,** *46* (8), 2594-2608.
36. Serpell, C. J.; Cookson, J.; Beer, P. D. N-Functionalised Imidazoles as Stabilisers for Metal Nanoparticles in Catalysis and Anion Binding. *ChemistryOpen* **2020,** *9* (6), 683-690.
37. Feyer, V.; Plekan, O.; Ptasińska, S.; Iakhnenko, M.; Tsud, N.; Prince, K. C. Adsorption of Histidine and a Histidine Tripeptide on Au(111) and Au(110) from Acidic Solution. *J. Phys. Chem. C* **2012,** *116* (43), 22960-22966.
38. Cohavi, O.; Reichmann, D.; Abramovich, R.; Tesler, A. B.; Bellapadrona, G.; Kokh, D. B.; Wade, R. C.; Vaskevich, A.; Rubinstein, I.; Schreiber, G. A Quantitative, Real-Time Assessment of Binding of Peptides and Proteins to Gold Surfaces. *Chemistry–A European Journal* **2011,** *17* (4), 1327-1336.
39. Buduru, P.; Reddy, B. C. S. R.; Naidu, N. V. S. Functionalization of Silver Nanoparticles with Glutamine and Histidine for Simple and Selective Detection of Hg2+ Ion in Water Samples. *Sens. Actuators, B* **2017,** *244*, 972-982.
40. Takeuchi, H. Raman Structural Markers of Tryptophan and Histidine Side Chains in Proteins. *Biopolymers* **2003,** *72* (5), 305-317.
41. Kho, K. W.; Dinish, U.; Kumar, A.; Olivo, M. Frequency Shifts in Sers for Biosensing. *ACS Nano* **2012,** *6* (6), 4892-4902.

42. Prodan, E.; Nordlander, P.; Halas, N. Electronic Structure and Optical Properties of Gold Nanoshells. *Nano Lett.* **2003,** *3* (10), 1411-1415.
43. Prodan, E.; Radloff, C.; Halas, N.; Nordlander, P. A Hybridization Model for the Plasmon Response of Complex Nanostructures. *Science* **2003,** *302* (5644), 419-422.
44. Halas, N. J.; Lal, S.; Chang, W. S.; Link, S.; Nordlander, P. Plasmons in Strongly Coupled Metallic Nanostructures. *Chem. Rev.* **2011,** *111* (6), 3913-61.
45. Li, J. J.; Wu, C.; Zhao, J.; Weng, G. J.; Zhu, J.; Zhao, J. W. Synthesis and Sers Activity of Super-Multibranched Auag Nanostructure Via Silver Coating-Induced Aggregation of Nanostars. *Spectrochim. Acta, Part A* **2018,** *204*, 380-387.
46. Atta, S.; Beetz, M.; Fabris, L. Understanding the Role of Agno3 Concentration and Seed Morphology in the Achievement of Tunable Shape Control in Gold Nanostars. *Nanoscale* **2019,** *11* (6), 2946-2958.
47. Nehl, C. L.; Liao, H.; Hafner, J. H. Optical Properties of Star-Shaped Gold Nanoparticles. *Nano Lett.* **2006,** *6* (4), 683-688.
48. Hao, F.; Nehl, C. L.; Hafner, J. H.; Nordlander, P. Plasmon Resonances of a Gold Nanostar. *Nano Lett.* **2007,** *7* (3), 729-732.
49. Nehl, C. L.; Hafner, J. H. Shape-Dependent Plasmon Resonances of Gold Nanoparticles. *J. Mater. Chem.* **2008,** *18* (21), 2415-2419.
50. Miura, T.; Satoh, T.; Hori-i, A.; Takeuchi, H. Raman Marker Bands of Metal Coordination Sites of Histidine Side Chains in Peptides and Proteins. *J. Raman Spectrosc.* **1998,** *29* (1), 41-47.
51. Kostko, O.; Xu, B.; Ahmed, M. Local Electronic Structure of Histidine in Aqueous Solution. *Phys. Chem. Chem. Phys.* **2021,** *23* (14), 8847-8853.
52. Zhu, G.; Zhu, X.; Fan, Q.; Wan, X. Raman Spectra of Amino Acids and Their Aqueous Solutions. *Spectrochim. Acta, Part A* **2011,** *78* (3), 1187-95.

53. Lim, J. K.; Kim, Y.; Lee, S. Y.; Joo, S. W. Spectroscopic Analysis of L-Histidine Adsorbed on Gold and Silver Nanoparticle Surfaces Investigated by Surface-Enhanced Raman Scattering. *Spectrochim. Acta, Part A* **2008,** *69* (1), 286-289.

54. Yi, C.; Sun, X.; Ye, J.; Ding, L.; Liu, M.; Yang, Z.; Lu, X.; Zhang, Y.; Ma, L.; Gu, W. Key Residues of the Receptor Binding Motif in the Spike Protein of Sars-Cov-2 That Interact with Ace2 and Neutralizing Antibodies. *Cell. Mol. Immunol.* **2020,** *17* (6), 621-630.

55. Yi, C.; Sun, X.; Ye, J.; Ding, L.; Liu, M.; Yang, Z.; Lu, X.; Zhang, Y.; Ma, L.; Gu, W.; Qu, A.; Xu, J.; Shi, Z.; Ling, Z.; Sun, B. Key Residues of the Receptor Binding Motif in the Spike Protein of Sars-Cov-2 That Interact with Ace2 and Neutralizing Antibodies. *Cell. Mol. Immunol.* **2020,** *17* (6), 621-630.

56. Zhang, D.; Zhang, X.; Ma, R.; Deng, S.; Wang, X.; Wang, X.; Zhang, X.; Huang, X.; Liu, Y.; Li, G.; Qu, J.; Zhu, Y.; Li, J. Ultra-Fast and Onsite Interrogation of Severe Acute Respiratory Syndrome Coronavirus 2 (Sars-Cov-2) in Waters Via Surface Enhanced Raman Scattering (Sers). *Water Res.* **2021,** *200*, 117243.

CHAPTER 5

Conclusions

5.1. Successes of Hollow Multibranched Gold SERS Substrates

The methods discussed throughout this work aimed to eliminate the need for reporter molecules enabling the direct spectroscopic detection of molecules such amyloid beta, SARS-CoV-2 spike, and Anti-SARS-CoV-2 antibodies. Hollow multibranched gold nanostructures were able to accomplish direct detection due to their increased number of hot spots compared to smooth nanoparticles. Additionally, the LSPR of the substrates was tuned to be close excitation wavelength resulting in a larger localized EM field and an increased SERS intensity. The use of a near-IR LSPR helped to avoid fluorescence backgrounds associated with biological molecules.

5.2. Emerging SERS Substrates

SERS uses the plasmonic fields at hotspots of noble metal nanostructures, typically a gap junction between nanoparticles, to enhance Raman signals. Despite the high chemical specificity, SERS measurements are limited by reproducibility to detect a broad range of analytes. Because the local electric fields are highly heterogeneous, over 99% of the analyte molecules are located outside of the hotspots on a typical SERS substrate and contribute minimally to the signal, leading to limited sensitivity and poor reproducibility. Novel trimer SERS substrate that consists of three nanoparticles precisely organized in 3D can focus intense EM fields near the binding sites of analyte molecules, leading to enhancement factors exceeding 10^{12}. The Ye group has worked on fabricating the novel 3D nanoparticle assembly at UC Merced. The Ye group uses DNA origami method to form a 3D cage. Long single-

stranded DNA fold into designer shapes using the help of short oligonucleotides. The cage's interior contains capture strands that can base-pair with the DNA ligands functioning the small nanoparticle. Therefore, the small nanoparticle (10 nm in diameter) can bind to the cage.

Another new class of plasmonic nanoparticle were synthesized by Nam et al. in 2019. Helicoid gold nanostructures have a spiral surface morphology, several intersecting crystalline grain boundaries, and crystallographic phases present on the surface as seen in Figure 1 below. Helicoid nanostructures were developed via a wet chemical technique. This is important because we can control the chirality of the surface by using R or S amino acids. The shape is understood to evolve from the FCC crystal structure of gold to the {321} index, which consists of <100>, <110>, and <111>. The numerous crystallographic interfaces and overall change in plasmonic properties will likely vary the spintronic behavior from other better understood gold nanoparticles. Additionally, the sharp edges and fine surface features will lead to exciting surface plasmon polaritons useful for Raman optical activity and SERS measurements.

5.3. Future Work

Chapter 4 demonstrated that histidine could simplify the bioconjugation process enabling the direct detection of SARS-CoV-2 spike protein and anti- SARS-CoV-2 antibodies. Collaborating with the Dubois lab at UC Santa Cruz could lead to screening

active COVID-19 cases in live patients. A likely route to improve screening would be to combine SERS with a lateral flow immunoassay. SERS could increase the reliability of the colorimetric results and potentially aid in understanding SARS-CoV-2 mutations and Covid-19 disease progression.

CHAPTER 6

Experimental Details and Characterization

6.1. General Methods

All materials were commercially available unless otherwise notes. Reducing agents were kept in a vacuum desiccator after the bottle was opened.

6.1.1. Chapter 2

Fatty Acid Solubilization

Palmitic acid (ACROS 129702500), stearic acid (Sigma-Aldrich 175366), myristic acid (Sigma-Aldrich 70082) and decanoic acid (Sigma-Aldrich W236403) with purity >98%, were ground into a fine powder then stored individually. A generous amount of fatty acid powder was mixed with 0.01M of reagent grade sodium hydroxide in water then vortexed three times for one minute each then sonicated for one hour at room temperature. Finally, the fatty acid solutions were stirred at room temperature overnight after which they were ready for analysis.

Total organic carbon (TOC)

TOC measurements were used for determining the amount of FA that were solubilized in a sodium hydroxide solution. The concentration of the TOC on each sample was obtained according to Standard Method 53104 B using a Shimadzu TOC-VCSH (Shimadzu Scientific Instruments, Columbia, MD).

Silver Nanoparticle Synthesis

The silver nanoparticles were synthesized following a modified Lee-Meisel silver colloid synthesis reported by Leopold and Lendl.[5] Overall, 10mL of the reducing

solution containing $NH_2OH \cdot HCl$ and 100µL of 4.5mM NaOH was added dropwise to 90mL of an $AgNO_3$ solution. The final molar values of $AgNO_3$ and $NH_2OH \cdot HCl$ were 1mM and 1.5mM respectively.

UV-Visible Spectroscopy

UV−vis spectra were recorded with an Agilent Technologies Cary 60 UV−vis spectrophotometer using a 700 µL quartz cuvette with 10 mm optical path length. The extinction measurements were performed on washed silver nanoparticles in an open environment. The washing procedure entailed centrifuging the nanoparticles three times under ambient conditions at 13 000 rpm for 2 min.

Electron Microscopy

Scanning electron microscopy (SEM) was performed at the W.M. Keck Center for Optofluidics at the University of California, Santa Cruz on an FEI Quanta 3D field emission microscope operated at 10.00 kV acceleration voltage. A 10 µL aliquot of diluted, 0.2 OD, silver nanoparticle solution was dropcast onto a 400 mesh copper grid with a carbon support film of standard 5−6 nm thickness (Electron Microscopy Sciences) and allowed to dry. The diameter of the nanoparticles was directly measured from SEM images using ImageJ software. Over 100 nanoparticles were measured and used to calculate the average diameter

Raman Spectroscopy, SERS and Fiber Enhanced SERS

Non-SERS solutions in this study was prepared by diluting the four aqueous FA solutions. The final concentrations ranged from micromolar to nanomolar. The SERS samples were prepared by 9:1, AgNP:analyte, dilutions for a total volume of 1mL and sodium chloride NaCl, 10 mM was added to induce aggregate formation. The solutions were incubated for about 10 min and SERS tests were performed about 20 min after the introduction of salt.

The hollow core photonic crystal fiber (HCPCF) used in our experiment was purchased from Thorlabs Inc. (Model HC-800B). The central core diameter is 7.5 m and the cladding pitch is 2.3 m. The fiber has a low transmission loss in the wavelength range of 735–915 nm.

The method for immobilizing nanoparticles on the fiber optic probe is below.[6] The end of the fiber tip was carefully cleaned by immersion for about 15 min in a piranha solution (3:1 mixture of 96% sulphuric acid and 30% hydrogen peroxide) and rinsed with H2O four times and twice with methanol. The cleaned fiber was dipped in a solution containing 90% of methanol, 5% of distilled water and 5% of APTMS. After about 15 min the fiber tip was extracted from the solution and rinsed four times with methanol to remove the excess of APTMS. The fiber tip was then cured for about 30 min at about 90 ◦C and then rinsed again three times with methanol. When all methanol was evaporated the tip was immersed for about 48 h in a colloidal solution of silver nanoparticles prepared by a modified Lee and Meisel method and highly

concentrated before use. The fiber tip obtained was then rinsed with methanol and distilled water.

Raman measurements

All the Raman and SERS soectra were measured using a Renishaw inVia Raman spectrometer at 532 nm laser. The laser was focused onto the sample using 5x objective with an effective power of 0.03mW at the sample surface. For each aqueous fatty acid sample (SERS and non-SERS samples) one single, 10sec scan was recorded and performed 3 times for reproducibility. The FERS scans were performed the identical laser wavelength and power at one single, 60sec accumulation.

6.1.2. Chapter 3

Synthesis of Hollow Gold Nanostars

Seed templated technique. The nanoparticle were made from a 150 nm gold nanoshell. All water used was ultrapure with a resistivity of 18.3 MΩ. The HNS were synthesized using a modified method published by Yuan *et al*. which entailed adding 100 µL of the seed solution to a 10 mL solution containing 0.10 M $HAuCl_4$ (5.0 µL, 10 µL, 20 µL, 40 µL, 60 µL) and 10 µL of 1.0 M HCl. Then immediately adding a 100 µL 3.0 mM silver nitrate solution and 50 µL of 100 mM ascorbic acid simultaneously resulted in a bluish green color change indicating the presence of spikes. Once the color changed, the solution was centrifuged with PEG-SH as a stabilizing agent. The particles were then conjugated and used in SERS measurements.

UV-Visible Spectroscopy

UV-visible electronic absorption spectra were recorded with an Agilent Technologies Cary 60 UV-vis spectrophotometer using a 700 μL quartz cuvette with 10 mm optical path length. The extinction measurements were performed on washed silver nanoparticles in an open environment. The washing procedure entailed centrifuging the nanoparticles three times under ambient conditions at 13,000 rpm for 2 minutes.

Electron Microscopy

Scanning electron microscopy (SEM) was performed on an FEI Quanta 3D field emission microscope operated at 5.00 kV acceleration voltage. HGN solutions were drop cast onto a 400-mesh copper grid (Ted Pella). High resolution transmission electron microscopy (HRTEM) was performed on a FEI UT Tecnai microscope operated at 200 kV acceleration voltage. Diameter measurements were taken directly from the electron microscopy images using ImageJ software. EM tomography -

Bioconjugation of Hollow Gold Nanostars and Bicinchoninic Acid Protein Assay

OPSS-PEG_{5K}-SVA was purchased from Laysan Bio Inc. PEG_{2k}-SH and BCA assay kit were purchased from Fischer Scientific. $A\beta_{1-14}$ was purchased from Neta Scientific and had the following sequence of amino acids: DAEFGHDSGFEVRH. PEGylated HNS were prepared by incubating 20 mL of freshly prepared HNS with 5 mL of 2 mg/mL OPSS-PEG_{5K}-SVA and 5 mL of 1 mg/mL PEG_{2K}-SH for one hour. The HNS-PEG particles were washed three times and redispersed in MilliQ water.

The HNS-PEG-analyte conjugates were prepared as follows: 100 µL of 1 mg/mL $A\beta_{1-14}$ was added to 9.9 mL of HNS-PEG, because of lower solubility 100 µg of tyrosyl-phenylalanine was added to 1.0 mL of HNS-PEG, and for both isoleucine and threonine 1.0 mg was added to 1 mL of HNS-PEG. The HNS-PEG-analyte conjugates were mixed on a shaker for 12 hour then washed, briefly sonicated, then washed again to remove unbound analyte and remove HNS conjugates that adhered to the centrifuge tube.

A Bicinchoninic Acid (BCA) assay was performed using 10 parts of the BCA Working Reagent and 1 part of the protein sample. The two solutions were combined then vortexed for 30 sec and incubated at 37 °C for 30 min under gentle mixing. The absorbance at 562 nm of a dilution series using known concentrations of Bovine Serum Albumin (BSA) from 2.7 µM to 0.55 µM was used to construct a calibration cure. Subsequently, Aβ conjugated HNS were analyzed using the protocol above then the concentration of Aβ was found using the calibration curve.

Raman Spectroscopy and SERS

All the Raman and SERS spectra were measured using a Renishaw inVia Raman spectrometer at 785 nm laser. The laser was focused onto the surface of the colloidal solution using a 50x objective with an effective power of 30 mW exiting the objective lens. The SERS samples were prepared by 9:1 nanoparticle:analyte dilution with a total volume of 1.0 mL.

6.1.3. Chapter 4

Reagents and Supplies

Gold Nanoshells (Nanocomposix, GSXR150-5M), tetrachloroauric acid (SigmaAldrich, 1.01582), silver nitrate (SigmaAldrich, 209139), ascorbic acid (SigmaAldrich, 1043003), BCA protein assay kit (ThermoFisher, 23227), SARS-CoV-2 spike protein S1 (ThermoFisher, RP-87679), SARS-CoV-2 (2019-nCoV) Spike S1 Antibody, Rabbit mAb (Sinobiological, 40150-R007), 400-mesh copper grid (Ted Pella, 01822).

Synthesis of Nanoshell Templated Gold Nanostars

The multibranched nanoshells were synthesized using a seed templated method.[45] The seed particles were purchased from Nanocomposix at a concentration of $2.8x10^{10}$ particles per milliliter with a hydrodynamic diameter of 164 nm. All water used was ultrapure with a resistivity of 18.3 MΩ. A 50 µL aliquot of the nanoshells was added to a 10 mL solution containing 20 µL 0.10 M $HAuCl_4$. Then immediately, 10 µL of 1.0 M HCl, 100 µL 3.0 mM silver nitrate solution, and 50 µL of 100 mM ascorbic acid were added in that order, which resulted in a pale teal blue color change indicating the presence of spikes. Once the color changed, the solution was centrifuged, then mixed with the S1 protein, followed by the COVID-19 anti-spike monoclonal antibody.[66]

UV-Visible Spectroscopy

UV-visible extinction spectra were recorded using an Agilent Technologies Cary 60 UV-vis spectrophotometer. The optical path length of the 700 μL quartz cuvette was 10 mm. The measurements were performed on washed gold nanoparticles in an open environment. The washing procedure entailed centrifuging the nanoparticles three times under ambient conditions at 13,000 rpm for 2 minutes.

Electron Microscopy, Energy Dispersive X-Ray Spectroscopy, and Electron Tomography

Scanning electron microscopy (SEM) was performed on an FEI Quanta 3D field emission microscope operated at 5.00 kV acceleration voltage. The multibranched nanoshell solutions were drop cast onto a 400-mesh copper grid (Ted Pella). High resolution transmission electron microscopy (HRTEM) was performed on an FEI UT Tecnai microscope operated at 200 kV acceleration voltage. A Thermo Fisher Scientific Titan TEM was used in STEM mode to obtain high-angle annular dark-field (HAADF) images; elemental maps were obtained using energy-dispersive X-ray spectroscopy (EDS) of the Au K-, Ag K-, and Si K-edges. All images were acquired with an accelerating voltage of 200 kV. STEM images before and after EDS mapping were recorded, to monitor signs of beam damage due to contaminants. Analysis of EDS maps was performed using the Bruker Esprit software. Individual nanoparticles were analyzed by quantifying selected regions of the EDS maps. STEM tomography was performed by recording HAADF images at tilt angles from -36^{o} to

36º. The image alignment and 3D reconstructions were performed using custom Matlab scripts implementing the simultaneous iterative reconstruction technique (SIRT) method.[67] Visualizations of the reconstruction slices and radial intensity measurements were performed using Matlab scripts. Visualization of the particle surfaces in 3D were performed using the TomViz software program.[68] The diameter and shell thickness measurements were performed using Image J on both the HAADF and HRTEM.[69]

Multibranched Nanoshell Conjugation and Bicinchoninic Acid Protein Assay

After synthesis, the multibranched nanoshells were washed three times and then redispersed in MilliQ water. The multibranched nanoshells were concentrated from 3.0 mL down to 0.50 mL, then mixed with 30 μL of spike protein, gently shaken for 30 minutes, then centrifuged. The pelleted multibranched nanoshell was redispersed in 0.50 mL of MQ water, then 5.0 μL of Anti-SARS-CoV-2 monoclonal antibody was added then incubated overnight. The multibranched gold nanoshell-SARS-CoV-2 S1 spike protein- monoclonal antibody conjugate was centrifuged, redispersed in 100 μL of MQ water, then analyzed immediately.

A Bicinchoninic Acid (BCA) assay was performed using ten parts of the BCA Working Reagent and 1 part of the protein sample. The two solutions were combined, then vortexed for 30 sec and incubated at 37 °C for 30 min under gentle mixing. The absorbance at 562 nm of a dilution series using known concentrations of Bovine Serum Albumin (BSA) from 2.7 μM to 0.55 μM was used to construct a calibration

curve. Subsequently, multibranched gold nanoshell-spike and multibranched gold nanoshell-SARS-CoV-2 S1 spike protein- monoclonal antibody conjugates were analyzed using the protocol above then the concentration of spike and monoclonal antibody were found using a calibration curve.

Raman Spectroscopy and SERS

All Raman and SERS spectra were measured using a ThermoFisher DXR2 Raman microscope with a 785 nm laser. The laser was focused onto the surface of the colloidal solution using a 50x objective with an effective power of 30 mW exiting the objective lens.